REPORT DOCUMENTATION PAGE

Form Approved
OMB No. 0704-0188

1. REPORT DATE *(DD-MM-YYYY)*	2. REPORT TYPE	3. DATES COVERED *(From - To)*
14/08/2018	final technical	15/05/2014-14/08/2018

4. TITLE AND SUBTITLE
Probabilistic Multi-Scale Damage Tolerance Modeling of Composite Patches for Naval Aluminum Alloys

5a. CONTRACT NUMBER

5b. GRANT NUMBER
N00014-14-1-0516 and N00014-16-1-2370

5c. PROGRAM ELEMENT NUMBER

6. AUTHOR(S)
TerMaath, Stephanie C.

5d. PROJECT NUMBER

5e. TASK NUMBER

5f. WORK UNIT NUMBER

7. PERFORMING ORGANIZATION NAME(S) AND ADDRESS(ES)
University of Tennessee
Knoxville, TN 37996

8. PERFORMING ORGANIZATION REPORT NUMBER

9. SPONSORING/MONITORING AGENCY NAME(S) AND ADDRESS(ES)
Office of Naval Research
875 N. Randolph Street Suite 1425
Arlington VA 22203-1995

10. SPONSOR/MONITOR'S ACRONYM(S)
ONR 331

11. SPONSOR/MONITOR'S REPORT NUMBER(S)

12. DISTRIBUTION/AVAILABILITY STATEMENT
DISTRIBUTION A. Approved for public release: distribution unlimited.

13. SUPPLEMENTARY NOTES

14. ABSTRACT
The goal of this research is to develop multi-scale, physics-based models and methodologies that predict the damage tolerance and performance of hybrid structures. The technical approach consists of three concurrent and integrated components throughout the entire research effort: modeling and simulation (M&S), experimental testing, and sensitivity analysis. The multi-scale models and methodology include the damage mechanisms of interlaminar and intralaminar composite overlay damage, plasticity, sensitization and crack growth in the metal, as well as disbond at the metal/polymer interface.

15. SUBJECT TERMS
ship repair, composite patch, sensitization, damage tolerance

16. SECURITY CLASSIFICATION OF:			17. LIMITATION OF ABSTRACT	18. NUMBER OF PAGES	19a. NAME OF RESPONSIBLE PERSON
a. REPORT	b. ABSTRACT	c. THIS PAGE			Stephanie TerMaath
					19b. TELEPHONE NUMBER *(Include area code)*
UU	UU	UU	UU	104	865-974-7711

Probabilistic Multi-Scale Damage Tolerance Modeling of Composite Patches for Naval Aluminum Alloys

Office of Naval Research Grant Number: N00014-14-1-0516/N00014-16-1-2370

Point of Contact

Dr. Stephanie TerMaath

Assistant Professor
Department of Mechanical, Aerospace, and Biomedical Engineering
1512 Middle Drive
Knoxville, TN 37996-2010

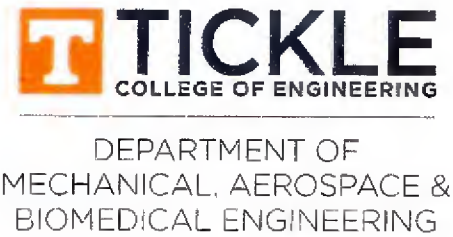

Abstract

The Office of Naval Research (ONR) Structural Reliability Program strives to assure "successful performance of a ship hull structure over its intended life." Due to loading and structural degradation given extreme operating environments, ship hulls may require repair or reinforcement during their lifetimes. One type of modification with a proven service record is to adhesively bond a composite overlay onto the metallic structure. (The system of a composite overlay bonded to an aluminum substrate is herein defined as a hybrid structure.) While in-service demonstration of this repair method establishes its successful application to ship structure, our understanding of the complex damage tolerance behavior and structural performance of these hybrid structural systems is lagging behind the implementation, as are standard reliability-based design procedures. Therefore, composite overlays are currently installed only as temporary repairs, and a thorough understanding of hybrid structure behavior under service loading and its long term performance is necessary to enable its reliable and widespread implementation.

To investigate the reliability of hybrid structure, it is necessary to consider multiple damage mechanisms, including the progressive failure of the composite overlay, and the interactions between the damage mechanisms when predicting damage initiation and propagation in the hybrid structure. Additionally, the effects of the many complex sources of error, such as epistemic, aleatoric, and experimental uncertainty as well as model form error, must be evaluated and quantified. Performing physical experiments to carry out a comprehensive damage tolerance study that includes all potential configurations, sources of uncertainty, damage mechanisms, and loading conditions is prohibitive. Numerical modeling offers an alternative method to efficiently explore designs and investigate the effects of parameters on hybrid structure after validating a baseline model through experimental testing. Given the many types of damage mechanisms that affect the damage tolerance of hybrid structure, there is no single numerical method capable of accurately simulating all mechanisms simultaneously with the required fidelity level and within a feasible amount of computation time. Therefore, multi-scale modeling with varying levels of fidelity at each scale is required to develop the capability to comprehensively investigate the damage tolerance of hybrid structure.

The goal of this research is to overcome many of these challenges through the development of multi-scale, physics-based models and methodologies that predict the damage tolerance and performance of hybrid structures. Through distinct models, customized for particular damage mechanisms, this approach captures widely varying physics, making it advantageous for complex problems such as hybrid structure performance. This effort integrates computational simulation at multiple scales with concurrent experimental testing to obtain material properties, fill in knowledge gaps pertaining to damage initiation and propagation, and provide validation data. Sensitivity analysis identifies the most influential parameters to patch performance enabling Navy implementation of this knowledge for effective design and optimization of patch configuration. Fundamental knowledge at multiple scales, informed by this research initiative, improve the understanding and guided efforts for reliable use of this repair technique.

The technical approach consists of three concurrent and integrated components throughout the entire research effort: modeling and simulation (M&S) to develop predictive models and methodology across multiple scales, sensitivity analysis to identify the most influential parameters

on damage tolerance performance, and experimental testing for characterization and model validation. The multi-scale models and methodology include the damage mechanisms of interlaminar and intralaminar composite overlay damage, plasticity, sensitization and crack growth in the metal, as well as disbond at the metal/polymer interface. Computational methodology encompasses both first principle calculation and numerical methods including Density Functional Theory (DFT), Peridynamics (PD), and Finite Element (FE) Analysis. Top down engineering requirements inform bottom up physics-based modeling and methodology development to simulate material science properties and structural performance. Computational model development, experimental testing, and sensitivity analysis was performed concurrently at all scales to account for the many types of parameter uncertainty, including model form error, experimental error, epistemic uncertainty, and aleatoric uncertainty, and to determine parameter influence on individual damage mechanisms as well as global damage tolerance.

While this approach was demonstrated to be efficient and resulted in plug and play models that enable the evaluation of varying scenarios, several significant outcomes and recommendations should be considered in future work:

- The parameter space is expansive, complex, and non-linear making it prohibitive, even with supercomputing resources, to build accurate surrogate models that encompass the entire space. Sensitivity analysis is also challenging given the difficulty in generating a surrogate model and the massive amount of sample data necessary to calculate converged data-driven Sobol Indices. Methodology to map the entire parameter space is needed to identify the dominant damage mechanisms and corresponding sensitive parameters in subspaces and their locations in the global space as well as the transitions between subspaces.
- Damage should be quantified by the amount of energy absorbed by each individual damage mechanism and these values used to map out the parameter space. This information is readily extracted from the computational results, and damage energy can be correlated to the physical amount of damage in the structure. A maximum allowable amount of energy can then be set for each type of damage to ensure reliable patch performance.
- One significant limitation in this research that must be considered in design, analysis, and future work is that all variables were defined as independent in the sensitivity analysis. Parameter correlation and dependency is inherent in this problem and must be investigated for improved implementation of sensitivity analysis results into design, analysis, and optimization procedures.
- This study evaluated Sobol Indices for first order and total effects and identified parameters with a significant difference between the two. Higher order effects calculations using chosen parameter combinations are then needed to identify the interacting parameters. An efficient method to systematically identify these interacting parameter combinations is needed.

Table of Contents

1 Project Overview

To produce lighter and faster ships, the Navy is increasingly utilizing lightweight aluminum in the design of new ships that operate in harsh marine environments and are subject to extreme loading conditions. Damage caused by these operating conditions include aluminum degradation and fracture. A composite overlay, or patch, effectively redistributes the load around the damaged section and restores load-carrying capacity of these damaged aluminum structures upon bonding to the metallic component (Figure 1). Ships with damaged aluminum structures, repaired by composite patches, are currently in service, and while the repair method is proving to be effective (Figure 2), our understanding of the complex behavior of patched systems is lagging behind the implementation, as are standard reliability-based design procedures. Therefore, composite patches are currently installed only as temporary repairs. (The system of a composite patch bonded to an aluminum substrate is herein defined as a hybrid structure.)

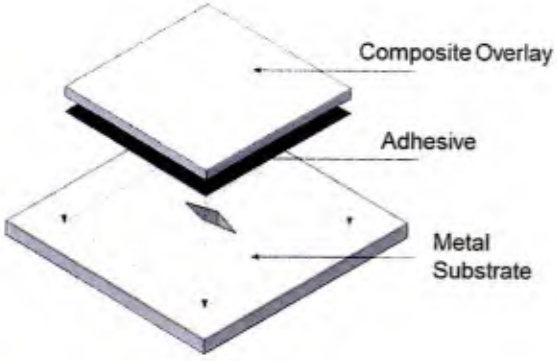

Figure 1. Composite overlay configuration (hybrid structure). In the application investigated herein, the adhesive is a layer of resin that is used to co-cure the composite overlay to the metal substrate.

Figure 2. Example of a US Navy composite overlay installed on a ship deck. There are currently prototypes aboard 12 ships totaling 70 patches in service.

For hybrid structures to progress past temporary repairs, the structural reliability over a specified lifespan must be ensured, requiring an improved understanding of the damage tolerance and damage mechanisms (Figure 3). Methods to predict the propagation of multiple, interacting damage mechanisms are required to ensure certain reliability metrics are met for long term implementation. Current methods to predict damage tolerance and propagation include large, expensive test programs, however recent advances in computational simulation provide an environment suitable to introduce complex numerical formulations for the prediction of various damage mechanisms. To achieve a standardized approach for reliability analysis, validated, physics-based models capable of simulating structural performance are needed, where the many complex sources of error, such as epistemic, aleatoric, and experimental uncertainty as well as model form error, can be quantified. The generation of such models requires the quantification and understanding of many design and installation variables including: amount and type of degradation in the pre-repaired aluminum, the configuration of the aluminum structure, the constitutive material properties, bond surface quality, and damage tolerance of the associated materials. Identification of the interactions between these parameters and damage mechanisms, and the associated uncertainty, is complex, yet critical to a comprehensive understanding of hybrid structure damage tolerance.

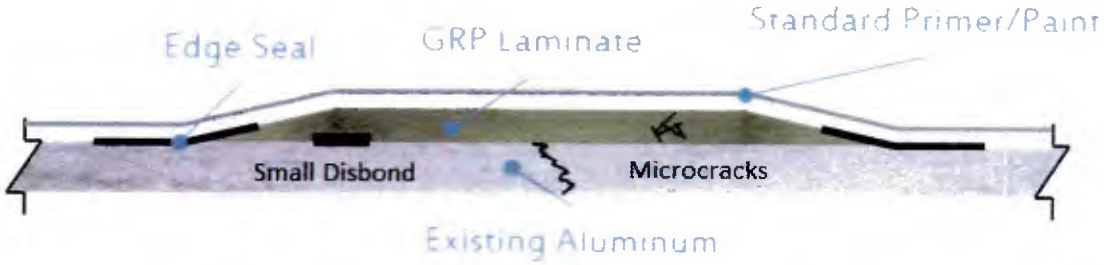

Figure 3. Damage mechanisms in hybrid structure include cracking and degradation in the aluminum, disbond at the metal/resin interface, and intralaminar damage in the composite patch.

Historically, many complexities have prohibited the development of the comprehensive models and methodologies necessary to fully simulate the behavior of the hybrid structure. In particular, several challenges must be overcome:

- The repaired system is constructed of distinctly different materials with different sets of constitutive properties, including fracture, and significantly different structural behaviors. A thorough understanding (including the combined fracture behavior, crack arrest, damage tolerance, and load distribution) of the repaired system is elusive.
- The fracture behavior of the repaired system is highly complex. In addition to the possibilities of multiple cracks and cracks that propagate through multiple materials, interactions of different damage mechanisms, and material degradation, must also be considered.
- Data for the properties of degraded aluminum are lacking, where the effects of degradation on crack behavior is relatively unknown and the effects on global patch behavior is intensely complex. Models are needed that account for degraded material in order to explore the effects on load redistribution and damage tolerance of repaired structure.
- Many sources of variability influence the performance of repaired structure. It is very difficult to have standard procedures that produce repeatable results for repair patches due to the complexities associated with the quality control on patch installation procedures which often lead to relatively poor or unknown reliability.
- Structural reliability data is lacking. In order to ensure structural performance, a systematic approach to uncertainty propagation is required, especially to implement into ship structural design procedures, retrofit design procedures, and to enable accurate reliability predictions.
- Much of the previous research on composite patches was performed by the aerospace industry and does not account for the thicker structure used in ships. Naval applications require bending effects and plastic deformation to be included in analysis.

The goal of this research is to overcome many of these challenges through the development of multi-scale, physics-based models and methodology that predict the damage tolerance and performance of hybrid structures. Through distinct models, customized for particular damage mechanisms or scales, this approach captures widely varying physics, making it advantageous for complex problems such as hybrid structure performance. This effort integrates computational

simulation at multiple scales with concurrent experimental testing to obtain material properties, fill in knowledge gaps pertaining to damage initiation and propagation, and provide validation data. Sensitivity analysis identifies the most influential parameters to patch performance enabling Navy implementation of this knowledge for effective design and optimization of patch configuration. All parameters in this research were defined as independent and interactions were identified in a general sense when present. Additional research is required that accounts for parameter correlation and dependencies and that identifies the specific parameter interactions. Fundamental knowledge at multiple scales, informed by this research initiative, improved the understanding and guided efforts for reliable use of this repair technique.

The research objective was achieved through the performance of three development phases during a period of performance of 4 years (Table 1). The specific objective for the initial award period, Phase 1, was to fully populate the multi-scale approach with preliminary models and methodology for each of the damage mechanisms and to identify the knowledge gaps in structural behavior and the limitations of the models. Additionally, sensitivity analysis methods were evaluated to determine the best approach to identify the most influential parameters on structural performance, identify interactions between parameters to quantify subspaces of optimal performance and unsafe performance, and evaluate uncertainty propagation across scales. The models and methodology used to populate the multi-scale approach in Phase 1 are primarily empirically driven (or data driven) given that the purpose of the initial effort was to demonstrate the feasibility of integrating models from atoms to structures to predict behavior and to identify knowledge gaps and limitations. Therefore, models and methodology were validated using existing test data similar to this configuration and parametric fits were performed to input material behavior in some cases. New methodology was implemented in Phase 2 to move towards more generic, physics-based capabilities for comprehensive investigation of materials, installation processes, and configurations. Additional experimental testing to characterize structural behavior and to provide validation was performed. To conclude this project, the focus of the Phase 3 effort was to demonstrate the models and probabilistic approach for relevant design and analysis applications. This report summarizes the final results from this effort.

Table 1. Phases and specific tasks performed to meet research objectives.

Task	Years 1 & 2	Year 3	Year 4
Phase 1: Exploration • Evaluate available modeling techniques and methodology • Develop preliminary models • Identify missing data • Perform sensitivity analysis			
Phase 2: Physics-based development • Perform experimental testing • Characterize damage space for individual mechanisms • Identify influential parameters throughout damage space • Develop physics-based models			
Phase 3: Damage space characterization • Model crack growth through sensitized aluminum with an overlay • Model demonstrations			

1.1 Naval Relevance

The Office of Naval Research (ONR) Structural Reliability Program strives to assure "successful performance of a ship hull structure over its intended life." Due to loading and structural degradation given extreme operating environments, ship hulls may require repair or reinforcement during their lifetimes. One type of modification with a proven service record is to adhesively bond a composite patch onto metallic structure. While experimental work at the Naval Surface Warfare Center Carderock Division (NSWCCD) and in-service demonstration of this repair method establish its successful application to ship structure, a thorough understanding of the behavior of this hybrid structure under service loading and its long term performance is necessary to enable its reliable and widespread implementation.

However, many gaps exist in our understanding of the structural behavior and damage tolerance of this repaired system. This lack of knowledge can result in poor structural performance or the use of large safety factors that may potentially result in unnecessary weight increase. The near term goal of this research is to advance the basic understanding and to optimize performance of composite patches adhesively bonded to metallic structure. Our improved models and methodology to investigate the structural performance of these repaired systems will enable their safe and effective use. Because this project focused on the basic research of physics-based model development, we did not develop design guidelines; however, the results provided by this research can be used by designers to develop load and resistance factors, safety factors, and optimization procedures.

Currently, there are limited guidelines for the design and implementation of composite patches, and this topic requires basic research given the future emphasis to use aluminum and other lightweight metals to replace steel. The ONR Structural Reliability Program seeks research that "will add to the development of a structural reliability-based toolset and decision criteria to ensure structural integrity of high speed vessels over their lifetime". The results of this research provide probabilistic-based methodology to help populate this toolset and data that can be used to develop design guidelines.

The long term potential use of hybrid structure extends beyond repairs and flat hull surfaces. Composites are easy to layup for more complex shapes, thus making them an attractive repair choice for joints. Additionally, hybrid structure may serve as a lightweight alternative to an all metallic structure [1, 2]. Metallic material provides global strength, while the composite provides superior corrosion resistance, damage tolerance, and stealth characteristics. The objective of an optimal hybrid design is to maximize the benefits and contribution of each material to reduce weight and improve performance over an all metallic structure. Our models and methodology can be used to optimize designs for complex applications.

1.2 Patch Configuration

This research focuses on the baseline E-glass/epoxy composite patch currently installed on Navy ships. This patch is applied to a 5xxx series aluminum plate (with a research focus on Al 5456 and Al 5083) using a hand lay-up procedure followed by vacuum bagging. The metal surface preparation is performed on the bonding side of the aluminum panel, following the application guide for AC-®130 provided by the distributor, Advanced Chemistry & Technology. To obtain a

quasi-isotropic laminate, ±45° (Vectorply E-BX 1200) and 0°/90° (Vectorply E-LT 1800) stitched fabrics are oriented according to the stacking sequence given in Figure 4. A 0°/90° plain weave ply (Hexcel 7500) is set first as the resin rich open ply while a 0°/90° fine harness stain weave ply (Hexcel 7781) is used as the top ply to obtain a quality surface. The entire thickness of the composite patch laminate is approximately 0.16 inch. The epoxy resin (PRO-SET M1002) is mixed with the curing agent (PRO-SET M2046 hardener) and spread on the fabrics layer by layer during the hand lay-up procedure. The composite patch is covered by a vacuum bag, with a P3 perforated film on the top of the composite patch to control the resin bleed rate. The vacuum level is set to 20 inHg for 3 hours and then the patch is cured at 140° F for 4 hours.

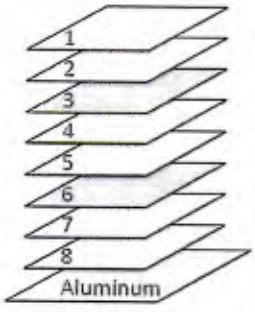

	E-glass Fabric	Fabrication Style
1	Hexcel 7781	0°/90° Satin weave
2	Vectorply E-BX 1200	±45° Stitch
3	Vectorply E-LT 1800	0°/90° Stitch
4	Vectorply E-BX 1200	±45° Stitch
5	Vectorply E-BX 1200	±45° Stitch
6	Vectorply E-LT 1800	0°/90° Stitch
7	Vectorply E-BX 1200	±45° Stitch
8	Hexcel 7500	0°/90° Plain weave

Figure 4. Stacking sequence of the E-glass/epoxy composite patch.

1.3 Integrated Technical Approach

To develop the probabilistic, multi-scale models and methodology to predict the damage tolerance and performance of hybrid structure requires the coalescence of fracture mechanics, material science, experimental testing, probabilistic analysis, advanced computational simulation, and high performance computing (HPC). Our technical approach consists of three concurrent and integrated components (Figure 5) throughout the entire research effort: modeling and simulation (M&S) to develop predictive models and methodology to investigate the damage tolerance of hybrid structure, sensitivity analysis to identify the most influential parameters on damage tolerance performance, and experimental testing for characterization and validation. Computational models spanning multiple scales were created to investigate the damage tolerance and structural behavior of hybrid structure. All models were validated through concurrent experimental testing or by comparison with test data from the literature. These validated computational models provide an efficient method to rapidly explore the design space and investigate the effects of many uncertain variables on damage tolerance. The uncertain input parameters at each scale were evaluated to identify the variables (and combinations of variables) that influence specific aspects of material and structural performance. Quantification and propagation of uncertainty in input parameters provided the necessary data to identify parameters and physical behavior with the most influence on damage tolerance informing model development focused on accurately capturing the related physics. Sensitivity analysis also informs experimental testing; allowing resources to be focused on thoroughly characterizing the most influential parameters.

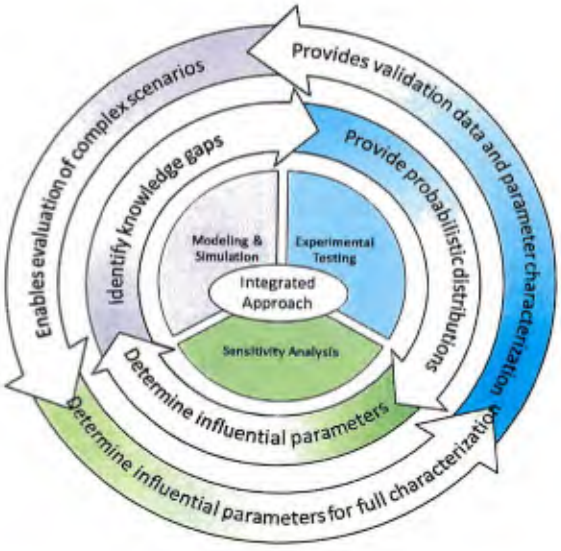

Figure 5. The technical approach integrates modeling and simulation, experimental testing, and sensitivity analysis at each step of the development process to produce validated computational models accompanied with the identification of the most influential input parameters on the uncertainty in each of the results produced by a given model.

While the developed capabilities are demonstrated for the specific application of hybrid structure, the developed methodology, analysis techniques, uncertainty quantification, and HPC processes can be applied to any generic structural design and analysis approach. Selected results are presented throughout this report to demonstrate specific capabilities and to present representative sensitivity analysis results. In the interest of report length, only a limited number of examples are described in detail.

1.4 Multi-Scale Model Development

As shown in Figure 6, the multi-scale model development begins at the atomic level and progresses through material microstructure ending with the prediction of damage tolerance at the macroscale. The multi-scale models and methodology include the damage mechanisms of interlaminar and intralaminar composite overlay damage, plasticity, sensitization and crack growth in the metal, as well as disbond at the metal/polymer interface (Figure 7). Computational methodology encompasses both first principle calculation and numerical methods including Density Functional Theory (DFT), Peridynamics (PD), and Finite Element (FE) Analysis. This range of methods is required to explore the diverse physical behavior and potential damage mechanisms to predict damage tolerance in hybrid structures. Top down engineering requirements inform bottom up physics-based modeling and methodology development to simulate material science properties and structural performance. Computational model development, experimental testing, and sensitivity analysis was performed concurrently at all scales to account for the many types of parameter uncertainty, including model form error, experimental error, epistemic uncertainty, and aleatoric uncertainty, and to determine parameter influence on individual damage mechanisms as well as global damage tolerance.

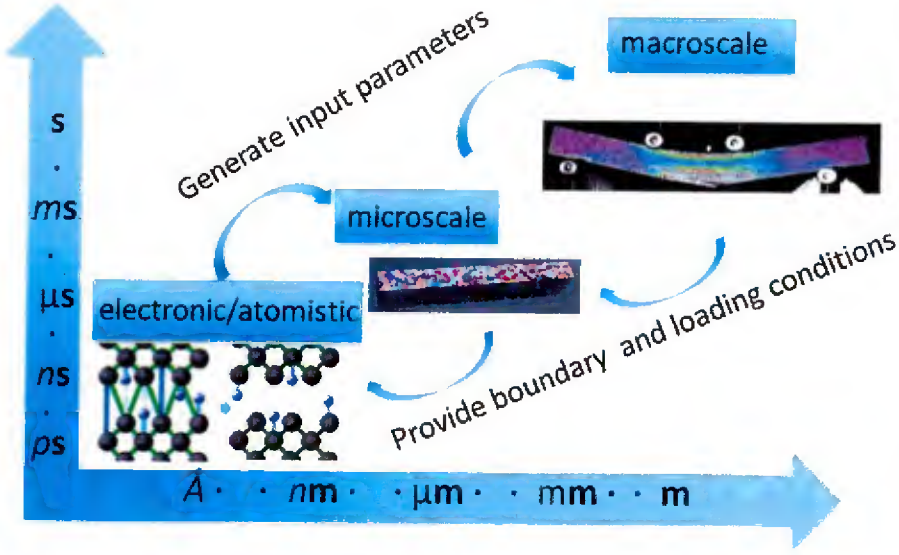

Figure 6. The multi-scale approach spans atoms to structure, and validated models capture chemical formulation, manufacturing effects, surface preparation, microstructure, material properties, and structural performance.

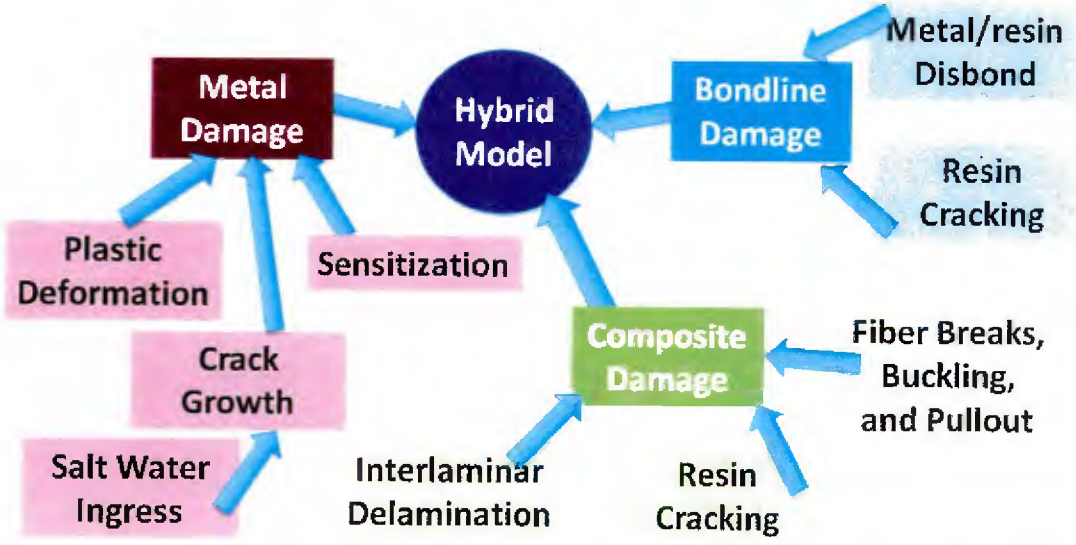

Figure 7. Many damage mechanisms are required to capture the diverse physical behaviors that contribute to the damage tolerance of hybrid structure.

Criteria and requirements for successful model development were:

- The multi-scale approach must be founded on physics-based models that are generic for varying material types and configurations. Data driven (or empirically driven) models, which require validation and physical testing for each new material combination, fail to meet the requirements of designers and analysts for use as a rapid exploration tool.
- The multi-scale approach must accurately capture physical behavior within and across scales; therefore, all models and methodology must be validated by comparison with experimental results.
- Exploration of the massive design space by including every possible parameter is not feasible, even when utilizing HPC resources. This complex space must be reduced to include only the most influential parameters on performance requirements. Sensitivity analysis is a critical component of the integrated development cycle to identify the most influential parameters

2 The Probabilistic Toolkit

A toolkit of probabilistic analysis capabilities, sensitivity analysis methods, surrogate models, and automated generation of input files for probabilistic analysis using HPC resources was compiled, and methods were linked for automated analysis when feasible. Identification of the most influential design parameters and quantification of uncertainty in the prediction of structural performance is enabled by the probabilistic and sensitivity analysis, which is applied at each scale and across scales. This knowledge informs design and analysis engineers of the manufacturing processes and material properties that have the greatest impact on product performance so that these parameters are identified to be fully characterized, assigned a probabilistic distribution, and optimized. If a parameter is deemed to be insensitive, an average result or design value can be used in analysis with minimal effect on the simulation, predicted material, and structural performance.

Figure 8 provides a conceptual diagram of the probabilistic framework that integrates the methodology contained in the toolkit. Figure 9 illustrates the details of the uncertainty quantification approach. The following steps provide a brief description of the features, capabilities, and architecture of this framework:

1. Sources of uncertainty are identified, and each source of uncertainty is represented as an independent input parameter for a computational simulation and included in the sensitivity analysis to quantify its influence on the performance results. All input files are written in parametric form allowing for the automated variation of the parameters and generation of input files.
2. The parametric set of input files, for a particular analysis, are provided to an analysis tool. This box represents all of the computational methodology available across all scales. A Monte Carlo loop is performed for each scale and the output at a scale i becomes the input to the subsequent scale $i+1$, making data management a critical component of this framework.
3. Analysis of the many input files needed to account for exploration of the design space was performed through the DoD HPCMP (HPC Modernization Program). At this point, a set of Big Data results is obtained, as all parameters are included in the investigation. To make the problem tractable, a small number of sampling subsets was specified for each parameter, and sensitivity analysis was performed on the results.

4. The influence of the parameters at each scale and across scales is quantified using sensitivity analysis to identify the effects of each on the performance results. This step is essential to reduce the number of parameters for uncertainty quantification by limiting the parameters for further evaluation to those that are the most influential. Less influential parameters are held at a constant average or design value for the remainder of the loop.
5. Each influential parameter is assigned a probability density function for uncertainty quantification. Additionally, these probability density functions are propagated across scales.
6. Another round of analysis is performed again moving through steps 2 and 3 using input files based on the most influential parameters and the assigned probability density functions to perform uncertainty quantification. All of the data collected and knowledge gained by performing these loops at each scale and across scales provides the capability for customized designs and exploration of the design space and informs design guidelines/safety factors and reliability-based design optimization.

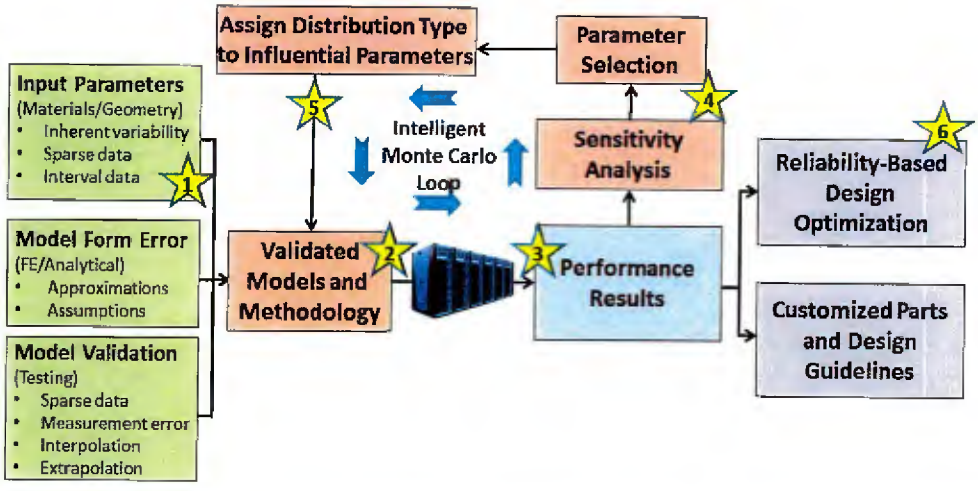

Figure 8. The probabilistic framework supports optimized reliability-based design of customized structural components and provides a tool for designers to rapidly explore the effects of material and manufacturing variations on performance, as well as to quantify the uncertainty in the structural performance.

Propagation of uncertainty through high-fidelity physics-based models can be very expensive computationally. For this reason, it is essential to sample the input space as efficiently as possible and evaluate the model as few times as possible while capturing the important statistical properties of the response. When needed, advanced Monte Carlo sampling methods were employed that integrate both adaptivity and optimality through sensitivity analysis. Advanced sampling techniques such as the partially stratified sampling method [3] can exploit interactions to greatly reduce the variance in statistical estimates from Monte Carlo simulations, thereby reducing the total number of necessary model evaluations.

The notion of partially stratified sampling stems from a generalization of the popular Latin hypercube sampling and stratified sampling methods. Latin hypercube sampling functions by stratifying the individual variables of the input vector, sampling from these strata, and randomly pairing them to build samples of the full input vector. At the other extreme, stratified sampling simultaneously stratifies all dimensions of the input vector and draws individual samples from

within each stratum. As recognized in [3], these correspond to two extremes in the spectrum of possible stratified designs with intermediate designs referred to as partially stratified designs. Latin hypercube sampling is perhaps the most widely used sampling method for the design of computer experiments because it has the important advantage of filtering additive effects. In other words, it greatly reduces the variance associated with the contribution of individual variables as they act through a transformation (i.e. it focuses on the individual sensitivities of each variable). Stratified sampling meanwhile, has been shown to very effectively reduce the variance associated with variable interactions [4]. The partially stratified designs aim to focus the stratification on those interactions that are deemed important to the analysis. In [3], the notions of Latin hypercube sampling and partially stratified sampling are combined to establish the Latinized partially stratified sampling method that has the advantage of simultaneously filtering the additive and interaction components. This results in a major advantage over existing methods and, for this reason, the LPSS method is used throughout this study.

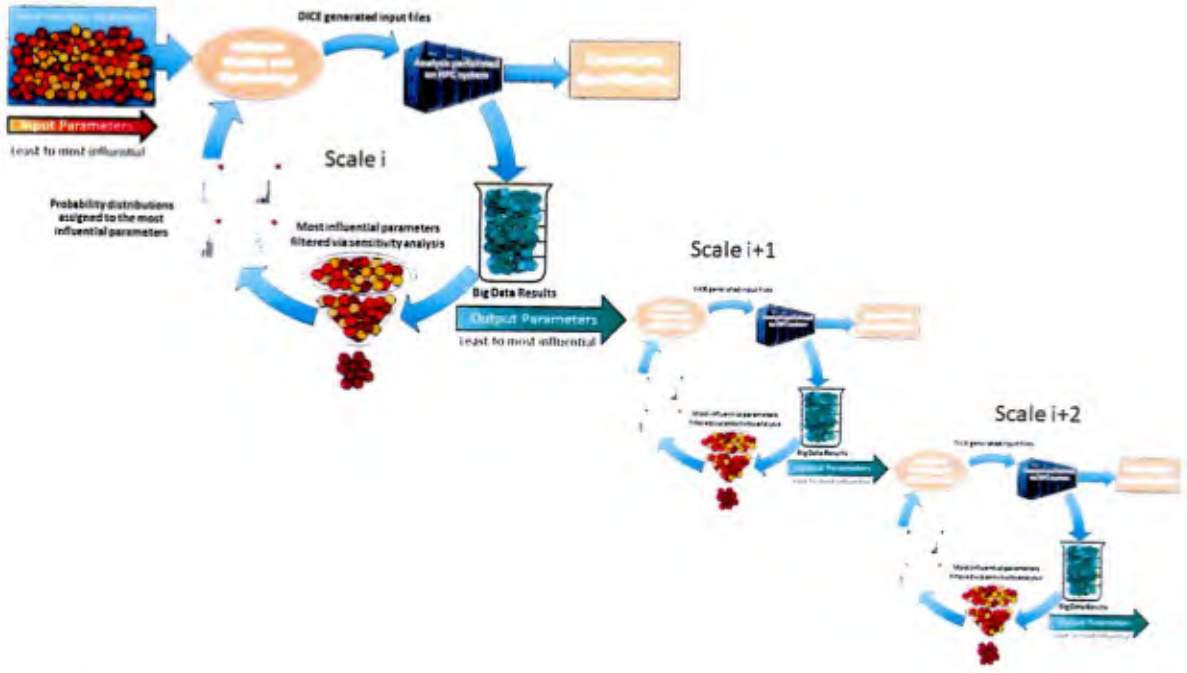

Figure 9. The analysis process for uncertainty quantification at a single scale is based on limiting the number of parameters to those identified as the most influential through sensitivity analysis. These highly influential parameters as well as output data at a scale is propagated to the next scale and the uncertainty quantification process repeats.

2.1 Sensitivity Analysis

An infeasible number of input parameters are required for many of the multi-scale models (for example, 50-200 input parameters are needed at the macroscale depending on how many types of uncertainty are considered), and many of these may be based on disparate and sparse data. Therefore, it is imperative to understand the influence of each parameter and its uncertainty on the analysis results, as well as eliminate parameters with minimal influence to limit the parameter

space to a feasible number for analysis. This knowledge will improve the current methodology, enable generic applications, and inform appropriate testing programs to gather critical data for uncertain but highly influential parameters.

When evaluating uncertainty across scales, the uncertain inputs at a scale i and their contribution to the uncertainty in the outputs then become inputs at the subsequent scale i+1 (Figure 10). In addition, new uncertain input parameters must be added to the analysis as needed at each scale to capture new physical behavior and damage mechanisms. This process results in the rapid generation of Big Data when accounting for the uncertainty introduced by each input parameter. When considering thousands of uncertain parameters, each described by probability distributions, it is clear that comprehensive exploration of the design space is intractable, even when utilizing an HPC system. To limit the design space to a feasible number of parameters, sensitivity analysis is performed to identify the most influential parameters on the output. The most influential parameters are then used in uncertainty quantification and design space exploration while all other parameters are held constant at average or design values.

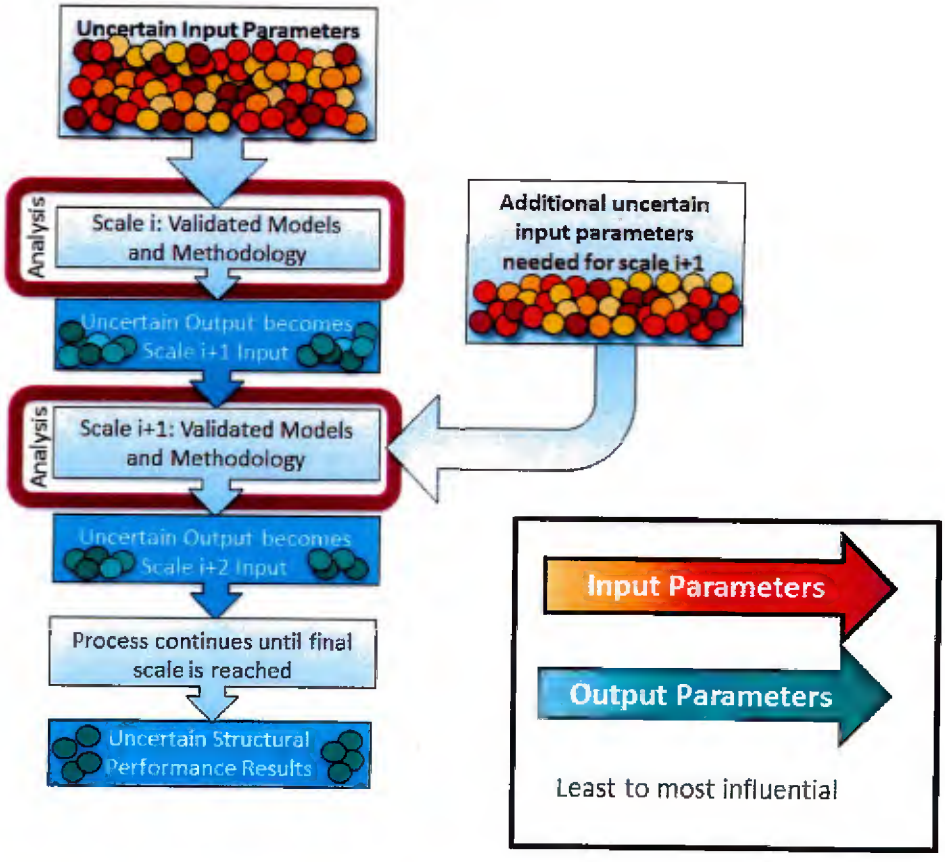

Figure 10. Uncertain input parameters at a given scale result in uncertain output from that scale. This output then becomes uncertain input at the next scale in addition to any new uncertain input parameters needed for the analysis. This process of propagating uncertainty across scales continues until the final scale is reached.

Although considerable research has been performed to study the effects of different factors on hybrid structure performance, most of these studies varied one factor a time (OFAT) with all other factors fixed to determine the influence of the factor on the outcome. OFAT is proven to be inadequate as a sensitivity analysis tool due to the limitations on estimating the global influences and interactions of inputs [5]. It is necessary to conduct a global sensitivity analysis considering the interactions between different factors to obtain reliable sensitivity information. Iooss and Lematre [6] reviewed the distinction, advantages, cost, and application of a variety of available global sensitivity analysis techniques. The variance-based method (also known as Sobol Indices) [7, 8] is used in the probabilistic toolkit to measure the influence of individual parameters and their interactions through variance calculations within a sample space. Sobol indices measure the influence of a parameter or set of parameters by delineating the contribution of each input to the total variance of the response. The process allows calculation of first-order effects (i.e. the influence of individual variables by themselves), higher-order effects (i.e. the contributions of combinations of variables together), and total effects of single input parameters. The value of this approach is that in addition to the single parameter evaluations, the Sobol index can be calculated to measure second-order effects for paired parameters, as well as any higher-order effects.

To calculate Sobol Indices, a model is described in the following form,

$$Y = f(\boldsymbol{X}),\ \boldsymbol{X} = \{X_1, X_2, X_3, \dots X_m\} \tag{1}$$

where $\boldsymbol{X}$ is the vector of m inputs, Y is the model output, and f is a square integrable function. The Sobol indices consider an expansion of the function in the following way,

$$f(X) = f_0 + \sum_{i=1}^{m} f_i(X_i) + \sum_{i<j}^{m} f_{ij}(X_i, X_j) + \cdots + f_{1,2,\dots,m}(X_1, X_2, \dots, X_m) \tag{2}$$

in which f_0 is a constant, other terms are functions of corresponding inputs and each term has a zero mean. Consequently, we can obtain the following equation by squaring both sides of Eq. 2.

$$V(Y) = \sum_{i=1}^{m} V_i + \sum_{i<j}^{m} V_{ij} + \cdots + V_{1,2,\dots,m} \tag{3}$$

where $V(Y)$ is the variance of Y, V_i is the variance of $f_i(X_i)$ and so on. Dividing both sides by $V(Y)$ of Eq. 3 yields

$$\sum_{i=1}^{m} S_i + \sum_{i<j}^{m} S_{ij} + \cdots + S_{1,2,\dots,m} = 1 \tag{4}$$

where S_i is the first-order indices, S_{ij} is the second-order indices and so on. S_i indicates the influence of X_i on the variance of output and S_{ij} shows the influence of interactions between X_i and X_j on the variance. Due to the computational intensity of computing all indices, generally only the first-order and total indices are calculated, with higher order indices calculated as needed.

The first order Sobol index for a single parameter is the ratio of two variance computations (Eq. 5). The numerator is calculated as the variance of the mean of the output parameter conditioned on a single, fixed input parameter. The mean in the numerator is evaluated numerous times across the sample space, thereby incorporating the impact across the entire space of the input parameter range. The denominator normalizes the index with respect to the variance across the entire sample space. This allows for comparison across various input parameters for the same output parameter.

An input parameter with a larger Sobol index is more impactful across the sample space than other input parameters for that same space with lesser Sobol indices.

$$S_1^i = \frac{V_{X^i}\left(E_{X^{\sim i}}\left(Y \mid X^i\right)\right)}{V(Y)} \tag{5}$$

The total index is the total contribution of one factor to the output variation. For example, the total index of X_1 for a model with three inputs is described as Eq. 6.

$$S_{T1} = S_1 + S_{12} + S_{13} + S_{123} \tag{6}$$

The total effects of a parameter attempt to identify not only the independent parameter effects, but effects due to all interactions with the parameter under investigation. While the calculation to independently measure the Sobol index for all higher-order effects can be performed to develop this total effects index, Eq. 7 demonstrates the commonly utilized analog which evaluates the total effects as unity minus the effects of all parameters except that under evaluation. This alteration provides a significant improvement to the computational efficiency of the process.

$$S_{Ti} = 1 - \frac{V[E(Y|X_{\sim i})]}{V(Y)} \tag{7}$$

where $E(Y|X_{\sim i})$ is the conditional expectations of the output Y when the input X_i is not included. The set of all S_i and S_{Ti} allows a fairly good estimation of the model sensitivities at a reasonable cost [8].

A parameter with a large total effect index is identified as a parameter with a large impact on the output parameter. Further, the comparison of the first-order effect and total effect provides an indication of the impact of interaction with other parameters. For a parameter with comparable indices, the interaction with any other or all other parameters is small, yet a parameter with a large total index in comparison to the first-order effects indicates that the parameter is impactful through interaction with other parameter(s). To investigate the effects of interacting parameters, higher order Sobol indices can be computed. It should be noted that all parameters investigated in the current effort are considered as independent parameters. Correlation and dependency was not included in analyses and should be accounted for in future work.

2.2 Surrogate Modeling

Most of the multi-scale models developed for this research effort are of high fidelity to accurately represent the behavior of the material behavior or damage mechanism(s) under consideration. These models are computationally expensive (some requiring 10-20 compute hours per analysis), and their multiple realizations are infeasible for sensitivity analysis on a large number of input parameters. For example, one of the macroscale models that captures multiple damage mechanisms requires 20 compute hours per analysis. If the parameter space is limited to only 41 material properties (neglecting configuration parameters and model form error parameters) and only 3 values are sampled (low, mean, and high) for each parameter then 3.6473E+19 high fidelity FE models must be analyzed equating to 7.2946E+20 computing hours to sample the design space. Given the variation in damage tolerance due to the rapidly varying contributions of the multiple damage mechanisms and effects of the parameters, this limited sampling is not adequate to capture

damage tolerance behavior between sample points and does not result in an accurate or converged Sobol analysis. A much more refined sampling distribution is needed but is computationally prohibitive, especially considering the number of models populating the multi-scale analysis approach as well as the number of uncertain input parameters.

In cases where the computational time required for a full parameter sampling using high fidelity models is prohibitive, a surrogate model can be developed to complete the sampling requirements for sensitivity analysis and uncertainty quantification. A surrogate model is an analytical approximation of a complex system (based on a limited number of data points) that predicts the relationship between the system inputs and outputs. The principle of building a surrogate model is summarized as an approximation function $\hat{f}$ of the true model function f given data collected by high fidelity computation at a finite number of input locations. With proper construction, these approximation models can mimic the behavior of the high fidelity simulation accurately at a much lower computational cost.

Data-driven machine learning was employed to develop the surrogate models. First, a set of locations in the parameter space was selected and the desired output was evaluated by high fidelity simulation at each of these locations, generating a set of independent observations of the high fidelity model response. The collected set of independent observations was then applied as the input data set to construct the surrogate model. The artificial neural network (ANN) posed as the structure of the surrogate model. ANN is a class of machine learning algorithms that utilizes a data driven approximation function $\hat{f}$ to describe information in a set of features organized in a hierarchy, where each step of the hierarchy is defined as a layer (Figure 11a). Each layer starts by utilizing the output of the previous layer as its input and ends with its output. Each node in the layers is called a neuron and represents the unit of computation in ANN, where the neuron performs a linear transformation of one or more inputs, $\sum_i^H w_i \cdot x_i + b$, followed by a nonlinear transformation, $\sigma(\cdot)$, to generate an output that serves as the input for the next layer (Figure 11b). The tunable parameters w_i in each linear transformation function is called the weight coefficient and the nonlinear transformation function $\sigma(\cdot)$ is called the activation function. In the surrogate model construction known as the neural network training process, the weight parameters are adjusted to minimize the error of the predicted value. The initial and last layers are called the input and output layers, respectively, and the intermediate layers are defined as hidden layers. The number of nodes in the input layer and output layer are determined as the number of input and output features, respectively. The construction of the machine learning based surrogate models (developed as needed for this project) were calculated using Tensorflow, an open-source software library for dataflow programming [https://www.tensorflow.org].

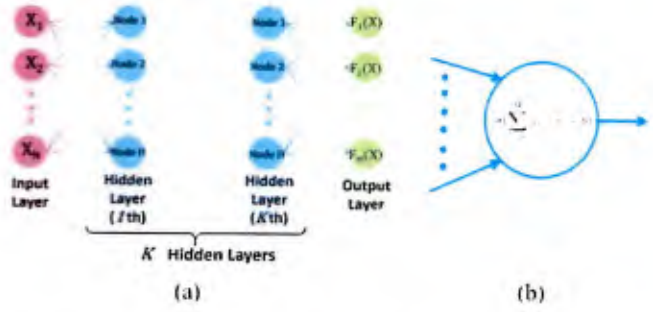

Figure 11. Schematic illustration of a typical structure (a) and the transformation of a neuron (b) in ANN.

2.3 Automated Generation of Input Files for HPC

DICE [9] (Distribution-based Input for Computational Evaluations) is a general purpose tool for preparing uncertainty quantification (UQ) and design of experiments (DOE) parametric studies. DICE was developed at NSWCCD with funding from ONR under the Ship Structural Reliability Program. DICE substitutes parameter values in text files based on user definitions of the parameters and the design of the study being performed. The input format for DICE is simple and intuitive and consists of parameter labels and definitions. The outcome of executing DICE is the entire series of ready-to-execute analyses.

DICE is executed from the command line or through a graphical interface. For every run requested for a study, DICE duplicates a specified template file and/or a directory tree and substitutes in the values for the defined parameters in the appropriate locations. The generality of its code-agnostic framework makes it extensible to any text-format file ranging from standard input files to input scripts for preprocessing software tools. Thus, DICE enables complex workflows that would be difficult to achieve with other similar tools. Furthermore, DICE is written in the Python coding language and is not operating system dependent thus successfully enabling the generation of all the files needed to perform a UQ or DOE study on both local and HPC computing assets. The tradeoff for this flexibility is that DICE plays no automated role in analysis execution or post-processing. Fortunately, many commercial codes as well as generalized visualization and plotting software programs readily support scripting.

Parameter properties are specified by the user in a parameters definition file. DICE recognizes three broad parameter types: probabilistic parameters, deterministic parameters, and derived parameters.

Probabilistic parameters are random variables whose values are sampled from the percent-point functions (or inverse cumulative distribution functions) of continuous distributions. DICE utilizes the open source statistics libraries of *SciPy* [9]. A number of common distributions are currently implemented, along with a framework for adding other distributions in the future. DICE can sample values from probabilistic parameters for each run using the Monte Carlo method [9], or using one of the currently-implemented stratified sampling techniques, including Latin Hypercube[9], partial-stratified sampling, and latinized-partially stratified sampling [9].

Deterministic parameters have user-specified values, and DICE creates runs for all permutations of the deterministic parameters, with each run corresponding to a unique permutation. Values are not limited to floating-point numbers and can include integers and strings. Additionally, DICE has the ability to group two or more deterministic parameters in the permutations, so that corresponding values from each of the grouped parameters appear in the same runs. This is advantageous for quantities such as Cartesian coordinates, where the permutations of coordinate values of a point along the global axes do not correspond to anything meaningful.

Derived parameters have values that are calculated based on the values of other parameters. For the definition of a derived parameter, the user specifies an expression, which may contain the names of other parameters in the analysis. This can be useful when, for instance, the probabilistic information for a quantity of interest is reported based normalized values. In that case, a derived parameter could be used to multiply the sampled probabilistic parameter by the necessary scale factor for the problem at hand.

2.4 Sensitivity Analysis Examples

Two representative examples are provided to demonstrate the use of sensitivity analysis to (1) guide model development and data collection and (2) identify the most influential parameters on damage tolerance. The details of both computational models are presented at length in Section 4.

2.4.1 Example 1: Sensitivity Analysis that Informs Model Development and Use

As fully described in Section 4.4, an analytical model was developed and applied to calculate the stress state at crack fronts in damaged aluminum plates. This stress state was then provided to a peridynamics model to investigate crack propagation along sensitized grain boundaries. Given the large number of runs required to perform stochastic evaluation on grain configuration and degree of sensitization, it was essential for the analytical model to provide converged and accurate results with minimized computation time. Sensitivity analysis on the crack growth model was performed to inform code optimization.

Given the propensity of cracks to branch and turn in sensitized aluminum, a branched crack (Figure 12) is discussed as a representative example of code optimization from sensitivity analysis results. The potential for crack growth at all three crack tips is evaluated for tension load applied perpendicular to crack segment 1. The angle of the branch is described by θ, and c, b, and, a are the lengths of crack segments 1, 2, and 3 respectively. The baseline configuration was $\theta = 30°$, and a=1, b=.8, and, c=5. The sensitivity analysis included all primary sources of model form error and experimental measurement error (Table 2). Model form error consisted of 5 parameters: the number of points uniquely assigned to each crack segment (the traction free condition is enforced at these points) and the number of polynomial and tip terms used in approximating the opening displacement profile of each crack segment. The experimental error was defined by 4 parameters: the measured length of each crack segment and the branch angle.

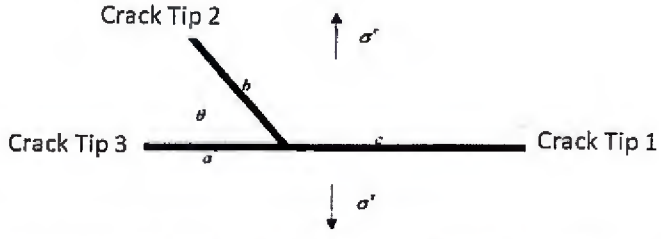

Figure 12. Branch crack example to demonstrate code optimization using sensitivity analysis results

Table 2. Parameters included for evaluation on branched crack growth under tensile loading

Model Form Error		Range of Parameter Values
X1	Number of points along crack segment 1	[10 – 70]
X2	Number of points along crack segment 2	[10 – 70]
X3	Number of points along crack segment 3	[10 – 70]
X4	Number of tip terms	[2, 6]
X5	Number of polynomial terms	[2, 6]
Experimental Measurement Error		
X6	Angle of the branched crack segment	[135*pi/180, 165*pi/180]
X7	Length of crack segment 1	[4.5, 5.5]
X8	Length of crack segment 2	[.72, .88]
X9	Length of crack segment 3	[.9, 1.1]

Sensitivity analysis results for these 9 parameters on the mode I and II Stress Intensity Factors (SIF) at each crack tip are shown in Figure 13. Although 800,000 samples were required to obtain convergence for the Sobol Indices, a surrogate model was not needed for this example as the analytical code runs in seconds for a single model. While some parameters exhibited elevated influence on individual SIFs, the number of polynomial and tip terms dominated for all outputs evaluated. Therefore, convergence and accuracy studies focused on these two parameters. And, model form parameters were clearly more influential than experimental measurement error.

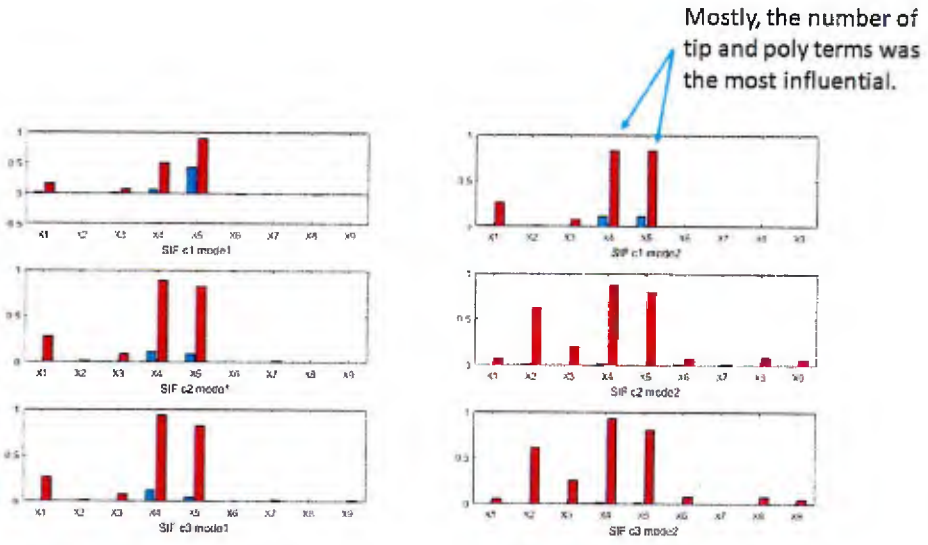

Figure 13. Sensitivity analysis results for the mode I and II SIFs relative to all 9 parameters encompassing both model form and experimental measurement error.

To determine the most accurate and converged model for a minimal computational cost, an evaluation of the number of polynomial and tip terms was conducted (for example Figure 14, shows a plot of the influence of these two parameters on the mode I SIF at crack tip 1). The conclusion of this study was that 4 terms were needed each to accurately capture crack opening displacement with minimal computational time. Once these two parameters were set, it was then determined that 10 points along each crack length provides an adequate number of points to enforce the traction free condition at crack faces.

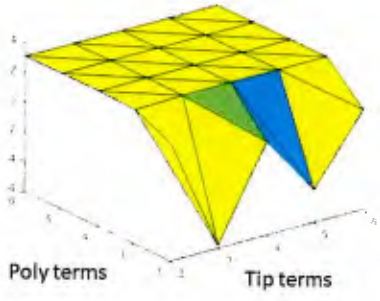

Figure 14. The variation in the Mode I SIF at crack tip 1 relative to the number of polynomial and tip terms included in the crack displacement profile.

Once a model with acceptable accuracy, convergence, and computation time was identified, the effects of measurement error on crack growth prediction was evaluated separately with this final model. Sampling was conducted at 3,950,886 points at a computational cost of 23.4 hours. While the results shown in Figure 15 are not fully converged, it is clear that all measurement values are important to fully explore crack growth at all tips. Therefore, care was taken when determining values for the branch angle and crack tip lengths from experimental test results.

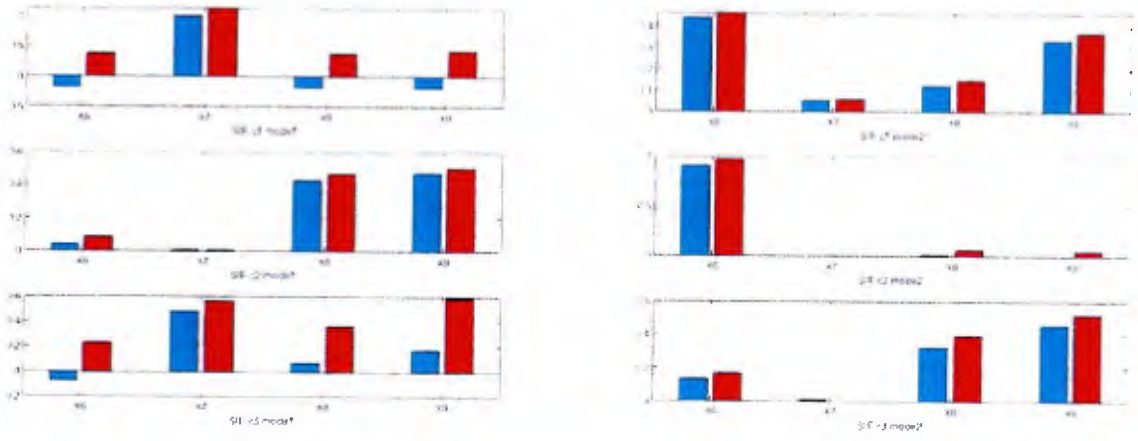

Figure 15. Sensitivity analysis results for the mode I and II SIFs at all crack tips relative to the 4 parameters encompassing experimental measurement error.

2.4.2 Example 2: Identification of the Most Influential Parameters on Crack Growth

A variation of the high fidelity FE model discussed in Section 4.5 is investigated to identify the most influential parameters on the crack arrest performance of a baseline composite patch under static loading. This version of the hybrid structure FE model consists of a rectangular aluminum plate with a through thickness crack at the center, the composite patch modeled using smeared composite properties, and the metal/resin interface (Figure 16).

The FE model is shown in Figure 17. Symmetric boundary conditions were applied. The thickness of the cohesive layer representing the metal/composite interface is 0.001 inch. The solid element C3D8R is used to mesh the Al 5456 plate. The e-glass/epoxy composite is meshed with the continuum shell element SC8R, and the interface layer is meshed with cohesive element COH3D8. Material properties are provided in Table 3 and Table 4, respectively. Prior investigation and engineering judgement identified the highlighted parameters as the most influential, and these were selected for a detailed sensitivity analysis. As shown in Figure 18, crack growth is proportional to disbond area, therefore, crack extension was used as the output parameter for the sensitivity study.

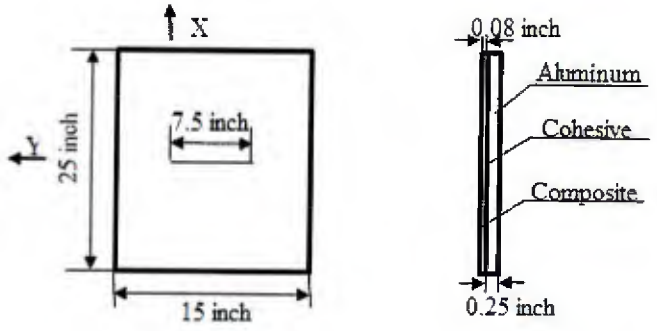

Figure 16. Configuration of the test specimen.

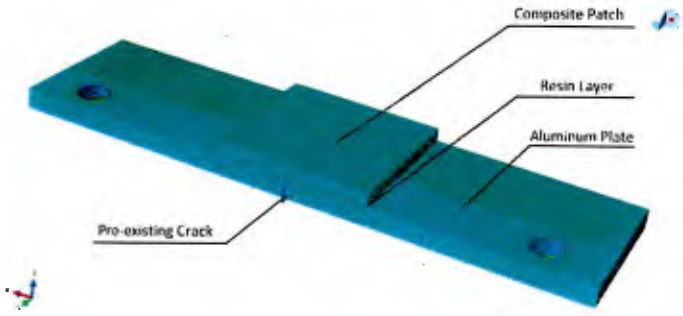

Figure 17. Symmetric FE model to investigate crack growth under static loading.

Table 3. Properties of the cohesive elements used to model the metal/composite interface

E/psi	G_I(GI_coh) /(lbf/inch)	G_{II}, G_{III} (GII_coh)/(lbf/inch)	Exponential of BK Law (n)	Normal damage initiation strength (InN_coh)/psi	Shear damage initiation strength (InS_coh)/psi
1.16E+07	6.28	16.5	2.6	6154	4308

Table 4. Properties for Al 5456 represented with a Johnson Cook Hardening Law

E/psi	v	Ultimate Strength /psi	Fracture Energy (J) /(lbf/inch)	Johnson Cook Hardening Law			Damage initiation strength of traction-separation law	
				A/psi	B/psi	n	Normal (InN_Al) /psi	Shear (InS_Al) /psi
1.01E+07	0.29	5.2E+04	152	2.98E+04	1.036E+05	0.607	52000	31200

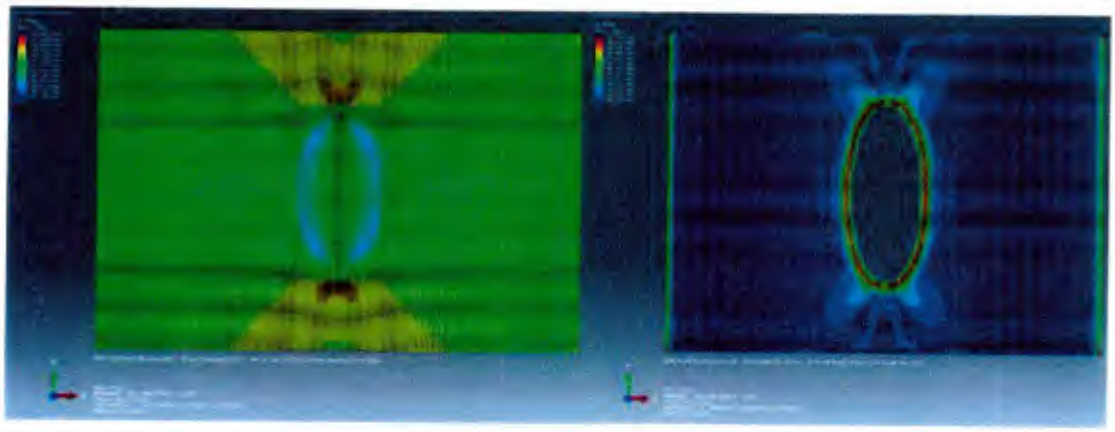

Figure 18. Simulation results showing that crack extension (left) is proportional to disbond growth between the metal/resin interface (right). Disbond area was in the shape of an ellipse, and the change in length of the ellipse is proportional to crack growth.

The number of samples analyzed with FE simulation was 95, and the input files were generated using DICE. Analysis was performed on the DoD HPC system, COPPER. Given the time required to run a single simulation, a surrogate model was constructed from the FE results using ANN as described in section 2.2. Latin Hypercube sampling with 6 strata for each of the investigated parameters (6^8 = 1,679,616 total samples) was performed to calculate the input for the sensitivity analysis. Even for this relatively low fidelity model, sensitivity analysis would have been infeasible without the use of the surrogate model, even with HPC resources. First order and total Sobol Indices were calculated as described in Section 2.1, and the results are shown in Figure 19. It is interesting to note that the properties of the metal, specifically the crack initiation parameter were substantially more influential than the interface problems for this specific case. Also, each parameter was treated as independent in the analysis, although some parameters are correlated. Based on these results, experimental test data was obtained for these most influential parameters for improved model predictions.

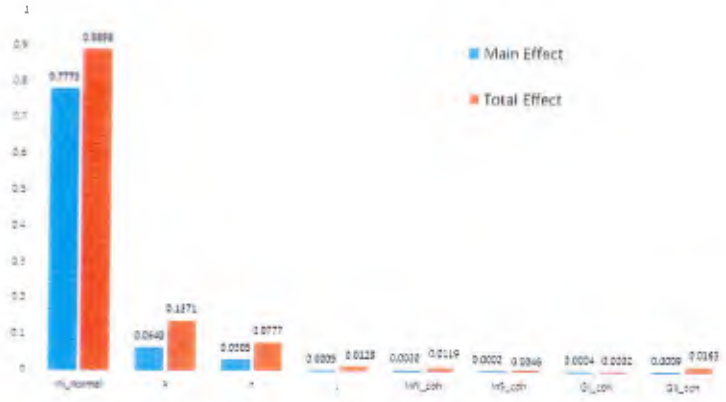

Figure 19. Sobol Index results from the sensitivity analysis indicate that the metal properties are more influential than the interface properties.

3 Experimental Testing for Characterization and Model Validation

As influential physical behaviors and material properties were elucidated from the concurrent sensitivity analysis during the multi-scale model development, experimental testing was performed to fill in knowledge gaps and generate validation data. The following sections outline the primary experimental testing done for validated model development, however some coupon testing was also performed to characterize material properties. This data is available on request.

3.1 Shear Strength at the Bondline

Widespread adoption of composite-metal joining signals a pivotal shift as customized parts and materials selections are optimized for specific applications. Creating interfaces between dissimilar materials that play to the strengths of each material while mitigating their weaknesses has been an enduring challenge when designing hybrid structure [10]. Traditional joining methods, such as bolts or rivets, can generate unacceptable damage in the composite, and co-cured joining is one technique to overcome this problem. Co-cured joints are an attractive solution, as they avoid damage to load bearing fibers, reduce stress concentrations in the substrates, are less prone to fatigue, and do not suffer from some of the manufacturing pitfalls associated with fabrication of bolted joints in composite materials, such as dependence on fastener hole tolerance [10-17]. While co-cured joints offer many advantages, a major disadvantage is that bondline failure is a non-visible damage mechanism requiring non-destructive inspection, which poses significant evaluation challenges. Small disbond areas that may be challenging to detect during inspection can create initiation sites for damage propagation and potential joint failure. Such interface disbond can occur under service loading such as bending, fatigue, or low velocity impact.

Improved understanding of the physics of bondline behavior and the manufacturing and installation processes that are most critical to requirements, can not only lead to improved bondline damage tolerance but also to efficient and reliable inspection schedules for bondline damage. The testing and corresponding FE models presented in this and the following section aimed to better understand bondline failure and to investigate the influence of parameters on the individual damage mechanism of disbond at the metal/resin interface. Four outputs are needed to propagate into the high fidelity FE model described in Section 4.5: normal and shear strength at the interface and normal and shear fracture at the interface. During model development, it was determined that acceptable accuracy was obtained by using the tensile strength of the resin. Therefore, experimental testing focused on characterizing the shear strength and fracture behavior relative to surface roughness to investigate bondline performance relative to installation guidelines.

Traditional lap shear testing was performed to capture shear failure at the bondline and was found insufficient due to not only the induced bending moments exacerbated by the large differences in material stiffness but also due to the inability to isolate failure along the interface. Traditional double lap shear (DLS) and single lap shear (SLS) test specimens did not control the failure surface and allowed for adhesive failure at multiple adhered surfaces and cohesive failure inside the adhesive matrix. Therefore, a test geometry was developed to force a pure-shear failure along a single contiguous interface. The new test geometry creates similar loading conditions as the fiber pushout test described by Liang and Hutchinson but at a much larger scale [18]. The test geometry, test fixture, and corresponding FE model with quarter-symmetry are shown in Figure 20. By constraining the adhesive and loading very near the interface, a pure shear failure mode at the

interface is achieved. Potential issues included matrix yielding or cracking prior to bondline failure. Analysis of these issues is addressed in later sections.

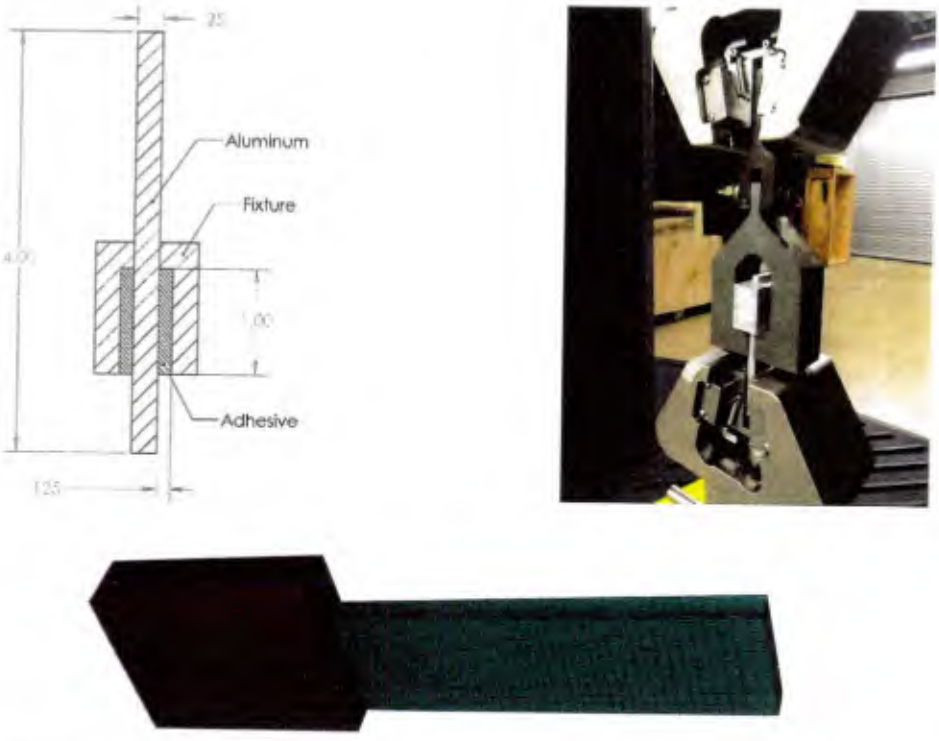

Figure 20. The test specimen dimensions, test fixture, and corresponding FE model used to investigate shear failure at the metal/resin interface.

Testing focused on varying surface preparation methods, specifically sandpaper grit level and application method. On ship, access to specific sandpaper grit levels or machine sanding tools is unreliable at best. Additionally, there may be areas of a given structure on which access to the surface using machine sanding tools is limited. Commonly available 60 and 180 grit abrasive papers were chosen for the study. Likewise, double action machine sanding and hand sanding were chosen for comparison due to their common use and availability. The effects of resin thickness were also investigated. The test matrix presented in Table 5 was followed to conduct the investigation of surface roughness effects and to characterize shear strength of the interface for input into FE models. Test materials used for initial testing are listed in Table 6.

To quantify the sensitivity of the test results to specimen geometry, two different test fixtures were created. The first, listed in Table 5 as "Thick Adhesive", created specimens with a 1/8 in thick adhesive layer surrounding the aluminum specimen. The second, described as "Thin Adhesive" resulted in a 1/16 in layer of adhesive. It was determined through previous experiments that adhesive thicknesses less than 1/16 in would result in deformation of the aluminum sample fixture.

Table 5. Test Matrix

ADHESIVE PULL OUT TEST	
TEST SPECIFICATION	**SAMPLE COUNT**
DA SANDER 60 GRIT ABRASIVE	
THICK ADHESIVE	5
THIN ADHESIVE	3
DA SANDER 180 GRIT ABRASIVE	
THICK ADHESIVE	5
HAND SANDING 60 GRIT ABRASIVE	
THICK ADHESIVE	5

Table 6. Material Specifications

ADHESIVE PULL OUT TEST MATERIALS	
ALUMINUM ADHEREND	5456-T116 .25" PLATE
EPOXY ADHESIVE	PROSET M1002/M2046
SURFACE CLEANER	PPG DX-579
SURFACE BOND TREATMENT	3M AC-130-2
	LOCTITE FREKOTE
FIXTURE RELEASE	770NC

Prior to bonding, the aluminum surfaces were thoroughly cleaned and a surface pretreatment applied. Test specimens were prepared using the following procedure:

1. Thoroughly remove obvious debris from surface of metal using Scott brand blue paper shop towels.
2. Wipe off any oil or wax based material manufacturing stamps using acetone.
3. Scrub surface with bristle brush and PPG DX-579.
4. Abrade surface using chosen method of surface abrasion for a minimum of two minutes per sample side. When using the DA sander, light pressure was used to allow for free rotation of the sanding disk and sander motion was alternated between vertical and horizontal strokes. When hand sanding, circular and "cross-hatch" patterns were alternated while frequently rotating the specimen 180 degrees to ensure even sanding coverage.
5. Reclean surface of aluminum with bristle brush and 579 metal cleaner. Repeat until wiping with shop towel returns clean surface.
6. Apply 3M AC-130-2 surface pretreatment to part per 3M specifications and allow to cure.

Once surface preparation was complete, specimens were bonded as quickly as possible to reduce the likelihood of surface contamination. Prior to assembly the specimen fixtures were treated with Loctite Frekote 770NC non-transferring release. This step was performed to allow for the fixtures to be reused. To prevent contamination, the fixture was slid onto the part from the upper non-bonded area of the sample, being careful not to touch the bond area or allow it to contact the released metal surface of the specimen fixtures. Once the proper positioning was achieved, the fixtures were sealed to the specimens using RTV silicone and allowed to cure. The RTV silicone serves the dual purpose of sealing the sample, allowing for pouring of the adhesive, and affixing the sample to the fixture while the adhesive is curing. Alignment of the samples with the fixtures was enforced by tight tolerancing of the interface between the sample and the fixture.

With the specimens assembled and the RTV silicone curing, 375g of Proset M1002 resin was mixed with 90g of M2046 hardener. During the mixing process, the introduction of air into the

mixture was minimized by using slow, deliberate mixing motions and an extended mix time. To ensure thorough mixing and complete incorporation of the two part system, both the sides of the mixing bucket and the stir stick were scraped down multiple times. This epoxy was then poured into the fixtures and allowed to gel. After an overnight room temperature gel the samples were post cured at 60C for 8 hours. The completed samples are shown in Figure 21.

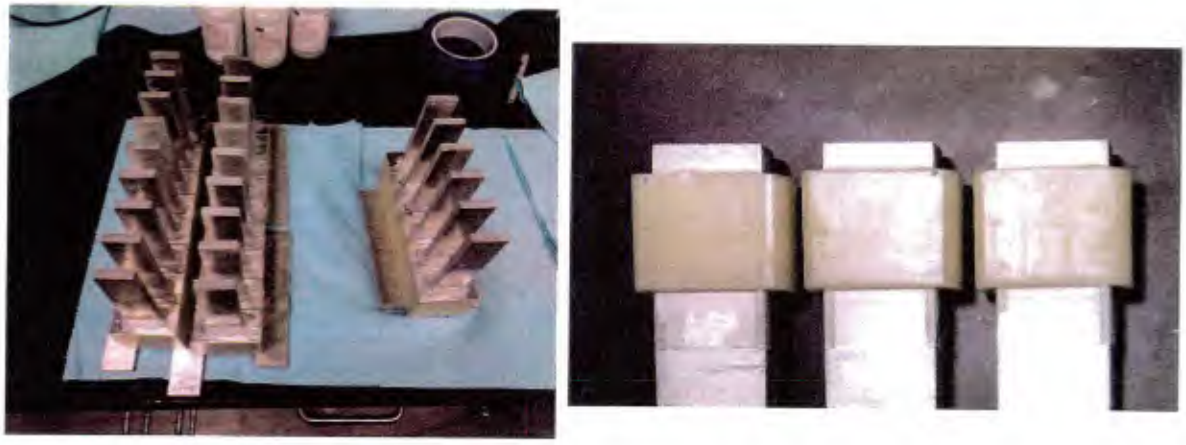

Figure 21. The completed specimens prior to testing.

Testing was performed on an MTS tensile testing machine using a 100kN load cell. The pin joint was added after initial testing showed that when clamping the upper hook directly there was high sensitivity to any misalignment introduced during clamp up. The samples were centered on the hook, allowed to hang naturally, and then clamped by the lower grip. Preload during clamp up was found to be below 100N at all times. The load cell used shows noise at zero load in the range of $\pm$20N. Due to these factors all measurements taken have been treated as accurate to $\pm$100N at peak load. With peak loads ranging from 30-40kN, this represents a maximum measurement induced error of approximately 0.3%. Load was applied via displacement control at 0.1 mm/s until ultimate failure was achieved.

Figure 22 shows test results for the investigation of thick and thin adhesive specimens prepared with the DA sander and 60 grit abrasive. While maximum force measurements seem to be within similar ranges, the failure mode differs for each sample geometry. The thin specimens failed progressively, with extended post-peak stiffness degradation. Visual inspection of the thin samples during testing showed fracture surfaces progressing towards the final upper boundary of the adhesive at differing rates on each side of the sample, which may account for the stepped post-peak behavior observed. Conversely, the thick samples exhibit a sudden onset of failure with complete stiffness loss occurring almost instantaneously. These samples exhibited the classic sudden shear failure mode expected of this test geometry. Upon close inspection, it was found that significant internal damage to the adhesive occurred in the thin samples while it was limited in the thick samples, with only a few specimens showing some matrix cracking. This behavior can be seen by comparing the post-failure surfaces of the adhesive shown in Figure 22. Note the vertical crack in the thin adhesive sample indicated by the arrow and the deformation at the top edge of the sample. Due to these issues, the thick adhesive was chosen as the primary test geometry. This test

geometry forces interface failure and limits deformation or damage in the resin (a source of energy absorption that could impact the accurate determination of the failure behavior at the interface).

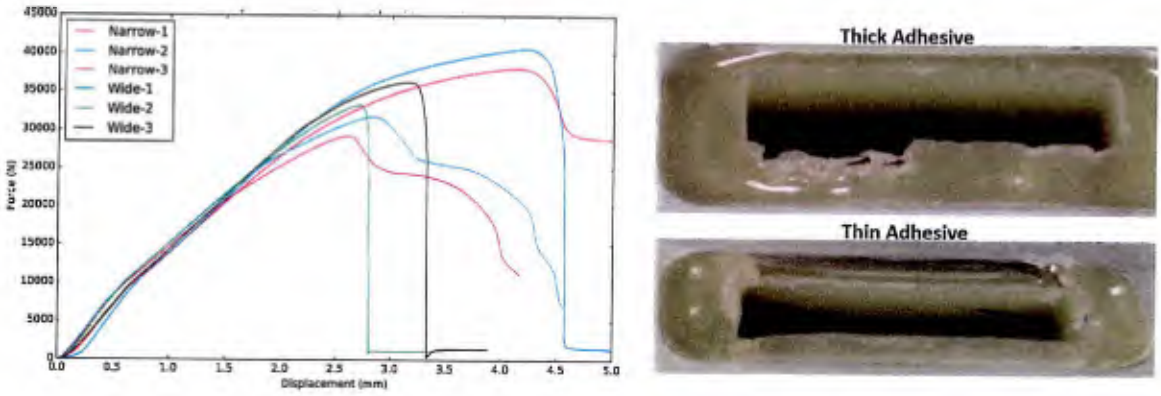

Figure 22. Results from the investigation of adhesive thickness on bondline shear strength.

The results from the remaining testing to compare the effects of surface preparation techniques is provided in Figure 23, Figure 24, and Figure 25. Table 7 presents the upper and lower bounds of each group of specimens as well as the standard deviation. Note the similarity in the test results for each type of surface preparation. More testing is necessary to truly determine whether a given test method results in superior bond performance, but of note is the reduction in standard deviation seen for the 180-grit preparation method. It is possible that the smoother surface results in more even stress transfer between the adhesive and adherend or that the smoother surface avoids stress concentrations caused by surface imperfections left by the other preparation methods. It appears from the raw data that the hand sanded samples performed better on average and in deviation from the average than the machine sanded samples, but it is worth noting that during fabrication of DA60-2 a small scratch was found on the sanded surface prior to application of the AC-130-2 surface treatment. At the time, it was considered a minor imperfection and noted, but in light of the poor performance of DA60-2 in comparison to the majority of the DA60 specimens it is possible that this surface imperfection contributed to an early failure. If DA60-2 is removed from the sample set, the standard deviation and average strength values improve significantly. Even with this improvement, the three surface preparation methods resulted in data so closely grouped it is difficult to make a determination as to which surface preparation method is superior.

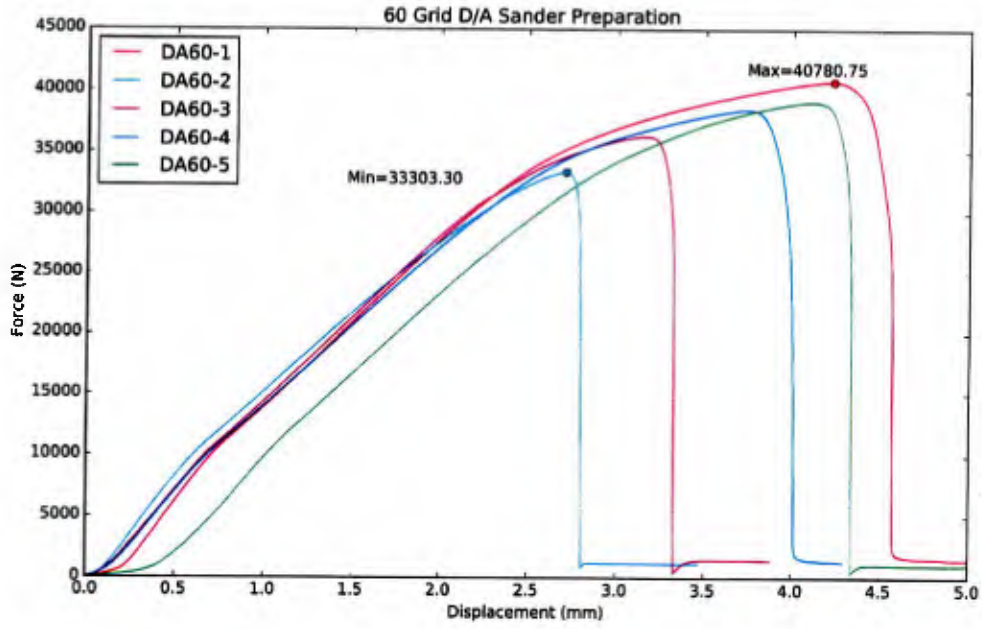

Figure 23. Test results for specimens prepared using a DA sander and 60 grit abrasive

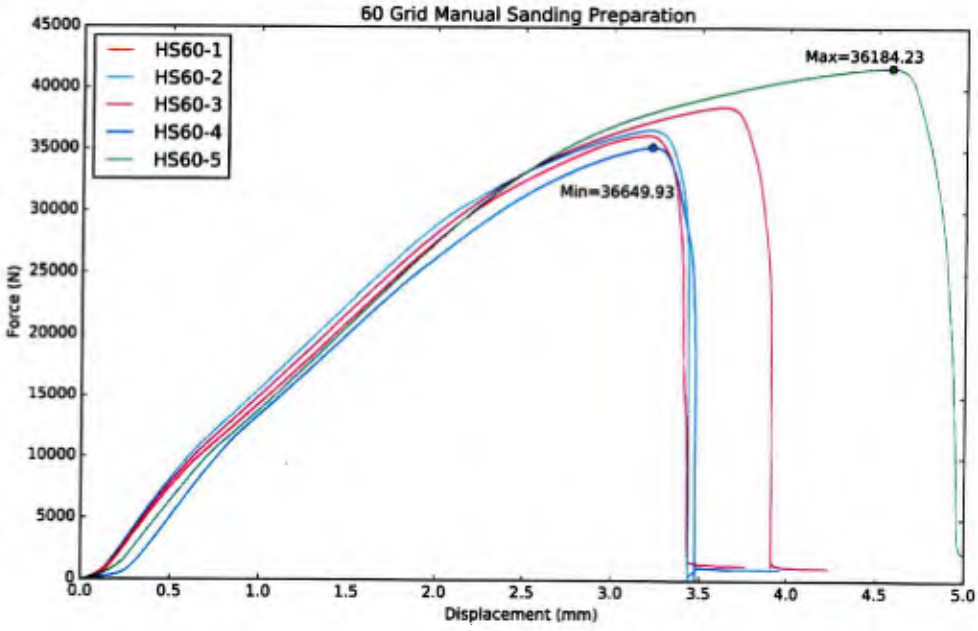

Figure 24. Test results for specimens prepared using manual sanding with 60 grit abrasive

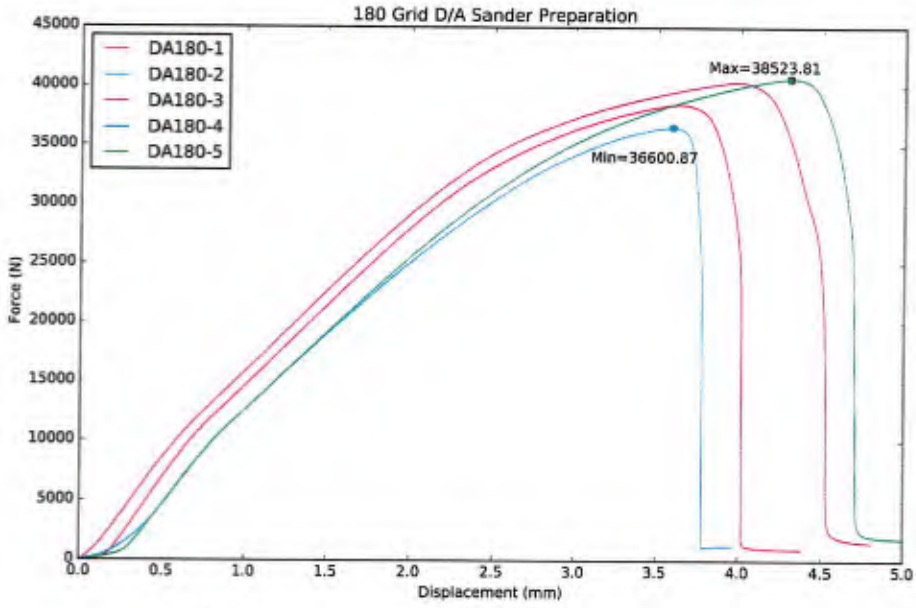

Figure 25. Test results for specimens prepared using a DA sander and 180 grit abrasive

Table 7. Statistical values for the varying surface preparation techniques

	DA60 (N)	DA180 (N)	HS60 (N)	DA60 minus DA60-2 (N)
Average	37591	39389	37671	38663
Max	40781	40707	41767	40781
Min	33303	36601	35230	36278
STDev	2584	1614	2312	1613

Images of the aluminum surface were taken both prior to and after testing using a Keyence digital optical microscope and a 1000x lens. Using the depth-up function of the Keyence microscope, initial surface form measurements were generated. The resolution of the Keyence system is not sufficient for detailed analysis of the surface roughness but provides data for model development and visual inspection of the surfaces. The 3D representation shown in Figure 26 and Figure 27 use a 4x multiplier on the depth measurement to aid visual inspection of the imaged surfaces of 60-grit DA prepared and 180-grit DA prepared surfaces respectively. Note the large difference in both the uniformity and size of surface scratches left by the different grit levels.

The surface of the same specimens was also imaged after testing to failure. Initial visual inspection indicated failure occurred at the interface, but inspection at 1000x showed significant amounts of resin still bonded to the aluminum surface, as shown in Figure 28 and Figure 29. The amount of remaining resin varied from sample to sample and surface preparation type, but the 180 grit samples consistently had the least resin remaining on the surface after failure. It is possible that the 180-grit samples failed in a more consistent failure mode than the 60-grit samples, leading to both the tighter bounds on the failure strength and the more consistent failure surfaces.

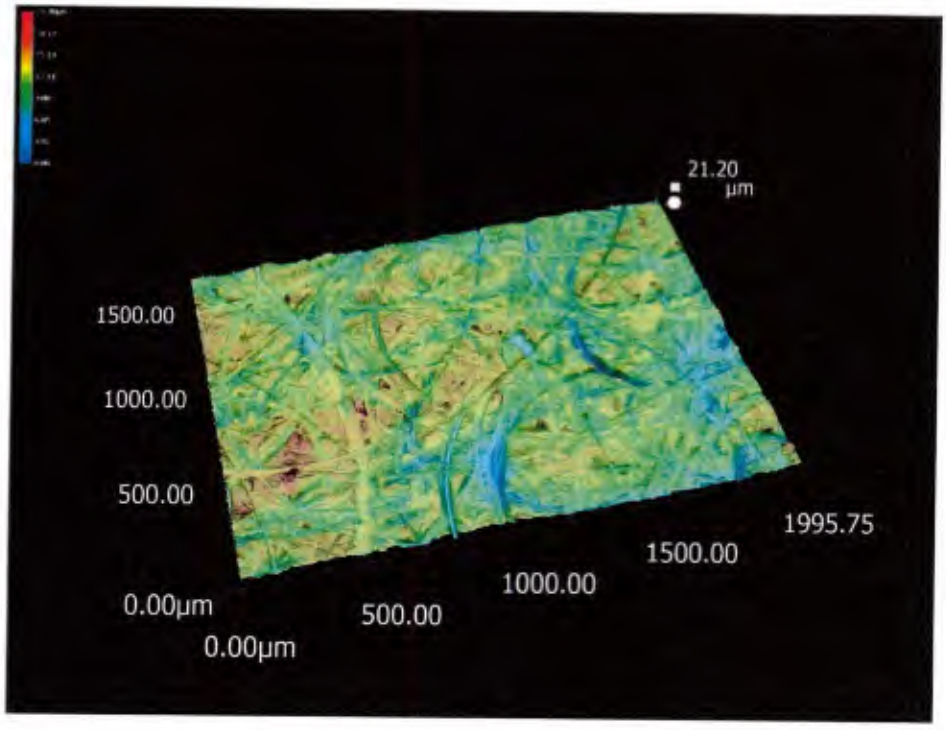

Figure 26. 1000x digital optical microscope image of DA sanded 60-grit prepared surface.

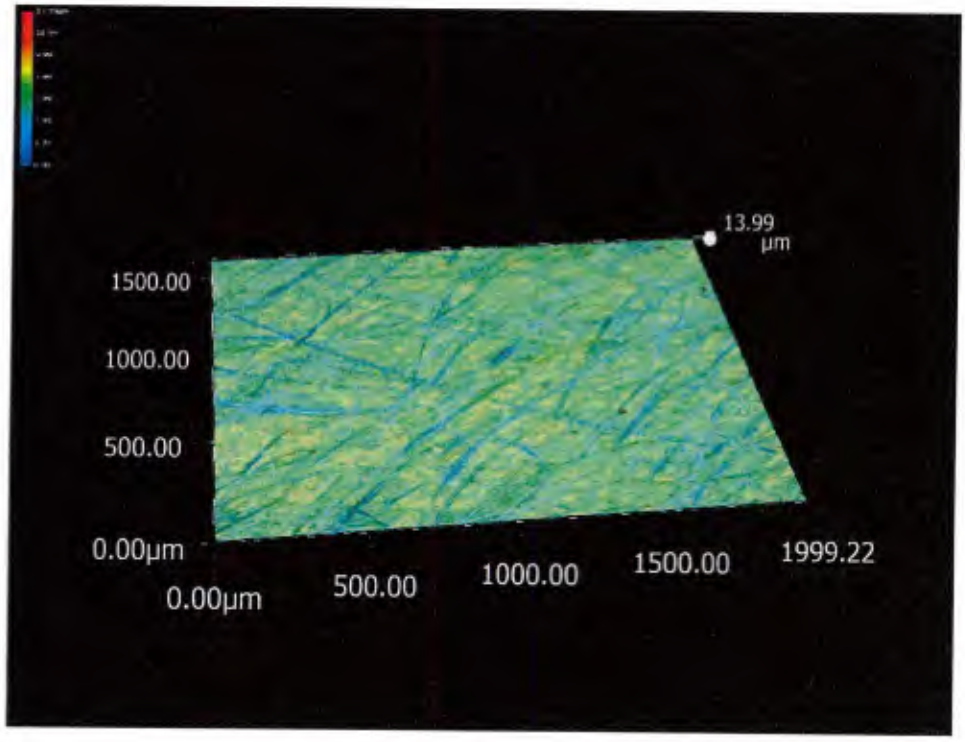

Figure 27. 1000x digital optical microscope image of DA sanded 180-grit prepared surface.

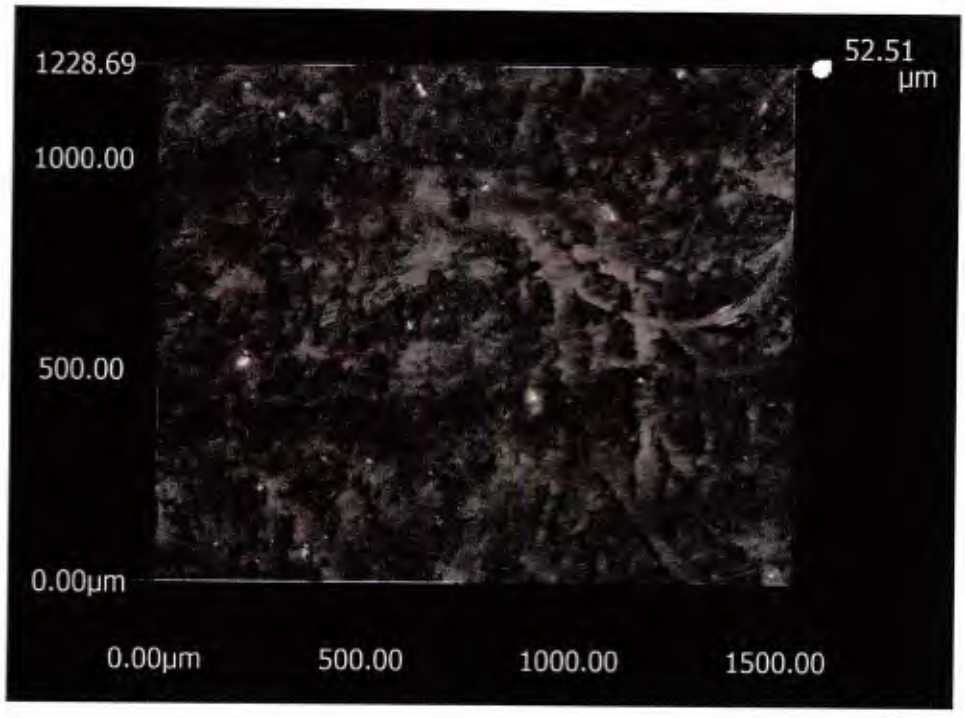

Figure 28. 1000x digital microscope image of post failure DA60 surface.

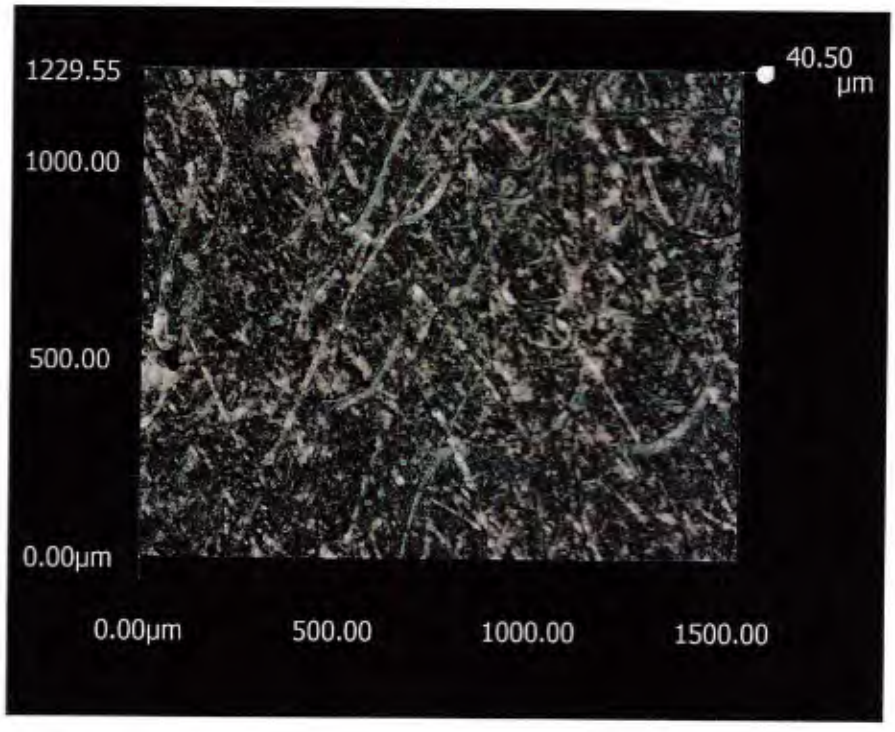

Figure 29. 1000x digital microscope image of post failure DA180 surface.

3.2 Fracture Properties at the Bondline

Critical strain energy release rate, G_c, is a property that quantifies a material's resistance to fracture in the presence of a crack and is a critical parameter when designing an adhesively bonded joint [19]. It is important to understand the failure under normal loading, mode I, and shear loading, mode II, and it is just as important, if not more so, to study the behavior of a material under mixed-mode I+II loading. This is because materials are rarely ever loaded in the pure normal or shear directions, but more often a combination of both, creating a mixed-mode situation. It is therefore necessary to develop failure criteria that includes these combined loading effects [20].

The double cantilever beam (DCB) test is one of the most popular for determining mode I fracture toughness [21]. The DCB specimen consists of two uniform thickness rectangular shaped adherends, with adhesive in the middle and an unbonded portion located towards the front. This is chosen because of the relatively simple test setup and universal specimen geometry that can be used for further obtaining modes II and I+II G_c values. More information on the DCB test can be found in [22].

The end-notched flexure (ENF) test is chosen for determining G_c in mode II. As with the DCB, this test has the benefits of having a simple test fixture and the same specimen as the DCB test. Difficulty in monitoring crack propagation and unstable crack initiation are common issues with this test and are addressed later in this report.[23]

The single leg bend (SLB) is used for determining the mixed-mode (I+II) G_c. The SLB is a common mixed-mode test and is chosen because it requires no additional testing equipment beyond what is required for the ENF, and uses only a modified DCB specimen. [24]

Specimens adherends are composed of 5456 grade aluminum. This is a high strength, marine grade aluminum often used in saltwater environments. The yield strength of this material is 228 MPa and has a modulus of elasticity of 71 GPa. The adhesive is a 2-part ductile laminating epoxy from PRO-SET, M1002/2046. This material has a tensile modulus of 3,000 MPa and tensile strength of 69 MPa.

The DCB specimen consists of two uniform thickness rectangular shaped adherends bonded with an adhesive. An initial delamination length provides a location for crack initiation. The specimen used for the ENF test is the same as used in the DCB and is also modified for use with the SLB tests. These geometries are presented in Figure 30.

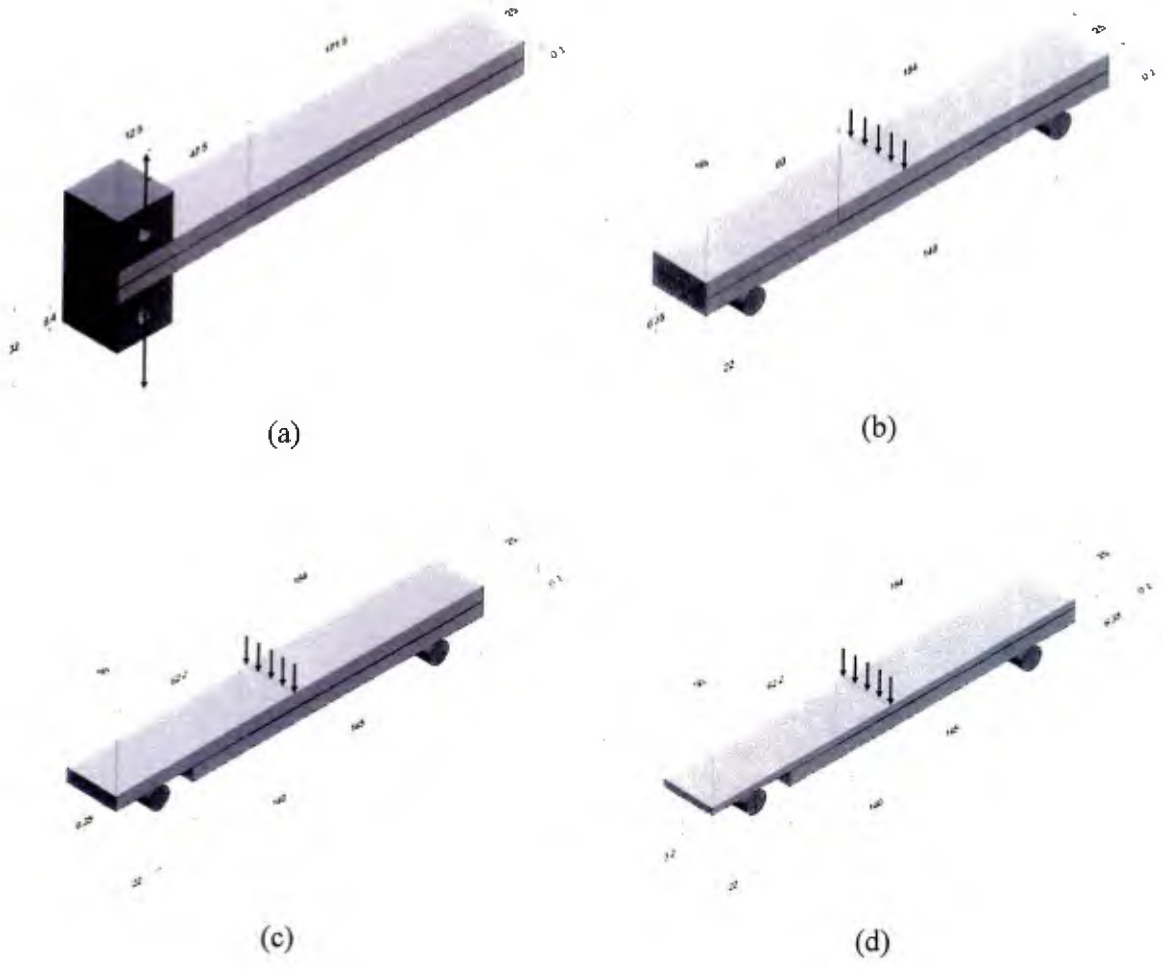

Figure 30. Specimen configurations for (a) DCB, (b) ENF, and (c), (d) two variations of SLB tests

Raw aluminum plates were cleaned with acetone and sanded to remove surface contaminants. 3M® AC-130-2 surface pre-treatment was applied to the sanded surfaces and allowed to dry for at least 60 minutes. 50-micron thick Teflon tape was applied to the interior surface of the specimens to reduce friction and provide an initial delamination span in this area. 100-micron glass beads introduced in the epoxy mixture maintained a constant adhesive layer thickness of .1 millimeters. Vacuum bagging was used during the curing process to provide uniform pressure across the plates during the curing process. Curing was done in a drying oven at 60°C for 4 hours. Specimens were precision cut to final size using a waterjet machine.

Various sanding methods and grits were used to prepare the specimens to study the impact on G_c. 40-120-180 grit, used respectively, and 40 grit, exclusively, were used for specimen preparation. Each was applied using two methods: hand and electric handheld random orbit sander. Table 8 below lists the preparation methods by group.

Table 8. Specimen group according to preparation method

Group	Application Method	Grit
A	Orbital	40-120-180
B		40
C	Hand	40-120-180
D		40

The orbital sanding was performed with moderate pressure in random zig zag patterns. The resulting finish was a consistent, uniform surface finish having no predominant surface pattern. Hand sanding used moderate to heavy pressure, applied with 4 fingers in a clockwise/counter-clockwise random circular motion. This method, in contrast to the uniform surface from the orbital, showed obvious swirling surface patterns. The prepared surfaces are shown in Figure 31. Sanding for both steps was complete when the oxidation layer was visually removed, and surface felt adequate to the touch.

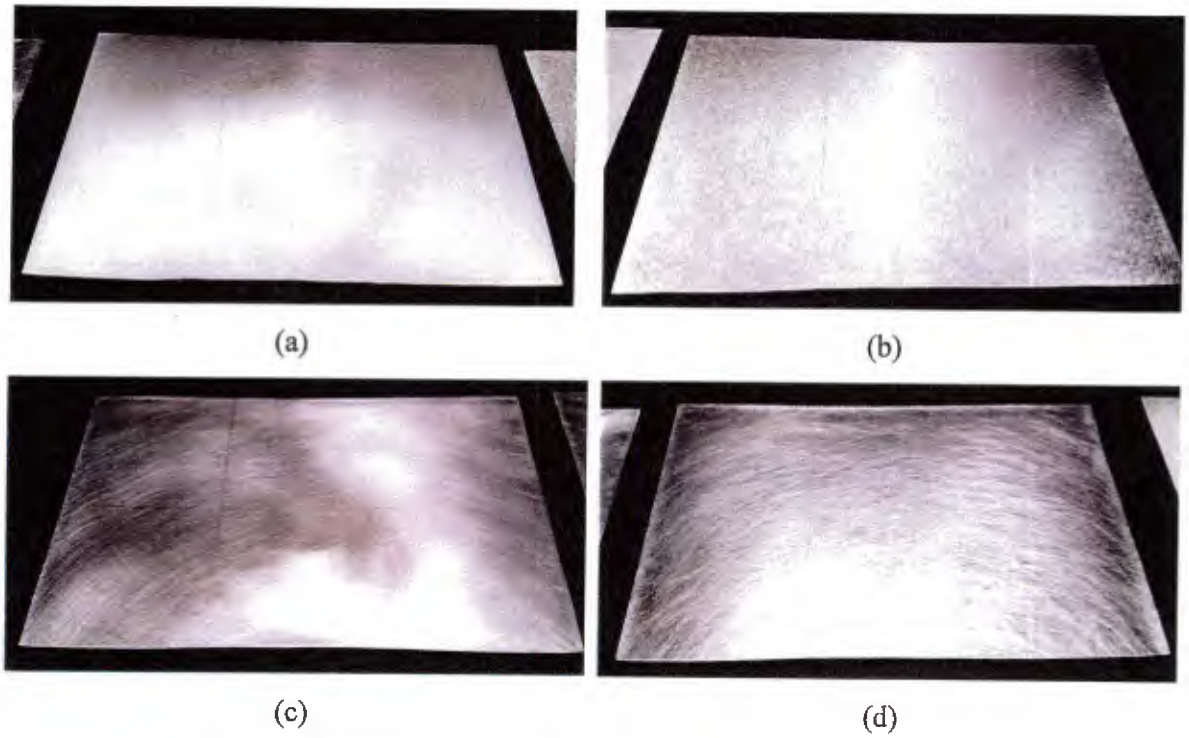

Figure 31. Surfaces for specimen groups A, B, C, and D

Testing was performed on a calibrated MTS universal testing machine using 10kN and 100kN load cells. Loading blocks were attached to the DCB test specimens using four #10-24 UNF screws. Hinge plates were attached to these loading blocks via pins and the hinge plates attached to the testing machine using tensile grips. The ENF and SLB test setups used rollers for the specimen supports and load application. The experimental setups are shown in Figure 32. Displacement was applied for all experiments at a rate of .50 mm/min. Opening displacement and load versus time were recorded during the test.

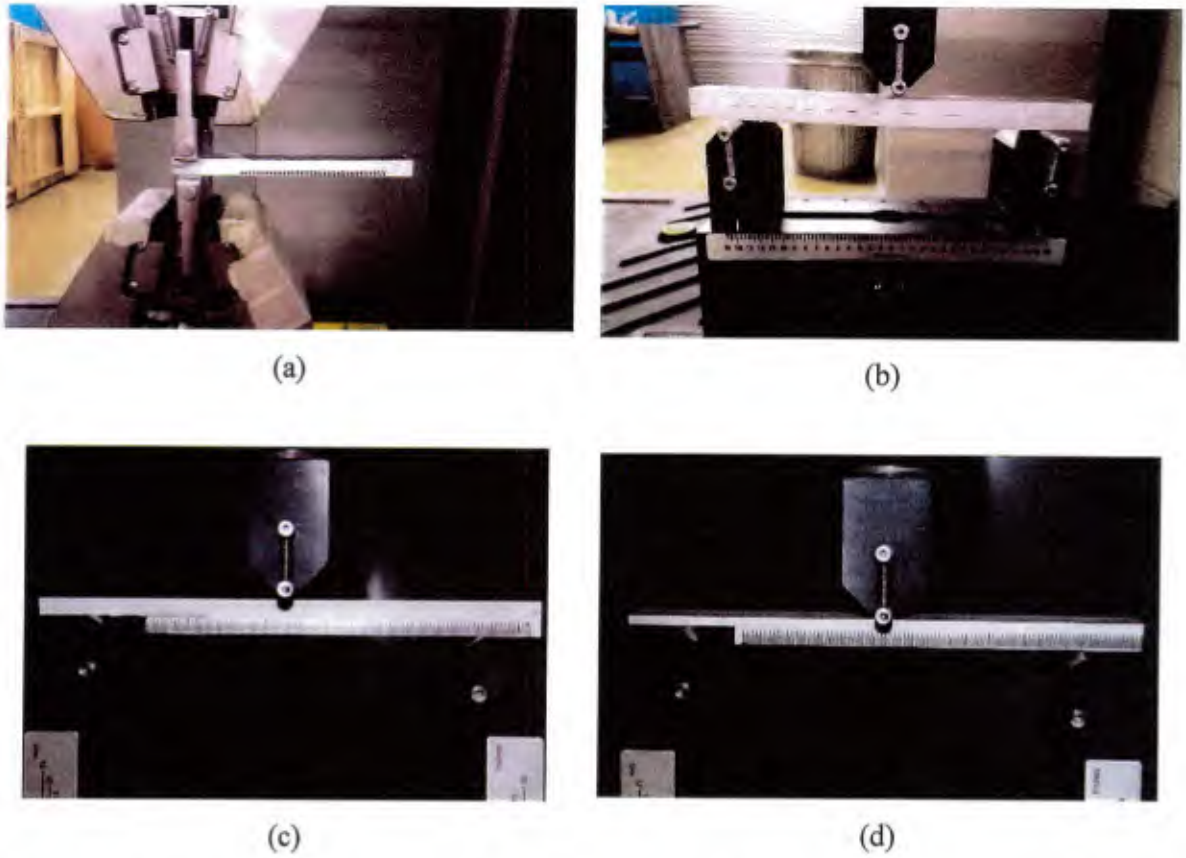

Figure 32. Experimental Test Setups for (a) DCB, (b) ENF, and (c), (d) two variations of SLB tests.

Many data reduction methods exist for calculating the fracture energy for mode I, II, and I+II. Beam theory is used as a basis for many of these methods. While reasonably accurate, they usually require precise measurements of the crack propagation during the experimental testing and do not capture the effects of the fracture process zone (FPZ) ahead of the crack tip. The effects from this FPZ have proven to be non-negligible for ductile adhesives, such as the type use in this study. An equivalent crack method, developed by [25] and called the compliance-based beam method (CBBM), uses the load and displacement data from the test to compute a specimen compliance. This compliance is used to compute a corrected flexural modulus, based on the initial crack length. The fracture energy in mode I can be computed by the following equation

$$G_{Ic}^{DCB} = \frac{6P^2}{B^2h}\left(\frac{2a_e^2}{h^2E_f} + \frac{1}{5G_{13}}\right) \tag{8}$$

where P is load, a_{eq} equivalent crack length, B specimen width, h the adherend thickness, E_f the corrected flexural modulus, and G_{13} the shear modulus of the adherends. More details on the formulation of this equation can be found in [25].

Much like mode I, the ability to measure crack propagation for the mode II ENF test is difficult. This is because, in addition to the FPZ issues, the compression of the adherends creates a scenario where the crack front becomes nearly impossible to detect. CBBM, developed by [23] using the ENF and ELS tests, has been shown to be an accurate scheme for calculating mode II fracture energy. G_{IIc} is found from the following equation

$$G_{IIc}^{ENF} = \frac{9P^2a_{eq}^2}{16B^2E_fh^3} \tag{9}$$

More information on the formulation of this equation can be found in [23].

For the SLB tests using the adherends with equal thickness, the CBBM approach is also used [26]. Again, this approach does not require the crack length monitoring. The fracture energy components are calculated as

$$G_I^{SLB} = \left(\frac{3P^2a_{eq}^2}{4B^2E_fh^3}\right)^{-1} + \frac{3P^2}{40G_{13}B^2h} \tag{10}$$

and

$$G_{II}^{SLB} = \frac{9P^2a_{eq}^2}{16E_fB^2h^3} \tag{11}$$

The total mixed-mode I+II fracture toughness is found by

$$G_T^{SLB} = G_I^{SLB} + G_{II}^{SLB} \tag{12}$$

The SLB specimens with the different thickness adherends use a different method of calculating fracture toughness. This method calculates the fracture energies based on beam theory and requires the load and crack length monitoring during the test:

$$G_I^{SLB} = \frac{P^2a^2}{8b}\left(\frac{D_2^2}{(D_1+D_2)^2}\left(\frac{1}{D_1} + \frac{1}{D_2}\right)\right) \tag{13}$$

$$G_{II}^{SLB} = \frac{P^2 a^2}{8b}\left(\frac{1}{D_1+D_2} - \frac{1}{D}\right) \tag{14}$$

where D_1, D_2, and D are the flexural rigidity of the top, bottom, and bonded beam, respectively. More information on this calculation can be found at [27].

P-δ curves of the DCB, ENF, and SLB experimental tests are presented in Figure 33, Figure 34, and Figure 35. The curves show linear behavior initially then sudden drop off when adhesive failure begins.

The DCB and SLB tests required that the specimens be precracked prior to being tested. This was completed by initially loading the specimens until a crack was formed. Once detected, the specimen loading was stopped, and the testing machine brought to zero. The location of the new a_0 was documented and the actual test started. The discrepancy in the initial slopes of these tests can be explained by the fact that the new a_0 varied from specimen to specimen and thus resulted in varying initial stiffnesses.

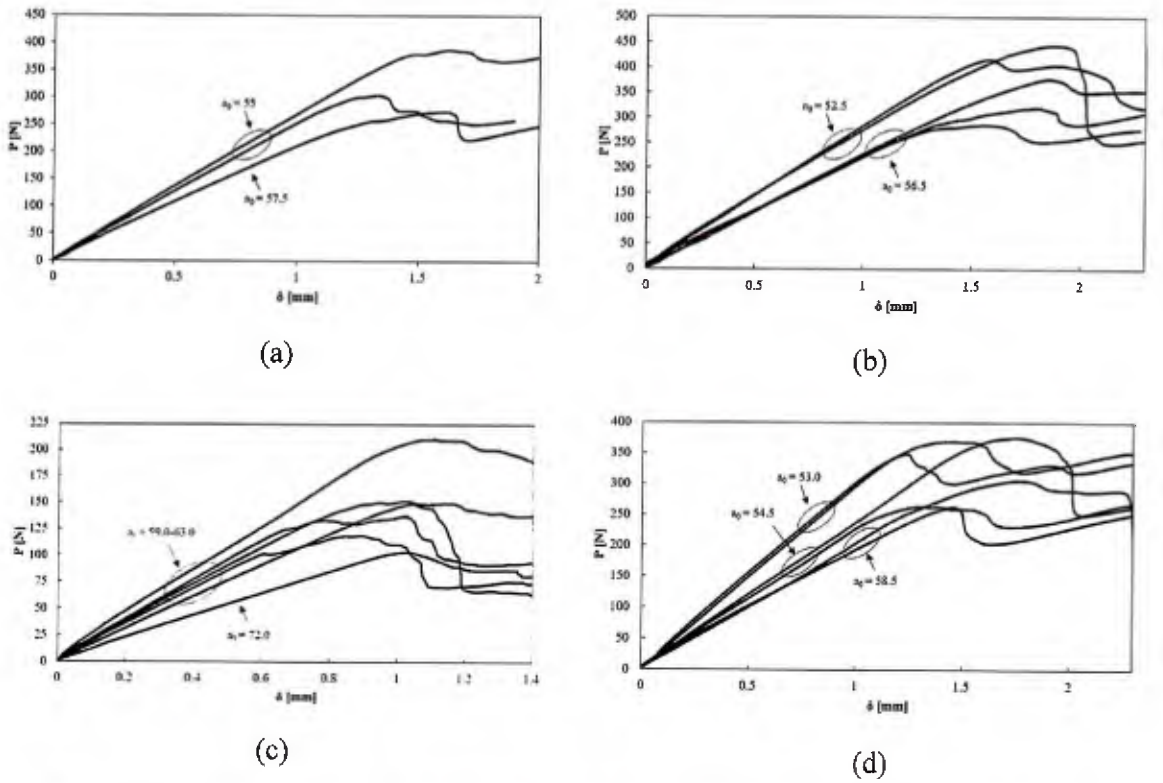

Figure 33. DCB experimental load-deflection behavior for Groups A (a) B (b) C (c) and D (d).

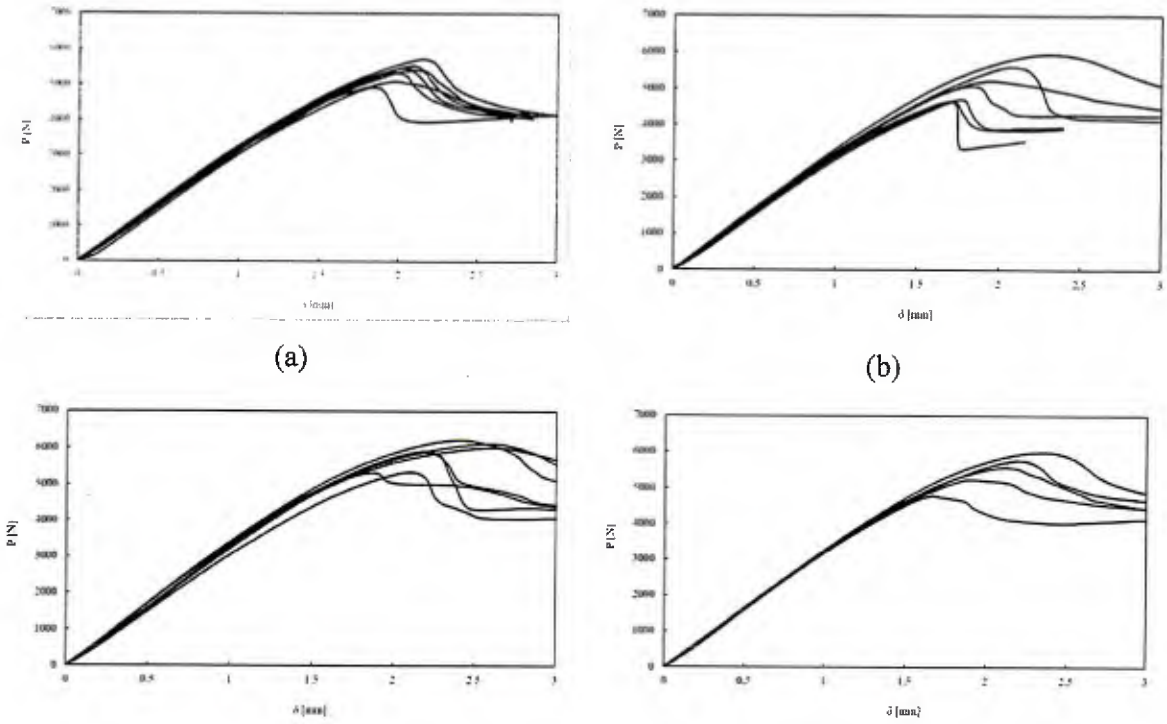

Figure 34. ENF experimental load-deflection behavior for Groups A (a) B (b) C (c) and D (d).

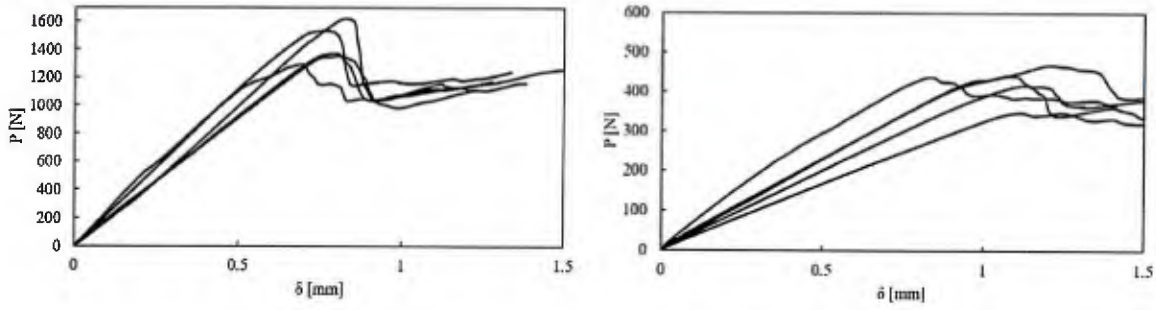

Figure 35. SLB experimental load-deflection curves for specimens with same thickness (a) and different thickness (b) adherends

Numerical models were created in the Abaqus® finite element software. Implementation of the adhesive layers of the DCB and ENF was achieved using cohesive elements, with bilinear and trapezoidal cohesive zone models used to simulate the mode I and mode II damage, respectively. Figure 36 depicts the shape of these laws, where σ_0 is the cohesive strength, 69 MPa, K_p the penalty stiffness, 16,400 N/mm^3, and the area under the curves the fracture toughness, G_c, calculated from the experimental tests. More information on the formulation can be found in [28].

The SLB adhesive layers were simulated using a potential-based cohesive zone model (PPR model). This model has been shown to accurately simulate adhesive failure under mixed-mode loadings and represents an alternative approach to using the standard cohesive element in the Abaqus® library. This PPR model was implemented as a user-defined element (UEL). More information on this PPR UEL can be found in [29].

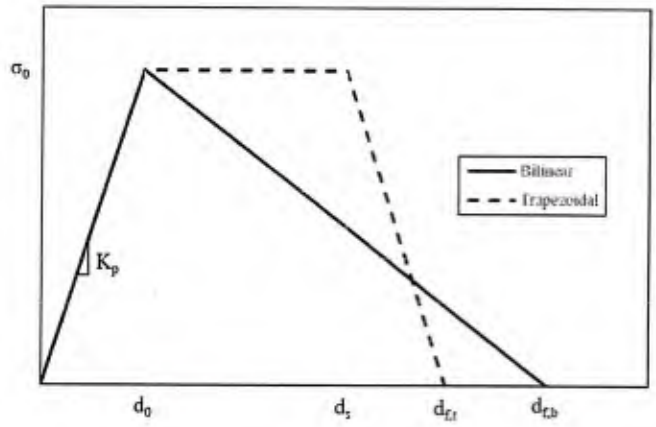

Figure 36. Traction separation laws used in FE models

The finite element models are shown in Figure 37. The DCB and ENF FE models were created with 3D 8-node, reduced integration bricks for the adherends and 8-node cohesive elements for the adhesive layer. The SLB models used 2D 8-node, reduced integration plane stress elements for the adherends and the previously discussed UEL for the adhesive layer [29]. The results of the FE models compared to the experimental data is shown in Figure 38. Overall, the numerical models show excellent agreement when compared to the experimental results.

Figure 37. FE models for the DCB (a), ENF (b) and SLB (c, d) tests

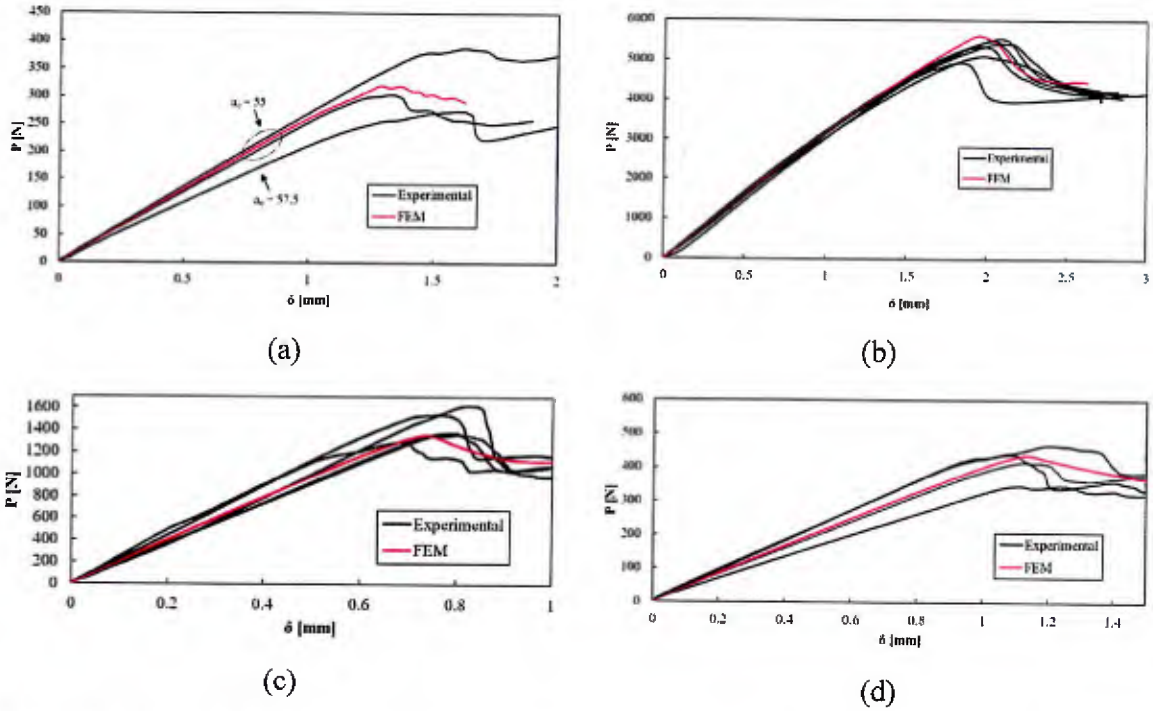

Figure 38. Comparison of experimental and FE prediction for the DCB (a), ENF (b) and SLB (c, d) tests

3.3 Three Point Bending

The primary objective of the three-point bending configuration applied to hybrid structure was to obtain data for validation of a high fidelity FE model. This FE model explicitly models the metallic substrate, the interface, and each layer of the composite, and has been developed to capture the yielding in the metal, disbond at the interface, and progressive damage in the composite. To investigate the damage mechanisms that contribute to hybrid structural failure, the model was evaluated under varying material properties once it had been validated by the experimental test data. Two different configurations were chosen to capture different combinations of damage mechanisms including the yielding of the aluminum substrate, interface disbond, delamination between the plies in the composite, fiber breakage, and matrix cracking.

The metal/composite hybrid is created by co-curing an aluminum 5456 alloy to the baseline E-glass/epoxy composite using a hand lay-up procedure and vacuum infusion. The aluminum plate is 0.25 inches thick and was bonded to a combination of laminates with an overall thickness of 0.16 inches. The bonding side of the aluminum plate was prepared using the metal surface preparation outlined in the application guide AC-®130 provided by the distributor, Advanced Chemistry & Technology. ±45° (Vectorply E-BX 1200) and 0°/90° (Vectorply E-LT 1800) stitched fabrics were used as the main fabric plies in the composite patch to create a quasi-isotropic laminate. A 0°/90° plain weave ply (Hexcel 7500) was set against the aluminum substrate. While a 0°/90° fine harness satin weave ply (Hexcel 7781) lies on the surface of the laminate to achieve a quality surface. The stacking sequence of the laminate is displayed in Figure 4. The composite matrix is an epoxy resin (M1002) mixed with a curing agent (M2046 hardener). This epoxy mixture was applied between each fabric layer of the composite patch and at the interface between the aluminum and Hexcel 7500. The composite patch was then covered by a vacuum bag with a P3 perforated film on top of the composite patch to help control the bleed rate of the resin. The vacuum level was set to 20 inHg of pressure over three hours. The patch was then cured for four hours inside an oven set at 140 °F. After the patch had been cured, the metal/composite plate was cut into specimens.

Regardless of the specimen load configuration the specimens shared the same dimensions. These dimensions are displayed in Figure 39. Figure 40 shows a completed specimen. The specimens were cut using water jet machining. A procedure was created to avoid damage occurring in the composite layers during the cutting process. The damage mechanism observed during the water jet cutting was delamination between the outer plies and is demonstrated in Figure 41. To reduce the loss of valid specimens a cutting process was developed to mitigate the damage occurring to the composite layers during the cut. The cutting path is displayed in Figure 42. This cut required two continuous paths to avoid delamination occurring past the first several specimens. The first cut began with a one inch lead-in that reduced the delamination damage caused by the initial water penetration. The second cut was a continuous straight line. The specimens past the first few showed no delamination between the plies by visual inspection. Due to the cutting technique and limitations of the water jet machine, a small strip of material was left on the side of the specimens that connected them together. This excess material was trimmed to separate each specimen from the others. No damage was observed during the trimming. The plate in Figure 41 shows how the specimens were cut from a larger plate.

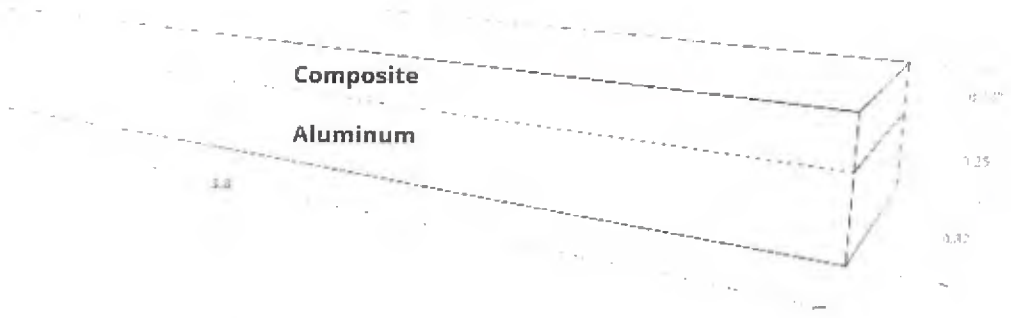

Figure 39. Dimensions of the specimens

Figure 40. Test specimen fabricated with aluminum and E-glass/epoxy

Figure 41. Metal/composite hybrid plate with specimens cut out. Delamination is shown near the initial lead-in (top). The first several specimens were invalid.

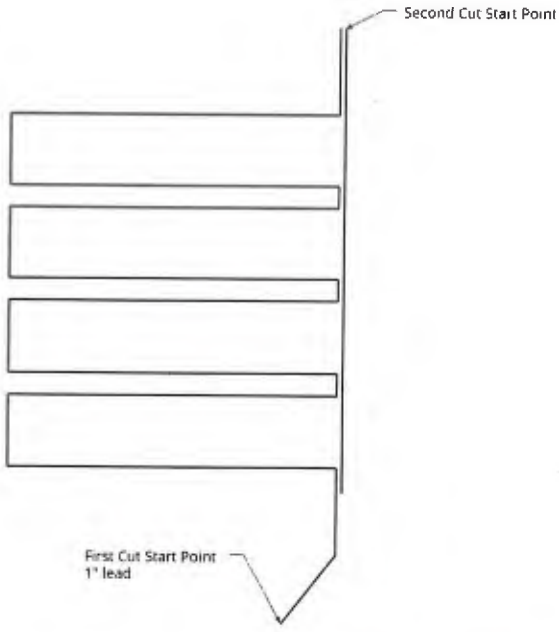

Figure 42. Cut schematic developed to mitigate delamination occurring during the specimen cutting process.

The boundary conditions were varied by inserting the composite on the tension or compression side of the fixture to capture the varying damage behaviors. The three-point bend testing was performed using an MTS testing machine that collected the loading force and displacement of the loading pin. The loading rate of the machine was set to 0.05 inch/min after review of several ASTM standards for metal and composite testing. The specimens were speckled on one side to enable a digital image correlation (DIC) system to calculate the real-time strain field during loading. DIC creates the strain field by comparing the movement of thousands of individual speckle points with one another from image to image. DIC imaging enables the creation of strain contours during the test providing critical validation data, particularly for this problem that included multiple damage mechanics and complex behavior. This strain field provided a way to compare the FE model to the experimental method in addition to the load-displacement relation. For this information to be accurate both the MTS machine and the DIC system were required to be started at the same time and operated with the same frequency of data collection.

The different loading conditions demonstrated multiple damage mechanisms in different degrees. The damage and permanent deformation in the specimens post-testing are shown in Figure 43. The DIC system's cameras recorded the speckled side of the specimen, and corresponding software was used to calculate the strain field on that surface. Figure 44 and Figure 45 illustrate the damage progression over time including the strain fields of the intact specimens, damage initiation, damage evolution, and complete failure.

Figure 43. Specimens post-testing. Back side of the specimens are shown to help distinguish between the composite and aluminum layers. Damage is highlighted with red circles and lines to illustrate where the damage occurs. (Left) Composite in tension, specimen-format A. (Right) Composite in compression, specimen-format B.

Damage in specimen-format A had the aluminum closest to the loading pin and placed the composite in tension. The failure occurred from intralaminar damage and interlaminar delamination. The composite layers on the outside of the hybrid specimen failed first. This can be seen in Figure 44. The damage was due to the maximum tensile stress occurring in that region. The fiber fracture and delamination of the other layers followed.

Specimen-format B had the top of the composite closest to the loading pin and placed the composite layers in compression. This format allowed the specimen to fail at the location of maximum shear force and moment. The failure initiated close to the loading pin. An expected failure would have been directly under the loading pin. However, defects inside the composite layers affected where the damage initiated. These defects consist of air voids, inclusions, and the inherent variation in mechanical properties. The damage initiated at the sites that had more defects or weaker mechanical properties. This damage then propagated to failure. The initial damage was fabric fracture and matrix cracking. This damage then propagated until failure occurred due to disbond. The damage evolution is provided in Figure 45.

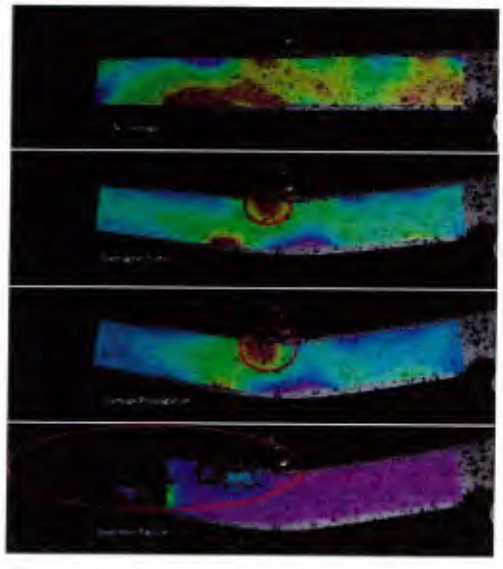

Figure 44. Damage propagation in three-point bending specimen-format A, and the strain field of the speckled face.

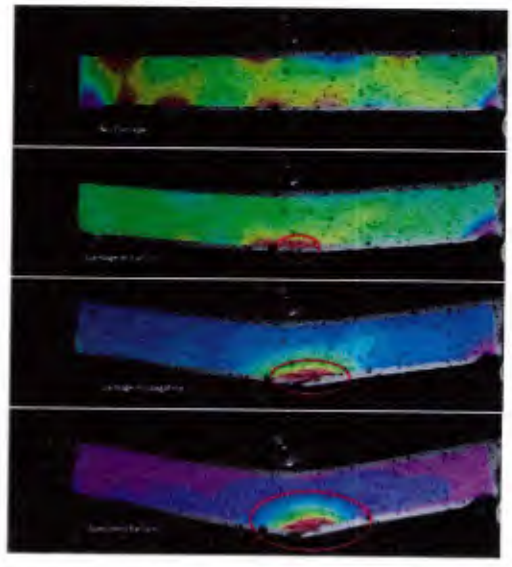

Figure 45. Damage propagation in three-point bending specimen-format B, and the strain field of the speckled face.

3.4 Four Point Bending

Experimental testing was also performed on four-point bending specimens to investigate progressive damage propagation under different loading conditions. The objective was to collect experimental data to validate the high-fidelity FE model under different combinations of damage mechanisms. This FE model explicitly modeled the metallic substrate, the interface, and each layer of the composite, and has been developed to capture the yielding in the metal, disbond at the interface, and progressive damage in the composite. Four different specimen configurations were designed to investigate varying combinations of the damage modes. These damage mechanisms were the same ones demonstrated by the three-point bending and included the yielding of the aluminum substrate, interface disbond, delamination between the plies in the composite, fiber breakage, and matrix cracking. The four different specimen configurations are shown in Figure 46.

The test setup and fabrication of these specimens were the same as the three-point bending specimens. To avoid damage to the composite patch during the cutting process, a water jet machine was used to cut the specimens from the large patched panel. The notches of specimen-C and D were machined with a CNC machine. The MTS machine was set to the same loading rate of 0.05 inch/min. The specimens were speckled on one side only to allow the use of a DIC system to calculate the strain field while loading the specimens. The DIC system generated the strain contours during the test and provided critical validation of the FE model. Having both the strain field and the load-displacement relation to validate the FE model was crucial for this problem. This is due to the multiple damage mechanics and complex behavior of the composite patch. The MTS machine and the DIC system collected data at the same frequency and had to be started at the same time to correctly correlate the data.

The four different specimen configurations allowed the experimental collection of data on the damage modes, including fiber fracture, matrix cracking, delamination between the plies, interface disbond, and yielding of the aluminum. Specimens A and B evaluate the composite patch under tension and compression respectively. Specimens C and D with an initial notch in the aluminum substrate or the composite patch respectively, are designed to study the disbond at the interface between the composite patch and the aluminum plate. The test configurations were designed using third point loading where the span of the loading pins on the top of the specimen is one-third of that of support pins at the bottom. The diameter of both the loading and support pins are 0.2 inch. All specimens are 3.9 inch long, 0.65 inch wide, and 0.41 inch thick.

Damage in specimen A initiated at the site where the maximum shear force and moment occurred and took the form of delamination. Due to the symmetry of the geometry, the theoretical damage should initiate under the loading pins simultaneously. However, akin to the three-point bending specimens, defects inside the specimens including air voids, inclusions, and mechanical properties initiated damage at the weakest locations. The damage initiated and propagated to failure from the site(s) that had more defects or weaker mechanical properties. The failure in the specimen shown in Figure 48 occurred from delamination on the left side. Since this failure occurred in the composite patch instead of at the interface between the aluminum and the composite, it can be concluded that interface strength was higher than the interlaminar strength. Additional damage is observed in fabric fracture and matrix cracking caused by the compressive stress in the top layers of the composite. This damage can be seen in Figure 47.

Specimen B displayed delamination and intralaminar damage as shown in Figure 47. The outside layer of the composite failed first, and the damage took the form of fiber fracture and delamination. This damage occurred in the presence of the maximum tension stress. As shown in Figure 48b, the delamination and fracture of the subsequent layers followed.

In specimen C, delamination of the same layer as in specimen A was observed. Specimen C also displayed the same damage in the top layer of the patch similar to specimen-A. The comparison of specimen C in Figure 47 and Figure 48c shows that minimal plastic deformation occurred in the aluminum substrate. It can be deduced that the main load-carrying component was the composite patch, which displays a more brittle behavior.

The interface disbond between the aluminum substrate and the composite patch dominated the failure in specimen D. This is prominently displayed in Figure 48d. Unlike specimen C, specimen D was able to produce a higher disbond stress. This occurred due to the aluminum being unnotched, which is significantly tougher than the composite.

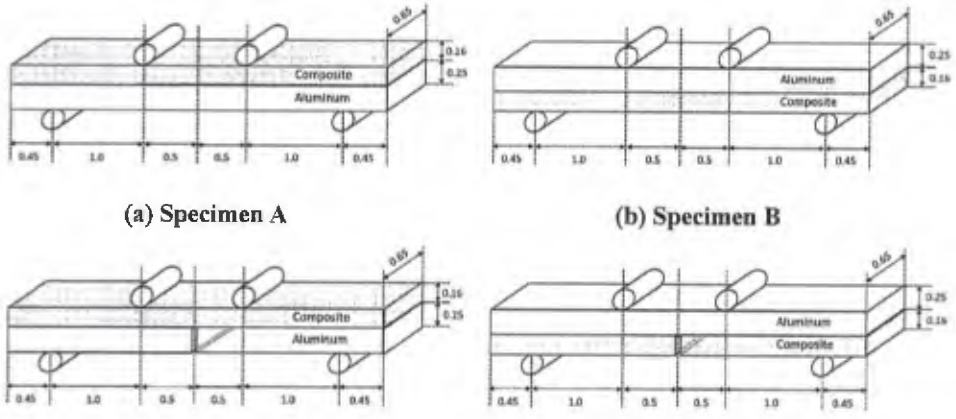

(a) Specimen A (b) Specimen B

(c) Specimen C (d) Specimen D

Figure 46. Four different specimen configurations of the four-point bending test, all dimensions are in inches.

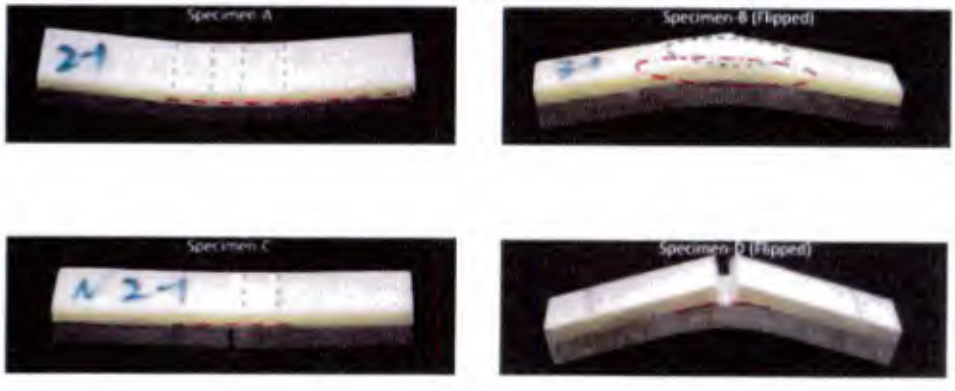

Figure 47. Specimens post-testing. Back side of the specimens are shown to help distinguish between the composite and aluminum layers. Red dash marks indicate delamination. Blue dash marks indicate intralaminar damage.

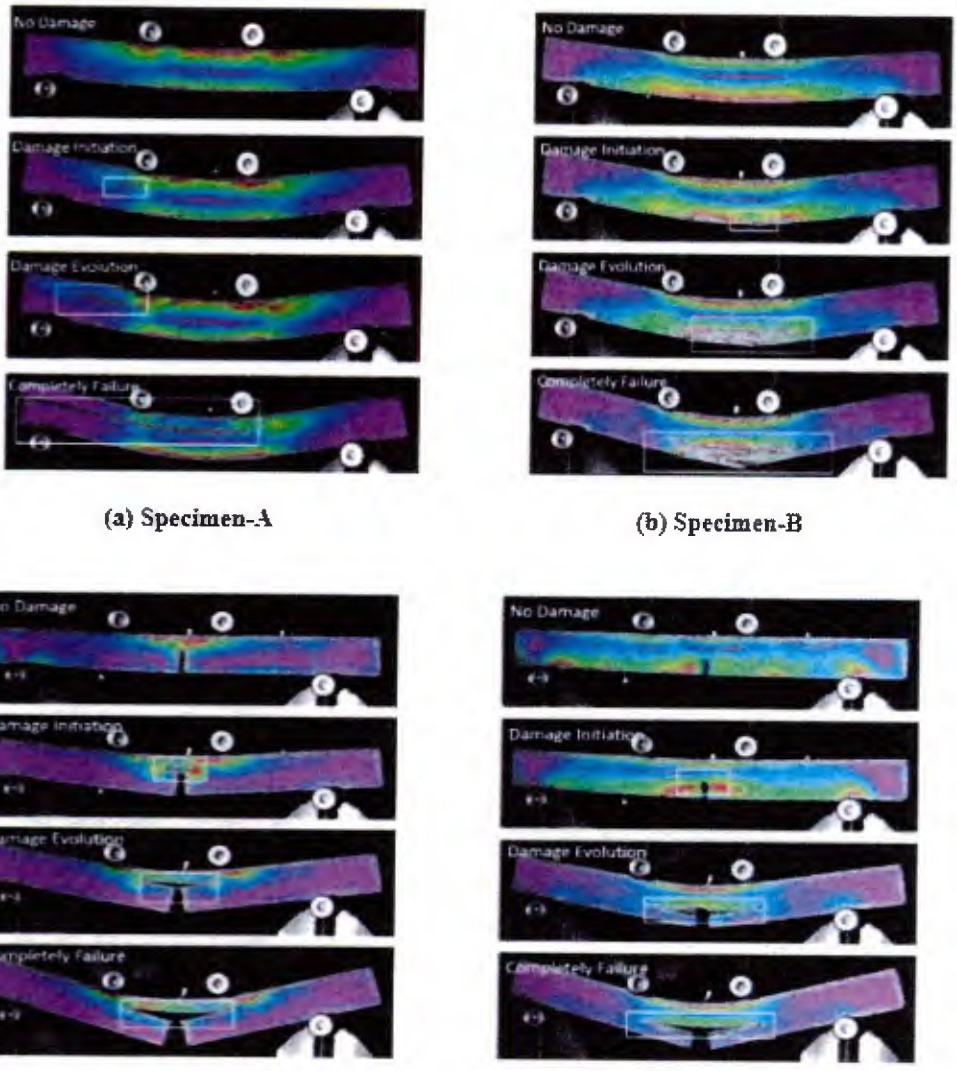

(a) Specimen-A

(b) Specimen-B

(c) Specimen-C

(d) Specimen-D

Figure 48. DIC results for undamaged patched structure under four point bend loading showing different failure mechanisms based on test configuration. The white box indicates an interface failure.

3.5 Mixed Mode Crack Growth in Hybrid Structure

The high strength aluminum alloys often used in marine structures suffer from cracking during service life. Installation of a composite patch has been demonstrated as a promising repair method to restore the damage tolerance of these cracked marine structures. Previous research [30-41] studied crack behavior in aluminum repaired with a composite patch. However, most of the investigations only considered pure Mode I fracture. In addition to the likelihood of mixed loading conditions during service life, mixed mode crack growth can be also initiated with tensile far-field stresses. Prior research [42, 43] shows that crack growth in aluminum alloys with high ductility exhibit a deviation (and corresponding change in growth direction) from pure Mode I due to the effects of multiaxial stresses, high loads, microstructure, and environmental effects.

The objective of this testing is to investigate and gather validation data for mixed mode crack growth and to evaluate the effectiveness of the composite patch in restoring damage tolerance of Al 5456 plate. Both unrepaired single edge crack specimens (Figure 49) and composite patch repaired single edge crack specimens (Figure 50) were tested under tensile loading.

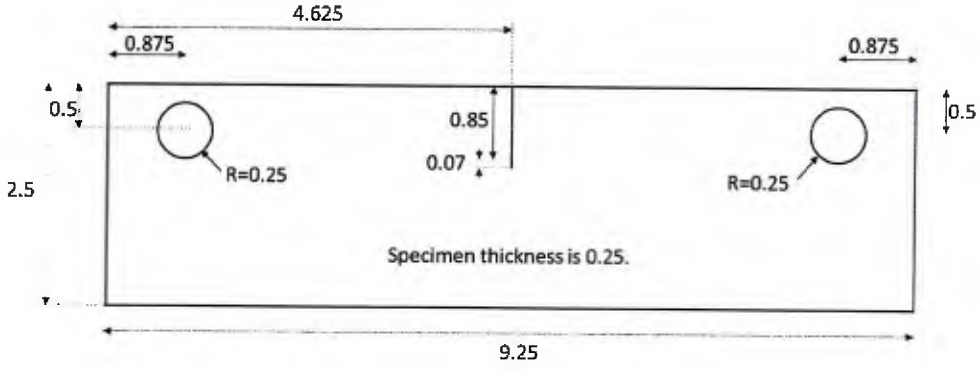

Figure 49. Configuration of the single edge specimen (inches).

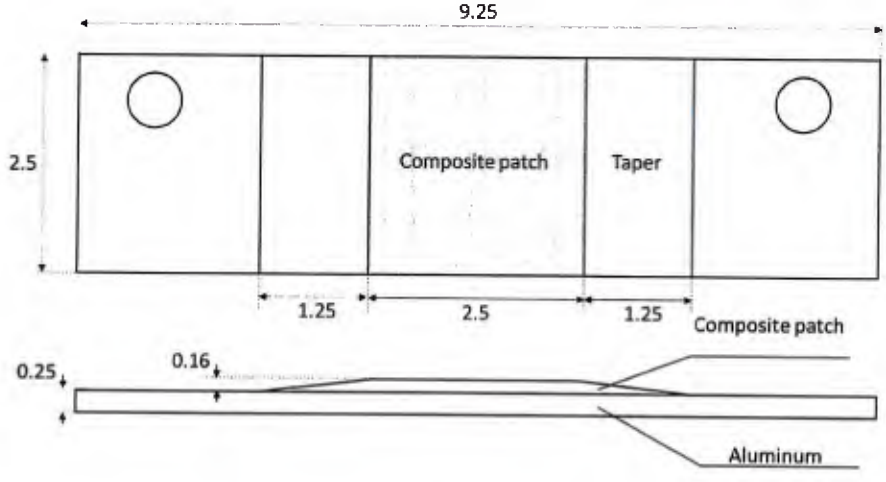

Figure 50. Configuration of the single edge specimen repaired with the composite patch (inches).

Aluminum alloy 5456 plate (from McMaster-Carr) was used to fabricate single edge crack specimens with a thickness of 0.25 inch. The elastic-plastic properties of the alloy were obtained from tensile testing data provided by the US Navy and are summarized in Table 9, where the plastic behavior is described by the Ludwik-Hollomon hardening law as shown in Eq. 15,

$$\bar{\sigma} = A + C\bar{\varepsilon}^n \tag{15}$$

$\bar{\sigma}$ is the equivalent plastic stress, $\bar{\varepsilon}$ is the equivalent plastic strain, A, C, n are material properties obtained via empirical fitting to the stress-strain curve of the experimental data. Strain rate and temperature effects have been neglected, because both the tensile testing and fracture testing are quasi static processes with negligible temperature variation.

Table 9. Elastic and plastic properties of Al5456 (provided by the United States Naval Academy)

E (Psi)	σ_Y (Psi)	v	A	C	n
1.0 E+07	2.2 E+04	0.3	2.2 E+04	7.2 E+04	0.34

The composite patch was fabricated according to the baseline layup described in section 1.2. The epoxy resin (M1002) and the hardener (M2046) were mixed to form the composite patch matrix and the bondline, and both were purchased from PRO-SET. The patch was reinforced by eglass fabric obtained from commercial sources, including the 8.8 oz/yd^2 Hexcel 7781 style 8 harness satin weave fabric, the 12 oz/yd^2 biaxial stitch bonded ±45° fabric, the 18 oz/yd^2 biaxial stitch bonded 0°/90° fabric and the 9.6 oz/yd^2 Hexel 7500 style plain weave fabric.

Specimens were fabricated with the initial edge notch perpendicular to the longitudinal direction on the aluminum plate. The initial notch of 0.06-inch width and 0.85-inch length was cut in the middle of the specimen edge by electrical discharge machining. Then a sharp fatigue pre-crack tip was generated by cyclic loading in a fatigue test machine. The maximum load was set as 400 lbf with a 10:1 tension-tension load amplitude ratio in the fatigue machine. The expected fatigue pre-crack was acquired running the cyclic loading for 2 hours with a load frequency of 5 Hz.

Unlike the co-cure process where the composite patch and bond line are fabricated simultaneously with hand layup and vacuum bagging directly onto the Al plate followed by machining to obtain the specimen of the desired geometry, the preparation of the patch-repaired cracked specimens was divided into two steps for ease of specimen fabrication. The composite laminate was first fabricated and then co-cured to the aluminum plate specimen using the epoxy. In the first step, a quasi-isotropic E-glass/epoxy composite laminate (2.0 ft x 2.0 ft) was prepared by the vacuum-bagging method. Four different types of fabrics are stacked on a glass panel in the sequence given in section 1.2. The 0°/90° fine harness stain weave ply Hexcel 7781 is used as the top ply to obtain a quality surface, and a layer of peel ply was placed after the bottom layer of the patch in order to achieve the same bond line mechanical properties between the patch and the aluminum plate as those prepared in the co-cure process. The epoxy resin (M1002) and the curing agent (M2046 hardener) were mixed in the ratio 4:1 by volume and spread onto the fabrics layer by layer during the hand layup process. The composite laminate was placed in the vacuum bag overnight under 23 inHg and then cured in the oven at 140° F for 4 hours. The setup of the vacuum bagging is

illustrated in Figure 51. The total thickness of the patch is 0.16 inch and the mechanical properties of the composite patch are given in Table 10. Prior to bonding to the aluminum plate, the composite patch was cut by a water jet machine into small rectangular pieces (2.5 inch x 5 inch). Then the taper at both sides was machined to avoid large peeling stresses in the specimen.

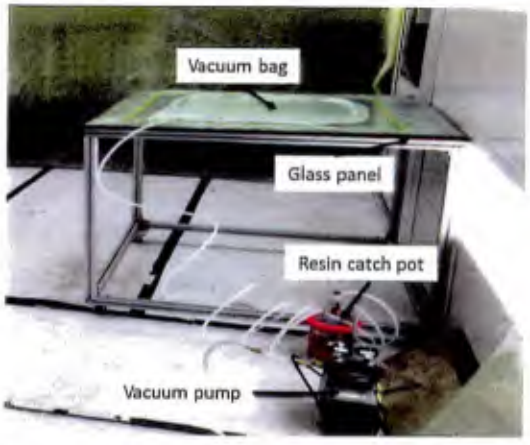

Figure 51. The vacuum bagging system to fabricate the composite patch.

Table 10. Mechanical properties of the E-glass/epoxy composite patch

E_{11}	1.7E+06	G_{12}	6.3E+05	ν_{12}	0.27
E_{22}	1.7E+06	G_{13}	2.8E+05	ν_{13}	0.25
E_{33}	7.7E+05	G_{23}	2.8E+05	ν_{23}	0.25

Before bonding the patch and the metal, the metal surface on the bonding side of the specimens was degreased with acetone, deoxidized with 180 grit sandpaper, and sprayed by the AC-130 solution. The epoxy (M1002) and hardener (M2046) again with the same mixing ratio (4:1 by volume) were used to bond the patch and aluminum. The resin was mixed with glass beads with a 0.004-inch diameter to control the thickness of the bond line. 2 grams of the glass beads are used with every 3 oz. of mixed resin. The bonded specimens were covered with vacuum bag under 23 inHg in a 140° F oven for 4 hours to eliminate the extra resin at the bond line and to cure the resin.

The fracture testing was performed on an MTS testing machine following the ASTM E1820 procedure, with the experimental setup shown in Figure 52Figure 53. The testing was performed with displacement control under the loading rate of 0.04 inch per minute. The crack extension on the outside of the specimen was monitored by a high-resolution camera (Canon, EOS Rebel T5i with 18-55 mm lens), with the video recorded at 1920 X 1280 pixels.

Figure 52. The experimental apparatus for showing a test of an unrepaired Al specimen.

Figure 53. The experimental apparatus for showing a test of a repaired Al specimen.

The fatigue pre-cracks in the unrepaired specimens were relatively straight and perpendicular to the loading direction (Figure 54a). However, the material deformation results in shear strain in the plastic zone around the crack tip (Figure 54b), leading to the presence of shear band localization and the subsequent initiation of inclined crack (Figure 54c). The mixed Mode I and II crack continue to propagate as a straight line along the direction of the initial inclined crack (Figure 54d). The crack angle, defined as the angle between the crack line on the outside surface of the specimen and the fatigue pre-crack line, was consistently about 135° (Figure 55) throughout the cracking process for all unrepaired specimens.

Figure 56 shows the fracture surface of the crack in the unrepaired specimen. The pre-fatigue crack with a smooth fracture surface is followed by a flat to slant crack transition region. The flat crack surface was formed because of the high stress triaxiality in the interior of the specimen, and the slant of the fracture surface was initiated because of the low stress triaxiality near the free surface. Then the crack propagated as a double slant crack all the way until the specimen fully failed.

The crack behavior in the repaired specimen is shown in Figure 57. A sudden disbond with a large area at the bondline was observed during the test and no damage was found in the composite patch. No crack initiation was detected right before the disbond as depicted in Figure 57a. Only a small plastic zone appeared around the tip of the pre-fatigue crack. The sudden disbond of the bond line caused the detachment of half of the composite patch from the aluminum. Unlike the unrepaired specimen, the crack in the repaired specimen initiated immediately with a large crack opening, as shown in Figure 59b, instead of initiating and propagating gradually. The crack then propagated with the same crack angle as the unrepaired specimen given that the patch was no longer effective, as illustrated in Figure 57d. Some resin remained on the aluminum surface after disbond, as shown in Figure 59.

Figure 60 compares the load-displacement curve of the repaired specimen with that of the unrepaired specimen. The composite patch changes the maximum load of the specimen from 4900 lbf to 6300 lbf, with a 29% increase. The sudden drop of the load after the first peak load in the repaired specimen is caused by the large disbond of the bond line. Then the curve follows the same trend as that of the unrepaired specimen, which indicates the remaining patch bonded to the aluminum has an ignorable effect on the crack behavior of the specimen.

In addition to providing validation data for the computational models that predict crack growth in hybrid structure, this testing effort also informed the fidelity level required for the modeling effort. Given that no damage was observed in the patch itself and that the patch failure model was purely due to disbond at the interface, models were created using smeared properties for the patch instead of the high fidelity composite model which captures progressive damage in the patch, saving considerable computation time. This testing effort also highlights the importance of non-visible damage. A small and undetectable disbond at the interface can lead to complete and sudden failure of the hybrid structure.

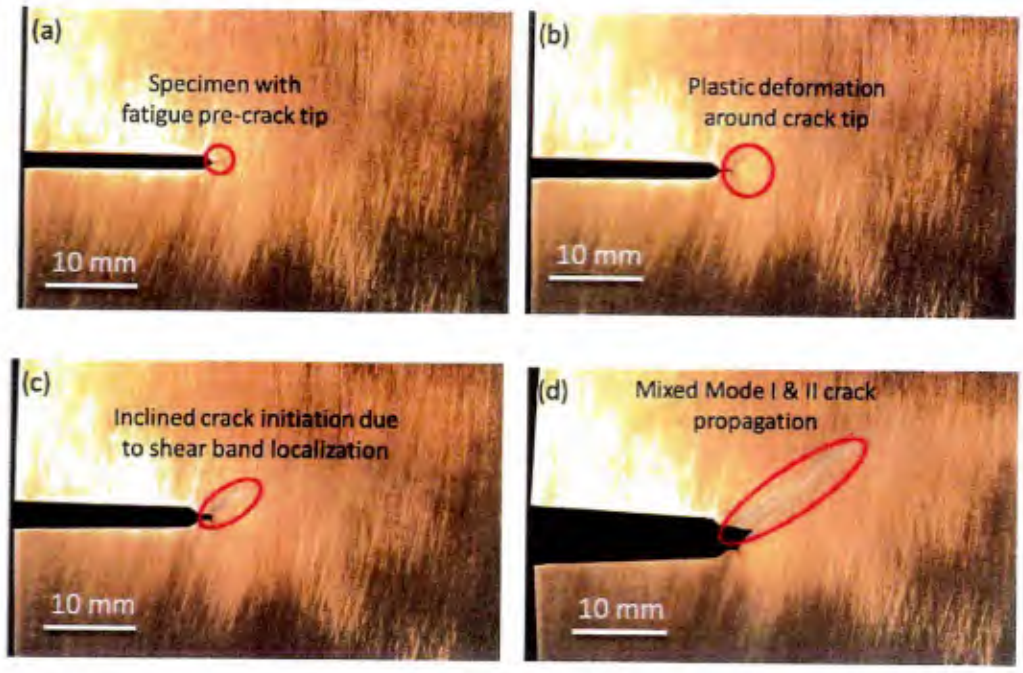

Figure 54. Crack initiation and propagation of the single edge crack specimen of unrepaired Al plate.

Figure 55. The definition of the crack angle.

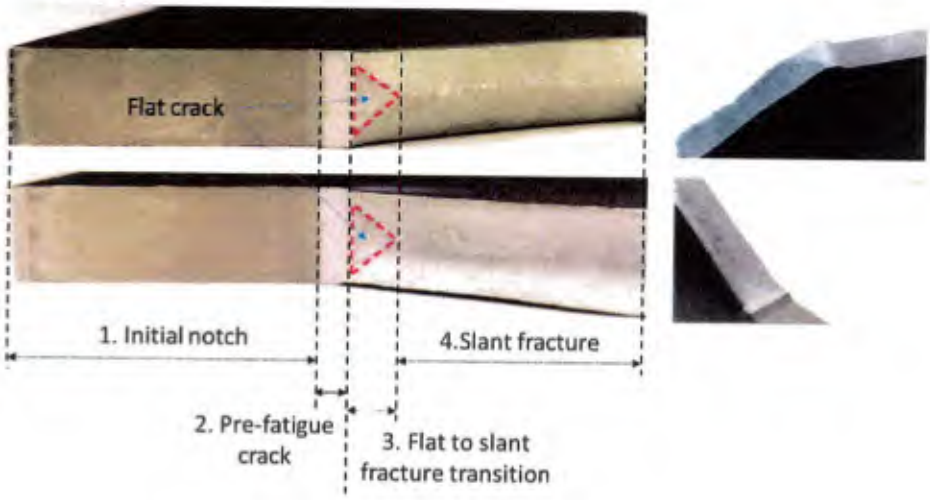

Figure 56. Fracture surface of the unrepaired specimen.

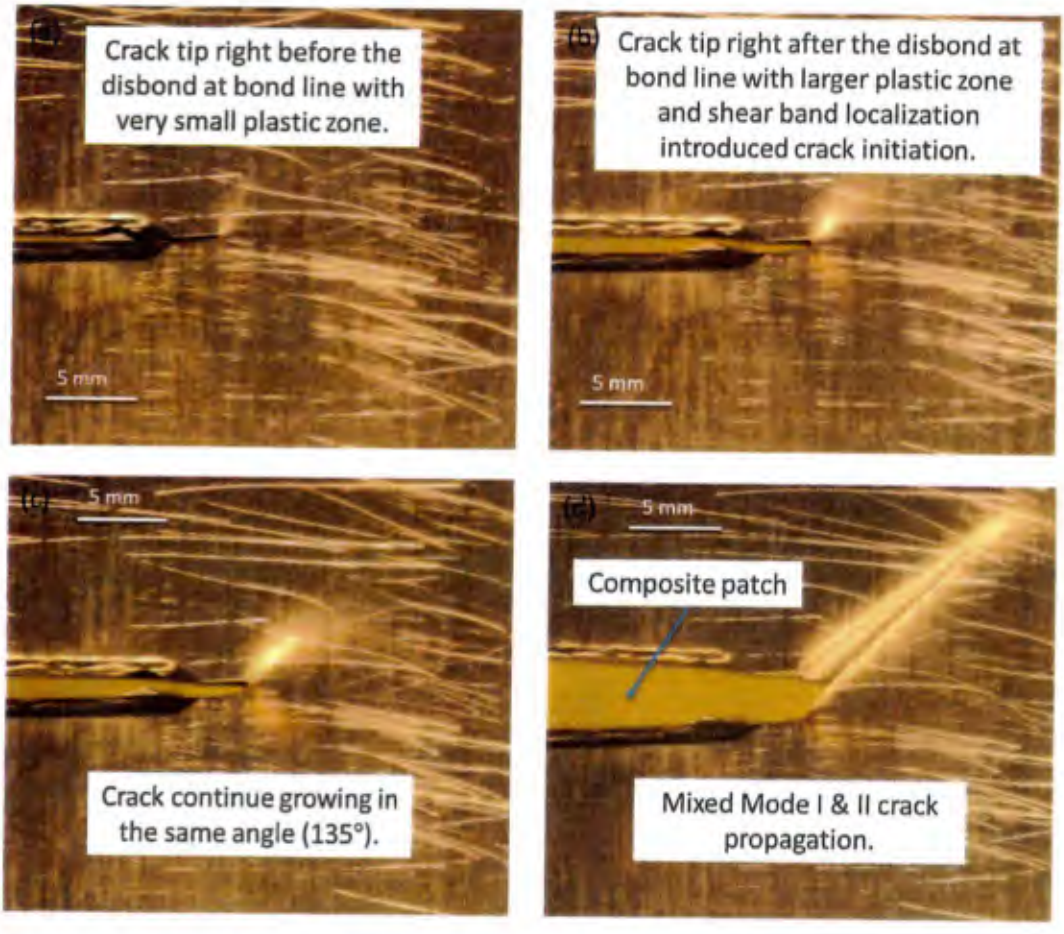

Figure 57. Crack initiation and growth in composite patch repaired specimen.

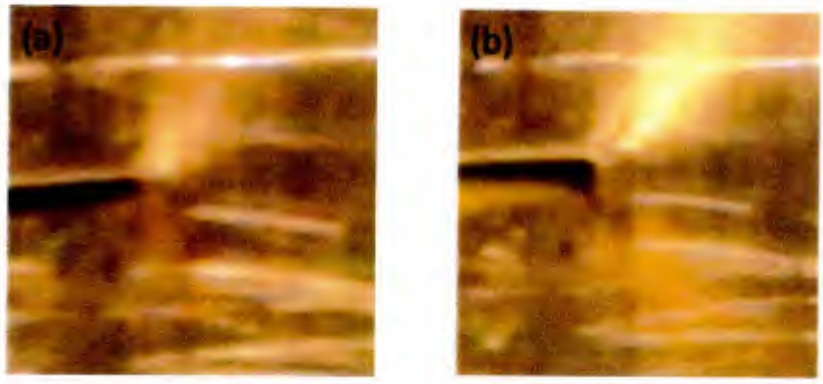

Figure 58. The crack tips in repaired specimen right before (a) and after (b) the disbond at the bond line.

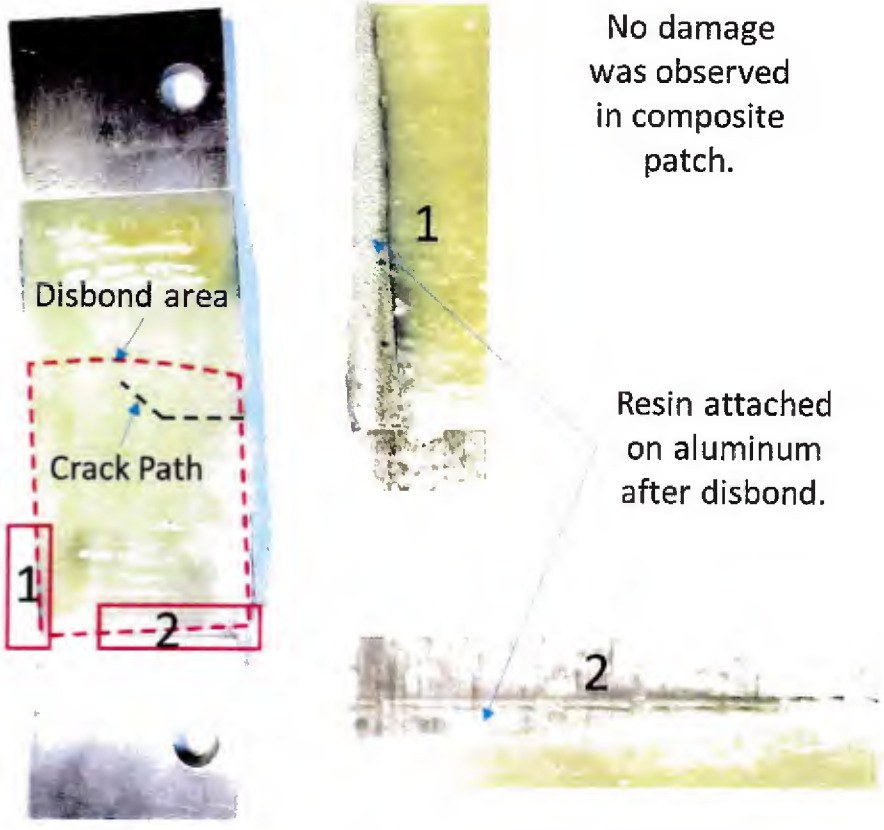

Figure 59. The schematic diagram of the disbond area and the crack path.

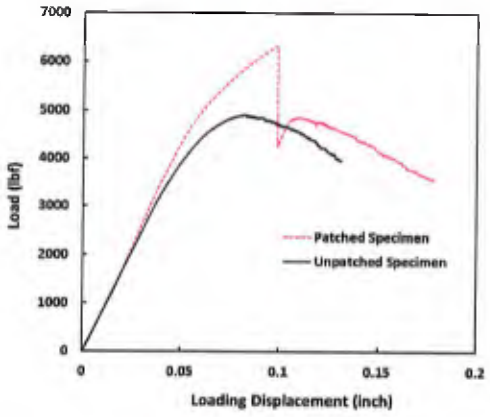

Figure 60. Comparison of the load-displacement curves of patched and unpatched specimens.

4 Multi-Scale Models and Methodology

Performing physical experiments to carry out a comprehensive study that includes all variations of all design parameters and potential configurations is prohibitive due to time constraints and cost. Numerical modeling offers an alternative method to efficiently explore designs and investigate the effects of parameters on patch performance after validating a baseline model through experimental testing.

As depicted in Figure 7, many types of damage mechanisms affect the damage tolerance of hybrid structure, and there is no single method capable of accurately simulating all mechanisms simultaneously with the required fidelity level and within a feasible amount of computation time. Therefore, multi-scale modeling with varying levels of fidelity at each scale is required to develop the capability to comprehensively investigate the damage tolerance of hybrid structure. Development of the models and methodology described in this section constituted the primary research effort of this project and provide a plug and play approach to investigate the damage tolerance of hybrid structure for varying loading conditions, composite patch configuration and materials, levels of aluminum sensitization, and crack patterns.

While composite patches offer many advantages, the experimental testing effort clearly identified that a primary concern when evaluating the damage tolerance of bonded composite patches is non-visible damage. Non-visible damage, located internally and often not identifiable without destructive inspection, can occur when the patch is subjected to general design loads or overloads during service, particularly bending stress [44-46] and low-velocity impact [47]. This non-visible damage can be present as disbond at the interface between the patch and the metal substrate, delamination within the patch, fiber fracture or local buckling, and matrix cracking. Such damage might initially be minor but then propagate under additional loading and degrade patch performance, resulting in a sudden failure (as shown in Figure 60). There is a considerable amount of prior research on the damage analysis of composite patches that focus on topics such as the fracture behavior of bonded metallic substrates [48-52] and disbond of adhesives [53-55].

Although progressive damage in composites has been widely investigated [56-62], few studies take into account the progressive failure of the entire hybrid structure (composite, bondline, and

metal), a necessary consideration when evaluating the structural performance of the patched structure. It has been demonstrated that the damage within the composite patch can substantially reduce the efficiency of the reinforcement or repair [63, 64]. Jones [63] also indicated that multiple failure modes, including cracking in the adhesive or at the adhesive-metal interface, fiber fracture, and delamination, should be evaluated when performing damage tolerance assessment.

Therefore, it is necessary to consider multiple damage mechanisms, including the progressive failure of the composite patch and the interactions between the damage mechanisms when predicting damage initiation and propagation in the patched structure. To further complicate the investigation of damage tolerance in patched structure, varying boundary conditions and loading types are applied, each activating different combinations of damage mechanisms and in varying degrees. To accurately predict the performance of composite patches for safe implementation, it is necessary to understand the dependence of damage mechanisms relative to in-situ conditions, capture progressive damage propagation, and identify the design parameters with the most influence on damage tolerance for each service loading requirement. The developed multi-scale models and methodology provide the capability to comprehensively explore the damage tolerance of hybrid structure under many varying scenarios.

4.1 Types of Damage Mechanisms

As described below, many types of distinct damage mechanisms (which need to be modeled with disparate chemistry and physics based formulations) are required to accurately capture the effects of each on hybrid structure performance, necessitating the development of multi-scale models of varying fidelity levels. These models must support plug and play analysis that utilizes multiple models to investigate a single scenario.

Metal Damage

The damage mechanisms investigated for the metal plate component of the hybrid structure are plastic deformation, degradation due to sensitization, and crack growth in unsensitized and sensitized aluminum. Plastic deformation modeling is straight forward, and elastic-plastic material properties from experimental testing are used in all models. Additionally, crack growth in unsensitized aluminum was readily modeled using XFEM in Abaqus (see section 2.4.2 for an example). Modeling material degradation effects due to sensitization and stress corrosion cracking (SCC) constituted the primary effort for modeling metal damage.

5xxx series Al alloys are used for marine-based structures due to their high strength-to-weight ratio, weldability, and cold workability [65]. However, there are a number of service issues observed in these alloys, such as sensitization and SCC [66, 67] due to their Mg content (Table 11). When 5XXX series Al alloys are exposed to temperatures over 50°C for sufficiently long periods of time, the formation of β-phase precipitate (Al_3Mg_2) occurs along the grain boundaries (Figure 61). This process, called sensitization [68-71] can render the microstructure susceptible to intergranular stress corrosion cracking (IGSCC) if the material is subjected to a corrosive environment while under loading [67, 72, 73]. Since the β-phase is strongly anodic relative to the Al-Mg matrix, it corrodes selectively (localised corrosion in the form of pitting) at rapid rate and it modifies the local stress and ultimately shortens the fatigue life and lowers the threshold stress for crack initiation and propagation. Furthermore, the beta phase precipitation causes sensitized materials to fail in service in the presence of an acting stress of sufficient intensity.

Table 11. Composition (% weight) of Several 5XXX Aluminum Alloys

	Mg	Fe	Mn	Si	Ti	Zn	Cr	Cu
5083	4.0-4.9	0.4	0.4-1.0	0.4	0.15	0.25	0.05-0.25	0.1
5086	3.5-4.5	0.5	0.2-0.7	0.4	0.15	0.25	0.05-0.25	0.1
5456	4.7-5.5	0.4	0.5-0.1	0.25	0.2	0.25	0.05-0.20	0.1

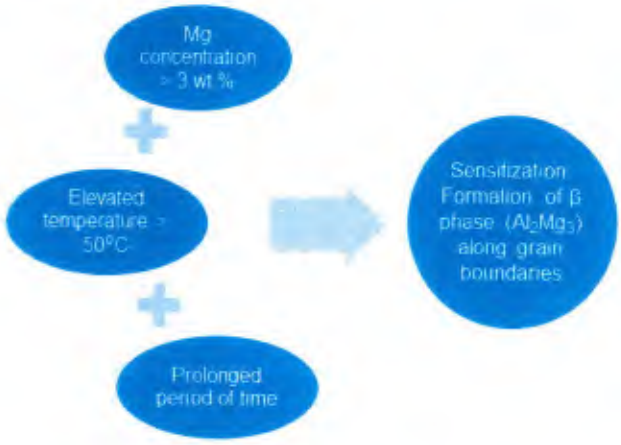

Figure 61. Sensitization process in Al alloys.

Many studies have contributed to understanding the mechanism of IGSCC in sensitized Al alloys, and one generally accepted mechanism is the selective dissolution of the β-phase [74-76]. According to this mechanism, the electrochemically active β-phase precipitation is preferentially dissolved in a salt water environment producing localized fissures and stress concentration points along grain boundaries leading to crack propagation under tensile stress and the subsequent dissolution at the new crack tips. While there is agreement that selective dissolution of β-phase affects IGSCC, recent experimental observations have suggested that hydrogen embrittlement also plays a role in the cracking mechanism during IGSCC, because observed crack growth rates are much higher than those that the pure dissolution of β-phase only could support [77]. Though the detailed role of hydrogen embrittlement in IGSCC process awaits further characterization, hydrogen enhanced decohesion (HED) has been suggested to be potentially relevant to IGSCC in sensitized Al alloys, where the dissolution of β-phase is believed to produce a sufficient amount of hydrogen that diffuses to the fracture process zone and adsorbs onto metal surface near grain boundaries, weakening the intrinsic bonding strength of grain boundaries [78].

IGSCC poses a major maintenance challenge for the US Department of Defense, specifically in terms of structural integrity, accounting for roughly 23.2% of the $23.2 billion annual spent on corrosion-based repairs in marine applications [79]. Due to the difficulty of performing on-board examination of the IGSCC impact on structural damage and that IGSCC typically occurs at sensitization levels beyond the weldable range (usually, the alloy is considered weldable only when the sensitization level is below 30 mg/cm^2), existing welded repair approaches are not suitable for implementation on some marine structures. On the other hand, composite patch repair method, has been used as an alternative repairing method for marine structures since 2010 [80] and is especially advantageous on structural areas of complex shape or for parts that would require removal of large amounts of existing structure. Compared to traditional weld-based methods, composite patch repair of metallic structures has the advantage of providing uniform stress transfer, easy installation, customized stiffness, high specific strength, adaptability to complex substrate, and excellent corrosion resistance [81].

After the patch is installed, IGSCC becomes a non-visible damage mechanism of great concern. Multi-scale modeling is essential to predict damage propagation, because the aforementioned studies have suggested that IGSCC in Al alloys is a complicated process with the involvement of both atomic and microscopic behaviors, making it challenging to experimentally assess the damage behavior of the alloys under different degree of sensitization, particular, under dynamic service conditions. With this viewpoint, a predictive model of IGSCC induced structural damage that captures material degradation and crack propagation, as a function of sensitization in the Al alloy, can provide pertinent information for the maintenance of metallic structures with regards to component life and repair intervals.

However, it is difficult to predict the damage properties of the sensitized material for FE modeling, due to the lack of conclusive materials properties and the incomplete knowledge of the complex mechanism for IGSCC. Moreover, the intrinsic deficiency of continuum mechanics for describing arbitrary crack paths makes it prohibitive to model the complex fragmentations where cracking interweaves with continuously varying degrees of sensitization (DOS) in the metal part. To overcome these challenges, an alternative formulation of solid mechanics for handling discontinuities and long-range forces, PD, is utilized in this section for modeling the IGSCC and damage behavior of sensitized Al alloys. PD is a mathematical theory of mechanics that extends classical continuum mechanics (CCM) to include discontinuities [82, 83]. In the PD framework, each point in a material body represents a material particle location, and all these material points constitute the continuum. Material points interact with each other through the prescribed functions associated with constitutive information of the material body. These attributes in PD formulation present a unique capability of directly capturing fracture behavior along arbitrary paths without any predefined crack information. Moreover, PD employs displacements rather than displacement derivatives in its formulation, making it flexible to describe interfaces between dissimilar materials. This allows for the simulation of complex fracture phenomena with the involvement of air voids, defects, and grain boundaries. The input properties for varying phases of β-phase formation are calculated using quantum mechanics (QM).

Bondline Disbond

Disbond at the interface between metal and resin components of hybrid structure is yet another mode of non-visible damage that can cause sudden failure. Preliminary modeling and experimental

testing informed model development of this damage mechanism. As shown in Figure 62, disbond of the patch occurred at three locations, often simultaneously: (1) the metal resin interface, (2) through the resin itself, and (3) the resin and first fabric layer. Where disbond initiated was primarily a function of surface roughness, air voids, and inclusions. Investigative efforts following the integrated approach of Figure 5, resulted in the development of the DCB, ENF, and SLB testing effort previously discussed in section 3.2 to obtain the mode I, II, and mixed mode fracture energies for varying surface roughness profiles. The final test specimens of section 3.2 differed from the original specimen configuration shown in Figure 62 which used adherends of extremely different stiffness, the baseline composite patch and the metal plate. This specimen configuration did not result in consistent failure at the bondline nor was it possible to eliminate bending moments from being introduced during testing, even with the use of backing material to reinforce the less stiff component. Given these issues, the specimen configuration type discussed in section 3.2 and shown in Figure 63 was developed. As shown, this specimen configuration resulted in consistent plane strain crack growth which was constrained to either a metal/resin interface or through the resin, the mode of failure identified in the three and four point bend testing program. Results with metal/metal adherend specimen were then used to develop a cohesive damage formulation that simultaneously captured both interface disbond and resin fracture near the interface. This approach was validated and demonstrated to accurately predict bondline failure.

Figure 62. Interface disbond initiating at multiple locations.

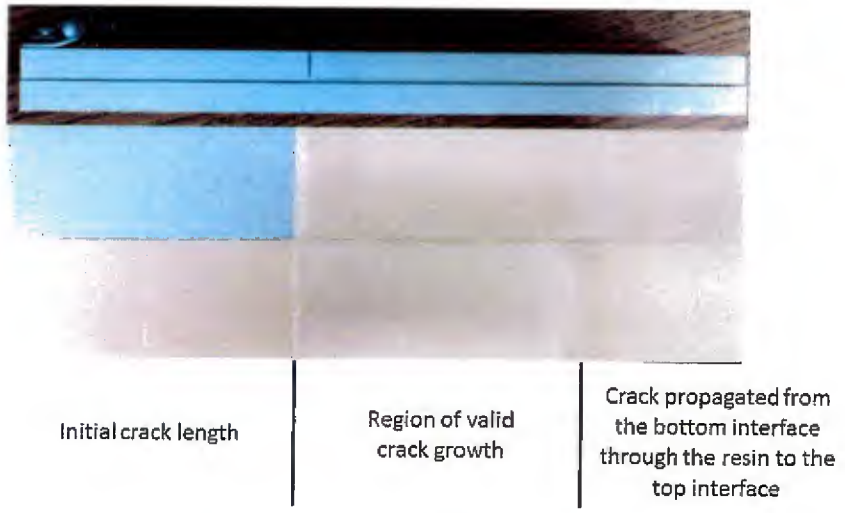

Figure 63. Specimen configuration producing repeatable, stable crack growth along the interface representing disbond of the patch from the metal.

Composite Damage

Damage mechanisms in the composite patch fall into two categories: (1) interlaminar delamination and (2) intralaminar damage. Interlaminar delamination occurs between two lamina, each consisting of a different fabric type for the baseline patch. As with the interface disbond, a cohesive damage model was developed based on experimental test results provided by NSWCCD to capture this damage mechanism. Intralaminar damage consists of microcracking in the resin and fiber breaks, buckling, and pullout. An extensive experimental testing program was performed to collect the material data needed for the Abaqus VUMAT for fabric reinforced composites.

4.2 Quantum Mechanics using Density Function Theory to Predict β-phase Properties

Mechanical properties of materials such as modulus, elastic constant, and fracture energies are important parameters for numerical modeling of hybrid structure damage tolerance. While experimental testing is possible for materials that have stable structure and can be synthesized in the laboratory, there is a large number of materials that are challenging to make and test due to their complex structure and dynamic response of properties to the environment. For example, 5XXX Al alloys are well suited to applications in marine vessels due to their low density and moderate strength. However, 5XXX Al alloys have a serious issue of precipitating Mg-concentrated β-phase in Al-Mg alloys at the grain boundaries of the matrix (sensitization) under service conditions. While determining the mechanical properties of the β-phase in Al-Mg alloys is essential in order to investigate their influence on the crack behavior of the structural part, the precipitated β-phase material is usually at the length scale of nanometers and is highly susceptible to electrochemical dissolution in salt water. The electrochemical dissolution in salt water makes it challenging to experimentally synthesize and test for material properties in marine conditions. However, quantum mechanics (QM) based first principle calculation, which only requires the types and approximate arrangement of atoms as input, provides the capability to explore the effects of chemical composition on material properties, eliminating dependence on material testing of each chemical composition.

First principle calculation is used to determine material properties directly from the basic physical quantities, such as the mass, charge, Coulomb force of an electron, etc., based on the principles of QM. Fundamentally, the calculation produces physical properties without the need for modeling or introducing various parameters, where modeling is used to correlate theoretical calculations and experimental results. Current implementation of this methodology, for the prediction of properties in new materials and further understanding the properties of existing materials, is spurred by advances in computational performance. In traditional QM based calculation methods, such as Hartree-Fock method and the methods beyond, the behavior of electrons in the system are described by wave functions. Since the wave functions depend on all spatial coordinates of all electrons in the system and these functions possess a high scaling computational cost associated with the number of atoms, calculations are limited to systems involving very few atoms and electrons (Figure 64a). On the other hand, the method within density functional theory (DFT) framework offers a balance between accuracy and computational efficiency well suited to most materials applications [84]. DFT treats the electron density as the central variable and thus only depends on the three spatial coordinates (Figure 64b), leading to a remarkable computational reduction compared to the traditional many-body wave function based computation method. With

the state-of-the-art Hohenberg-Kohn-Sham formulation of DFT, it is feasible to allow quantitative data to be generated for systems on the order of one thousand atoms.

Figure 64. Many-body view and DFT perspective in QM based first-principle-calculation

This section outlines the DFT-based first principles calculation for predicting the evolution of mechanical properties in Al alloys and the atomic interaction at the surface of Al alloys. The prediction capacity of first principles calculation was validated through the comparison of experimentally measured atomic lattice constant and bulk modulus of Al. The bulk modulus of the β-phase at varying stages of Mg content, which is usually formed at the nanometer size in grain boundary of 5XXX Al alloys due to sensitization, will be predicted. The effect of hydrogen adsorption on the fracture energies of Al will be discussed in depth. As will be discussed the section on microscale modeling, the bulk modulus and fracture energies calculated using QM will become input to the peridynamic models of microscopic crack behavior of sensitized 5XXX Al alloys.

All of the first principles calculations were performed using DFT with the Kohn-Sham approach implemented in Quantum Espresso, a plane-wave-based software package [85]. Energies of each model were calculated using plane-wave-based ultrasoft pseudopotential for atomic cores and Perdew-Burke-Ernzerh (PBE) exchange-correlation functional for all atoms [86, 87], with kinetic energy cutoff of 500 eV. The Brillouin zones were sampled with 8×8×8 Monkhorst-Pack k-points[88]. The electronic occupation of Kohn-Sham eigenstates was smeared by the Fermi-Dirac approach with width of 0.2 eV to aid in computational convergence, and all energies were extrapolated to T = 0 K.

Prior to the prediction of β-phase material properties, the accuracy of the QM calculations in determining materials property was validated by comparing the calculated atomic lattice structure and bulk modulus of Al with experimental measurements. The validation model was bulk structure optimization of face-centered cubic (fcc) Al with a 2x2x4 supercell and periodic repeat on three-dimensional Cartesian coordinates (Figure 65). In order to calculate the equilibrium structure, a series of volume values for the supercell were selected and fixed in each calculation, while all atoms in the model were fully relaxed using quasi-Newton algorithm built in Quantum Espresso with the convergence criteria of 0.05 eV/Å.

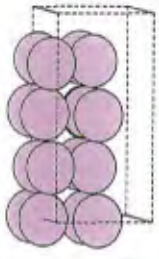

Figure 65. Illustration of the model for bulk structure optimization of fcc Al

In order to obtain the equilibrium structure of fcc Al, the total energy of each volume value of the supercell in the fcc Al model was extracted from the first principles calculation (the points in Figure 66). The equation of state (EOS) in terms of a quantitative relationship between the total energy and volume was established by the fit of all calculated results against the supercell volume with the stabilized jellium equation of state (SJEOS) method, which have demonstrated to be well suited for metal systems [89]. The equilibrium structure constant and bulk mechanical properties can be achieved from the SJEOS function.

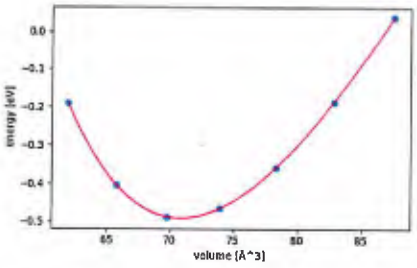

Figure 66. Total energy of fcc Al as a function of volume from first principle calculations (points). Solid line corresponds to the fit of calculated results by SJEOS method to achieve EOS function.

The equilibrium bulk structure and bulk modulus for fcc Al from first-principle calculation, as well as the reported experimental measurements, are summarized in Table 12. The equilibrium lattice constant of fcc Al was found to be 4.05 Å. This value is slightly larger but agrees with the experimental value (4.04 Å) measured by X-ray diffraction [90]. The calculated bulk modulus is slightly smaller but also agrees with the experimental value [91]. The agreement between the calculated and experimental value demonstrates the capacity of first-principle calculation to predict mechanical properties Al alloys with various Mg concentrations.

Table 12. The equilibrium lattice constant and bulk modulus for FCC Al from first-principle calculation. The predicted values are in good agreement with experimental observations from the literature.

Properties	This work	Experiment
Lattice (Å)	4.05	4.04
Bs (Gpa)	72.3	76.5

Based on the validation, the model utilized for bulk structure optimization of was a 2x2x4 supercell for each fcc Al-Mg alloy and a 1x1x1 unit cell for the β-phase, with all models repeated periodically in three dimensional coordinates (Figure 67). For each alloy system with the proposed bulk Mg concentration, a series of Al atoms (gray color) were replaced by Mg atoms (green color) in random lattice position. In order to calculate the equilibrium structure of each model, a series of values for the supercell volume was selected and fixed in each calculation, while all atoms in the model were fully relaxed using quasi-Newton algorithm until the forces were smaller than 0.05 eV/Å.

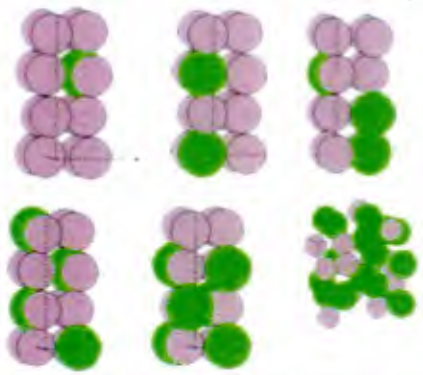

Figure 67. Illustration of the model for bulk structure optimization of Al alloys.

The EOS plot with SJEOS method for each Al alloy system was obtained from the first principles calculations (Figure 68). In all models, the first principal calculated total energy at each volume falls closely onto the fitted line, suggesting a good prediction using the SJEOS method for EOS function.

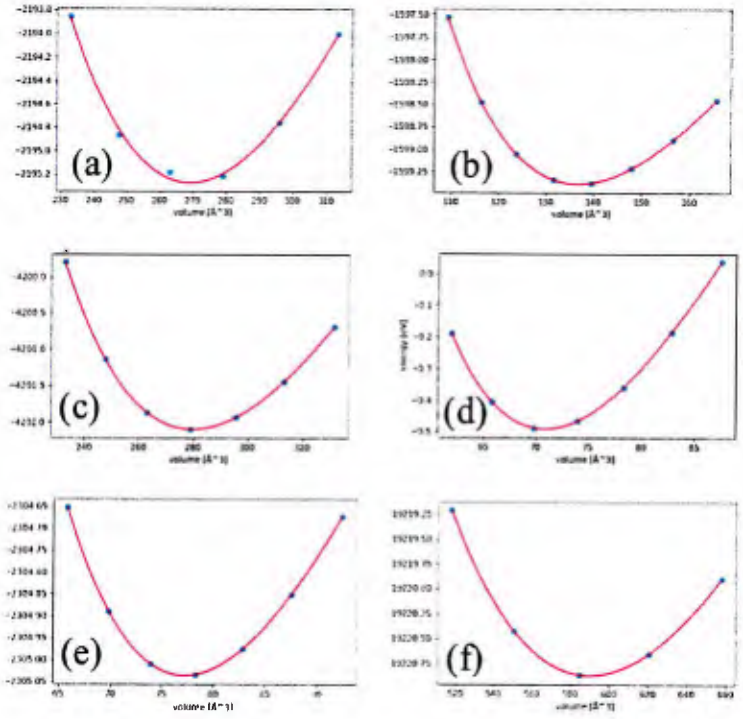

Figure 68. EOS fitting of total energy against volume for Al-Mg alloys

The predicted evolution of bulk modulus in Al alloys with different concentrations of Mg was plotted in Figure 69. The bulk modulus of the forming β-phase has little variation when Mg concentration is less than 10 %. However, for the β-phase during formation with Mg concentration higher than 10 %, there is an almost linear decrease of the bulk modulus with the increase of Mg

concentration. Particularly, the final β-phase has more than a 30% drop in bulk modulus compared with a β-phase with 5% Mg during formation.

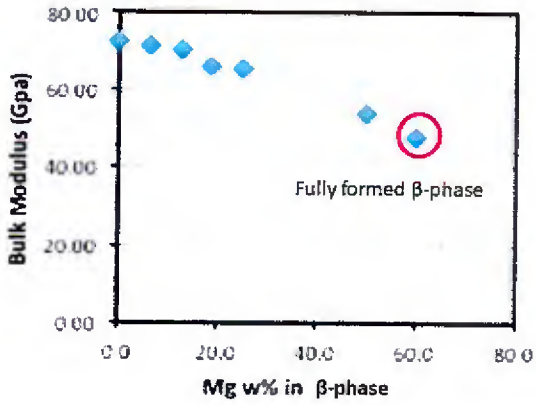

Figure 69. Predicted evolution of bulk modulus of β-phase at different Mg content during formation.

Current work alludes to hydrogen uptake in the aluminum alloys contributing to crack growth [92]. In the case of 5XXX series Al alloys, for example, the hydrogen produced due to the dissolution of β-phase under service conditions could adsorb on the metal atoms at the grain boundaries and the adsorption may occur along the length of crack, continuously evolving the state of the crack flanks influencing the process [93]. A number of differing mechanisms, such as hydriding; hydrogen induced local plasticity; and hydrogen induced local decohesion, should be investigated to understand hydrogen assisted cracking in Al alloys. However, each mechanism is consistent with only particular sets of phenomenological observations due to the difficulty of submicroscopic and atomic experimental study on hydrogen-metal interaction. Therefore, there is still a lack of correlation connecting the atomic level behavior of hydrogen-metal interaction to engineering properties degraded by hydrogen, such as fracture toughness [94]. The focus of the next discussion is to present a model that links the effect of hydrogen uptake on the decrease of macroscopic cohesive strength in Al to the first principles calculated fracture energy of Al with mobile hydrogen atoms adsorption.

At the atomic scale, fracture can be view as the rupture of atomic bonds (Figure 70a and b) that forms two new surfaces from a bulk system, and the energy cost to form the two new surfaces is called fracture energy [95, 96]. From first principles calculation, the total energy of a bulk system (E_{bulk}) and the total energy of a surface (E_{suf}) can be predicted. The fracture energy can thus be calculated as difference of the surfaces and the bulk system:

$$2\,\gamma(0) = 2E_{suf} - E_{bulk} \tag{16}$$

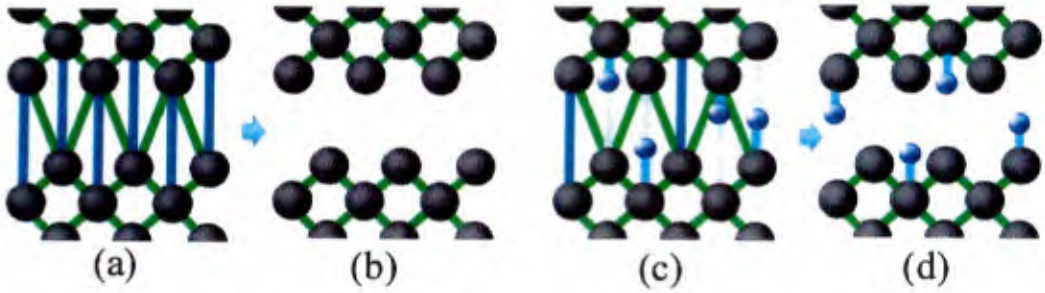

Figure 70. Atomistic view of fracture. The gray and purple spheres represent the metal and hydrogen atoms, and the green and blue line represents the bonds.

In the cohesion reduction mechanism [97], hydrogen uptake by metal atoms to an incipient fracture zone reduces the local atomic bonding, thus decreasing materials cohesive energy and facilitating crack formation (Figure 70 c and d). Through a Born-Haber cycle [98], the fracture energy of the material at a hydrogen atom coverage (θ) can be calculated as:

$$2\gamma(\theta) = -H_s + 2\,\gamma(0) + E_{ad}(\theta) \tag{17}$$

In Eq. 17, $2\gamma(\theta)$ is the fracture energy of a metal-hydrogen system along a certain plane, $2\,\gamma(0)$ is the fracture energy of a pure metal without hydrogen, H_s is the solution enthalpy of hydrogen in the bulk metal, and $E_{ad}(\theta)$ is the dissociative adsorption energy of hydrogen to for atomic hydrogen adsorbed on metal surfaces.

The atomistic fracture energy can be linked to the macroscopic cohesive strength of a metal system by the renormalized traction-separation law [99]. With the assumption that the effective critical opening displacement is independent of hydrogen coverage upon renormalization, the macroscopic impurity-dependent effective cohesive law can be related to the atomic level description of impurity coverage effects on the de-cohesion of metals in the following way (Eq. 18):

$$\frac{\sigma_c(\theta)}{\sigma_c(0)} = \frac{\gamma(\theta)}{\gamma(0)} \tag{18}$$

Where $0 \le \theta \le 1$ is the impurity coverage, $\sigma_c(\theta)$ and the $2\gamma(\theta)$ are the macroscopic critical stress and the fracture energy of a metal from first principle calculations, respectively.

Table 13 is a summary of the first principle calculated fracture energies, $2\gamma(\theta)$ of Al at various hydrogen coverage values (θ) with the Born-Haber cycle method [98].

Table 13. First principle calculated fracture energies of Al at different hydrogen coverage

θ	0.0	0.11	0.25	0.50	1.00
$\gamma(\theta)$ (J/m^2)	2.43	2.18	1.87	1.29	0.46

A fit to the first principle calculated data, in combination with Eq. 18, gives dependence of the effective cohesive law on hydrogen coverage on Al (111) surface as Eq. 19 and presented

graphically in Figure 71. Establishment of this correlation between hydrogen coverage and the macroscopic cohesive strength of a metal makes it feasible to predict damage behavior Al alloys at the microscopic level, as will be discussed in the next section.

$$\frac{\sigma_c(\theta)}{\sigma_c(0)} = 0.047\theta^2 - 0.713\theta + 0.998 \tag{19}$$

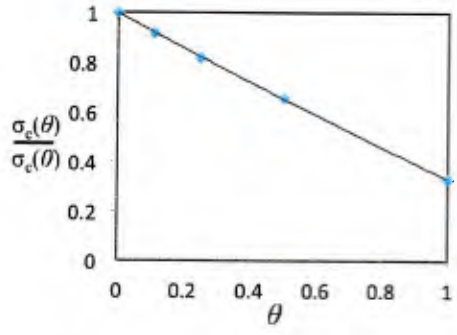

Figure 71. Dependence of cohesive law on hydrogen coverage.

4.3 Peridynamics to Model Crack Growth in Sensitized Al

PD theory unites the mathematical modeling of continuous media, particles, and cracks within a single framework [100]. The governing equations of PD, are valid even when there are discontinuities in the system because this formulation is based on integral or integro-differential equations containing no spatial derivatives. Partial derivatives do not exist on crack surfaces, therefore, integral equations are advantageous for solving problems involving fracture mechanics. These equations are based on a model where all of the internal forces within a body are described as points that interact with each other over finite distances. In contrast, in the classical theory of solid mechanics there is an assumption that there is a continuous distribution of mass within a body where all internal forces are contact forces.

This representation places heavy emphasis on the smoothness of the deformation in order for the partial differential equations (PDE) to accurately represent the physical behavior. Consequently, fracture mechanics techniques introduce many relations that are extraneous to the basic equations in classical continuum mechanics [100]. In PD, damage is incorporated into the force function by allowing bonds to break after a certain specified elongation. When a bond breaks, the existing load is distributed to other bonds that remain intact. The progressive breaking of bonds and subsequent redistribution of load is the driving force of crack growth within the PD model. PD introduced the ability to use the same equations at all points in the model of a deforming structure and thus limited the need for special techniques, such as the separation of crack growth laws based on the stress intensity factor in fracture mechanics. Due to the limitations of classical continuum mechanics with regards to the handling of discontinuities and singularities, it is not ideal for conditions and geometries as they become more complex or if they operate on smaller scales. Molecular dynamics (MD) provides the ability to understand material behavior at small length scales but cannot model

systems with sufficient size to compare to continuum models. PD theory attempts to treat both the nanoscale and macroscale behavior within the same system.

While FE analysis provides useful results and has traditionally been the most commonly accepted technique for classical continuum mechanics for several decades [101], PD was chosen to model crack growth in sensitized Al with randomly generated grain microstructure to avoid mesh dependency. FE analysis performs very well under small deformations or until cracks begin to grow. When a crack begins to grow in FE analysis, the crack will suffer from mesh effects where the crack will most likely follow the path of the mesh itself. This also requires re-meshing after each incremental crack growth and the needs for an external crack growth criterion [102]. The need for external crack growth criterion is cumbersome due to the complexity in obtaining and generalizing fracture data obtained experimentally along grain boundaries.

The capability of the PD model in predicting crack behavior is validated with experimental data available in the literature. The effects of the degree of sensitization (DOS) and hydrogen embrittlement on the damage behavior of sensitized Al alloy will be discussed. The performance of bonded composite patches damage prevention will be predicted. This work provides, for the first time in the literature, a PD model to investigate IGSCC in sensitized Al alloys.

The PD formulation can considered as the replacement of partial differential equations in classical theory of solid mechanics with integro-differential equations that are derived according to material points interactions within a body [82, 83]. The equation of motion for any material point at x in the reference configuration at time t can be expressed as Eq. 20.

$$\rho(x)\ddot{u}(x,t) = \int_H f(\eta,\varepsilon)dV_{x'} + b(x,t) \tag{20}$$

In the above equation, $\rho(x)$ and $u(x,t)$ are the material density and the displacement vector field at the material point x and time t, respectively. The variable b is the body force exerted on the material point x, and H is the neighborhood of the material point at x described by a scalar δ called the horizon. For convenient description of the kinematic information, the relative position of the two materials points x and x' in the reference configuration and their relative displacement are denoted as $\varepsilon = x' - x$ and $\eta = u(x',t) - u(x,t)$, respectively. The interaction of these two particles is expressed in term of a pairwise force function $f(\eta,\varepsilon)$ that corresponds to the macroscopic constitutive relationship of a material.

Because IGSCC in sensitized Al alloy is a process occurring at the grain boundaries in the brittle β-phase, the bond interaction can be well approximated by a linear elastic prototype microelastic brittle (PMB) material model [103, 104]. According to the PMB model, the constitutive equation characterizing the pairwise force can be expressed as Eq. 21.

$$f = cs \tag{21}$$

In the above equation, the constant c is called micromodulus which is a function of the material's bulk modulus K and horizon δ as shown in Eq. 22.

$$c = \frac{18K}{\pi\delta^4} \tag{22}$$

The variable s is called bond stretch which is defined in Eq. 23.

$$s = \frac{|\varepsilon+\eta|-|\varepsilon|}{|\varepsilon|} \tag{23}$$

The notation $|\varepsilon|$ and $|\varepsilon + \eta|$ in the above equation are the original bond length and deformed bond length in the material configuration. With a view toward modeling fracture in a deforming body, the critical stretch for bond failure s_0 is introduced to describe the bond break when stretched beyond s_0. The value of s_0 in the PMB model is given as a function of the material critical energy release rate G_0, the bulk modulus K, and horizon δ as in Eq. 24.

$$s_0 = \sqrt{\frac{5G_0}{9K\delta}} \tag{24}$$

With the introduction of critical stretch for bond failure, the PD damage at a point can be expressed as Eq. 25.

$$\varphi(x,t) = 1 - \frac{\int \mu(x,t)dV_{x'}}{\int dV_{x'}} \tag{25}$$

Where $\mu(x,t)$is a scalar-valued binary function that equals 1 if the bond stretch is smaller than the critical value s_0 and 0 otherwise. The total damage in a model is thus defined as the sum of damage at all material points extracted from the PD simulation (Eq. 26).

$$D_{model} = \sum_i \varphi_i\,(x,t) \tag{26}$$

All PD simulation was performed using a mesh free discretization method implemented in PDLAMMPS, an open source package with a focus on materials modeling [105]. An example of a stochastic volume element (SVE) developed for PD analysis is shown in
Figure 72. This particular model has a length of $\mathbf{1.6 * 10^{-2}}$ m, width of $\mathbf{0.32 * 10^{-2}}$ m and height of $\mathbf{0.16 * 10^{-2}}$m and the grain structure was generated using Dream3D [106]. Non-deterministic analysis was performed using the built in synthetic microstructure approach in Dream3D to generate models of random gain orientation with average grain size of $\mathbf{4.0 * 10^{-4}}$ m and a total amount of 6263 grains for this particular SVE. The model has a 3D cubic lattice of particles with the lattice constant $\boldsymbol{a = 1.0 * 10^{-4}}$ m and the horizon distance $\boldsymbol{\delta = 3a = 3.0 * 10^{-4}}$ m. The model contains 90321 particles, and each particle has a volume, $\boldsymbol{V = a^3 = 1.0 * 10^{-12}}$ m.

In order to simulate the effect of the DOS on the crack behavior of the model, the bottom quarter section of the model (i.e. $0 \leq z \leq 0.8$ mm) was assumed to be the sensitized region representing the outer surface of a sensitized Al plate, which contains 1303 grains. Following the literature discussion [107], the DOS is defined as total areal coverage fractions of grains by β phase in the sensitized region (A_{sen}) normalized to the total amount of grains in the model (i. e. $DOS = (A_{sen} * 1303)/6263 * 100\%$).

In this representative example, a layer of composite material with a thickness of $0.08 * 10^{-2}$ m and defined using smeared patch properties was added to the SVE for a preliminary study on the

effect of the composite patch on extending the structure integrity at the interface. This composite layer was added adjacent to the sensitized region (Figure 73). The bulk modulus and critical energy release rate of the composite were estimated to be $9.19\,Gpa$ and $2.63 * 10^4 J/m^2$, respectively[108]. The bonding strength between the metal part and the composite was estimated to be $1.28 * 10^3 J/m^2$ [109]. The efficiency of bonded patch for extending structure integrity of sensitized Al alloys is defined as the structure integrity increase of the sensitized Al alloy bonded with composite:

$$integrity\ increase = \frac{damge\ without\ patch - damge\ with\ patch}{damge\ without\ patch} * 100\ \% \qquad (28)$$

All of the simulations were performed at the constant temperature of $T = 300\ K$ under beam bending loading applied at the speed of $5\ m/s$. The Verlet algorithm was employed for integration with the timestep set to be $1.0 * 10^{-8} s$.

Figure 72. Example of an SVE used for the DOS study.

Figure 73. Example of an SVE that includes a composite patch layer added adjacent to the sensitized layer, indicated by the red line.

The structural integrity increase of the sensitized model due to the bonded composite patch was simulated for different DOS values (Figure 74). For this example, when the level of DOS is lower than 10%, the bonded composite patch is capable of increasing structure integrity by 60% to 90%. However, in the region with a DOS larger than 10%, the effectiveness of the composite patch in preserving structural integrity drops dramatically with increasing DOS.

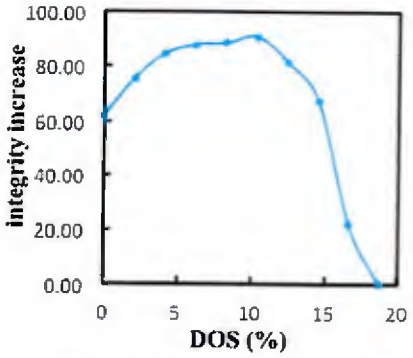

Figure 74. The effectiveness of composite patch repair of sensitized aluminum relative to the DOS.

4.4 Analytical Prediction of Branched and Kinked Crack Growth

Given the propensity of cracks in sensitized Al alloys to branch and deviate from a straight line due to the β-phase along the grain boundaries, an analytical method was further developed to determine the full stress field in a plate containing multiple cracks that can be straight, branched, or kinked (Figure 75). Results from this method also include the SIFs at all crack tips and kink angles with singularities. This information is provided to the PD model to predict new crack growth which is then input into the analytical model to update the crack pattern. Through a sequential loop, crack growth is predicted. The primary limitation of the analytical method is that the cracks must be through the entire plate and the same on the top and bottom (ie, the crack cannot slant through the plate). The analytical method is valid for stress field prediction in a brittle, isotropic material in plane stress or plane strain under linear elastic fracture conditions. These limitations were deemed acceptable for this research as cracking through the brittle β-phase meets linear elastic fracture conditions, and the uncertainty in measuring cracks in sensitized aluminum is of the same order of magnitude as the uncertainty due to the limitations.

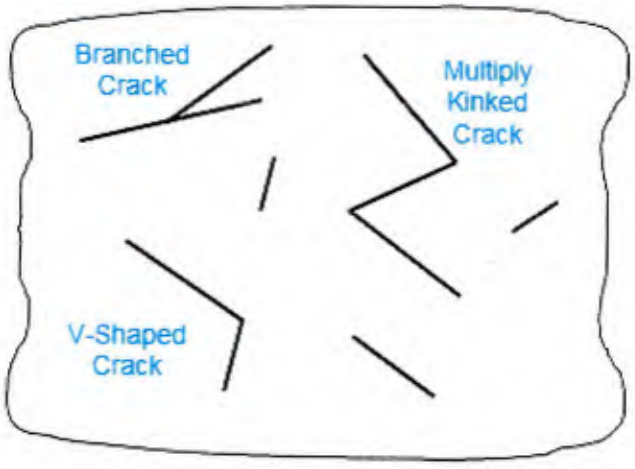

Figure 75. Metallic plate containing multiple cracks.

An overview of the method is provided here, and the full details can be found in [110-114]. New functionality added specifically for this research included an improved method for the assignment of points along the crack segments where the traction free condition is enforced, a new model for kinked cracks that also branch, and automated sensitivity analysis and uncertainty quantification.

The dislocation distribution method is summarized with an emphasis on highlighting the key concepts that form the foundation of this model development. Given an existing crack array in a plate, the problem of determining the stress field is solved by approximating the opening displacement profile for each crack segment such that all crack faces are traction-free. While these opening displacements are mathematical approximations of the true crack opening shape, deviations from an exact traction free condition are typically on the order of 10^{-6} for most crack arrays. To solve this boundary condition problem, the principal of superposition is applied by modeling the cracked plate as two separate problems (Figure 76), the trivial problem and the auxiliary problem. The sum of the two problems is the solution to the original problem. The trivial problem is the stress field in the plate without the cracks, while the auxiliary problem is the cracked plate under tractions that result in traction-free crack faces. Solution of the auxiliary problem comprised the bulk of the computational effort.

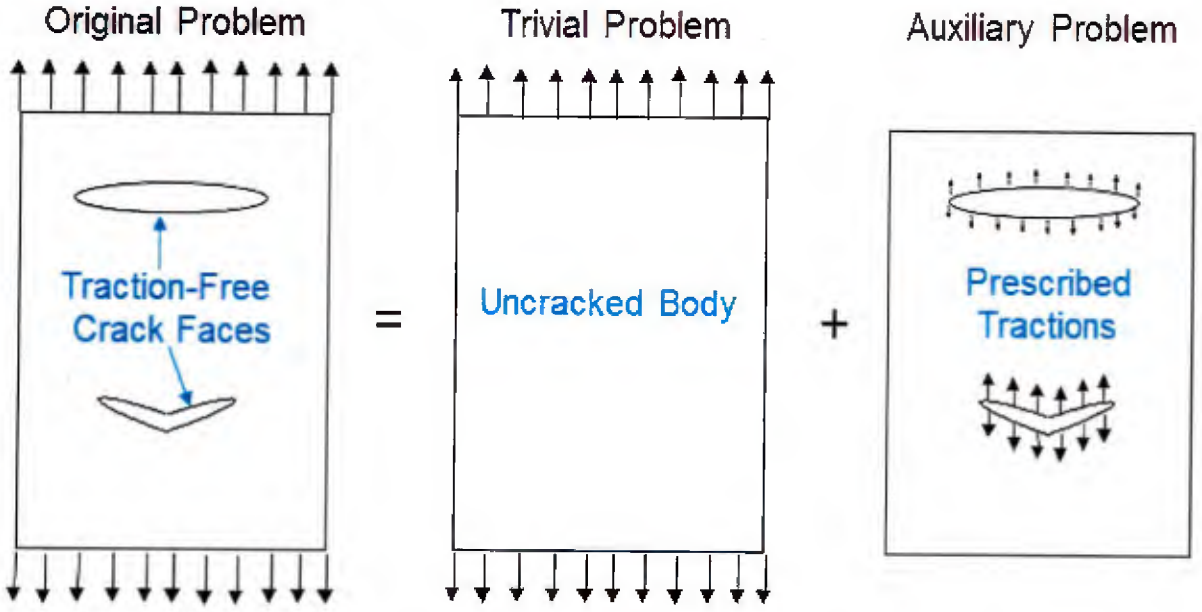

Figure 76. The solution process of superposition to achieve traction-free crack faces.

Eq. 29 provides the equations that are used to enforce the traction-free condition. The left side of the equations is a function of the applied tractions while the right hand side is a function of the opening displacements. The stress fields (Eq. 30) induced in the plate by each individual crack are denoted as $s^{(i)}$, and these stress equations are formulated by integrating the dislocation distributions used to define a crack opening displacement profile (Eq. 31). Dislocation distributions are built from series of terms that capture essential crack behavior such as that occurring at crack tips and wedges.

$$\sigma^{\infty}_{XY} n_Y + \sigma^{\infty}_{XX} n_X = -n_Y \sum_{i=1}^{c} s^{(i)}_{XY} - n_X \sum_{i=1}^{c} s^{(i)}_{XX}$$

$$\sigma^{\infty}_{YY} n_Y + \sigma^{\infty}_{XY} n_X = -n_Y \sum_{i=1}^{c} s^{(i)}_{YY} - n_X \sum_{i=1}^{c} s^{(i)}_{XY}$$

(29)

n_y, n_x	-- crack face normals
c	-- number of crack segments
$s^{(i)}$	-- stress field resulting from j^{th} crack segment
σ^{∞}	-- applied tractions

$$s^{(i)}_{xy}(z) = -\frac{2G}{\pi(1+\kappa)} \left\{ y\,\mathrm{Re}\left(Z^2_{2i}\right) + \mathrm{Re}\left(Z^1_{1i}\right) + y\,\mathrm{Im}\left(Z^1_{2i}\right) \right\}$$

$$s^{(i)}_{yy}(z) = -\frac{2G}{\pi(1+\kappa)} \left\{ \mathrm{Re}\left(Z^2_{1i}\right) - y\,\mathrm{Im}\left(Z^2_{2i}\right) + y\,\mathrm{Re}\left(Z^1_{2i}\right) \right\}$$

$$s^{(i)}_{xx}(z) = -\frac{2G}{\pi(1+\kappa)} \left\{ \mathrm{Re}\left(Z^2_{1i}\right) + y\,\mathrm{Im}\left(Z^2_{2i}\right) + 2\,\mathrm{Im}\left(Z^1_{1i}\right) - y\,\mathrm{Re}\left(Z^1_{2i}\right) \right\}$$

(30)

$$Z^{\eta}_{1i} = \int_0^a \frac{\mu_{\eta i}(t)\,dt}{z - t}$$

$$Z^{\eta}_{2i} = \int_0^a \frac{\mu_{\eta i}(t)\,dt}{(z-t)^2} = -\frac{d}{dz} Z^{\eta}_{1i}$$

(31)

4.5 High Fidelity FE Model to Investigate Interacting Damage Mechanisms

Performing physical experiments to carry out a comprehensive study that includes all variations of all design parameters and potential configurations is prohibitive due to time constraints and cost. Numerical modeling offers an alternative method to efficiently explore designs and investigate the effects of parameters on patch performance after validating a baseline model through experimental testing. Therefore, a high-fidelity 3D FE model, as shown in Figure 77, was developed to capture the damage mechanisms previously discussed. Each fabric layer is explicitly modeled, and cohesive elements are included between each layer to capture delamination between plies. The numerical simulations are executed in the FE code ABAQUS [115]. Each lamina is individually modeled with continuum shell elements (SC8R). The CDM damage model of each lamina is implemented using a VUMAT user subroutine [116, 117]. Cohesive elements with a triangular traction-separation law integrated in ABAQUS are used to detect the interlaminar damage and are also included at the metal/resin interface to predict patch disbond. The input parameters for the cohesive elements, including the stiffness, strength, and element size, are selected according to guidelines suggested by Turon [118]. The aluminum substrate is modeled with solid elements (C3D8R).

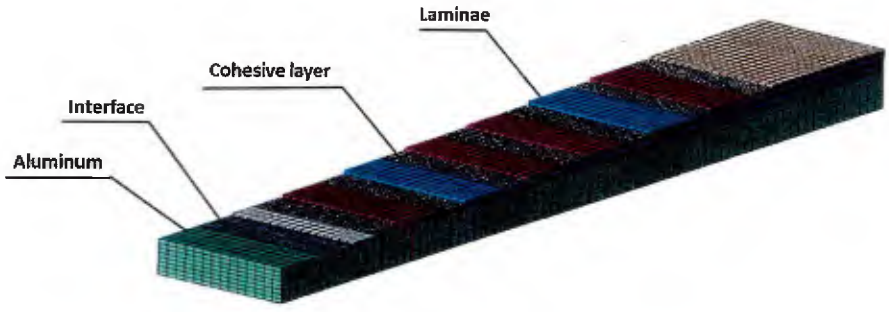

Figure 77. The laminae, the cohesive layers, the metal/resin interface, and the aluminum are modeled individually in the high fidelity model of hybrid structure.

Damage modeling in the patched structure requires the interaction of different methodologies. The Continuum Damage Mechanics (CDM) is used to model the intralaminar damage, fiber fracture, and matrix cracking. The Cohesive Zone Method (CZM) is used to model the interlaminar damage (delamination) and the disbond of the interface between the composite patch and the aluminum. Plasticity is included as the only damage type in the aluminum as PD is applied for detailed damage analysis. A preliminary investigation using Johnson-Cook damage modeling indicated zero change in results; therefore, damage modeling in the metal is not included in the high fidelity FE model, instead boundary conditions and loading on an element are provided to a PD model for detailed analysis and prediction of degradation effects and crack growth in sensitized aluminum. No damage was observed in unsensitized Al without an existing crack during experimental testing other than plastic deformation.

The CDM approach has been extensively studied to predict composite failure modes, especially in investigations of impact damage modeling. The CDM enables an easy integration of stress or strain

failure criteria and fracture mechanics. The stress or strain failure criteria predict damage initiation and the fracture mechanics approach captures damage evolution by correlating the damage variables to fracture energy. The load carrying capacity of composites progressively degrades due to the accumulation of microfiber/matrix cracks and the plasticity of the matrix prior to ultimate failure. To quantify damage at the macro scale caused by microcracks, the CDM describes the degradation of material properties. The CDM uses the damage variables to gradually reduce the material stiffness. Each lamina is modeled as a homogeneous orthotropic material. The elastic damage model is utilized for fiber dominated tensile or compressive failure while the elastic-plastic damage model is applied for matrix-controlled shear failure.

Constitutive equations for lamina with damage variables in the elastic domain are considered in plane-stress and take the form:

$$\begin{bmatrix}\varepsilon_{11}^{e}\\ \varepsilon_{22}^{e}\\ \varepsilon_{12}^{e}\end{bmatrix}=\begin{bmatrix}\frac{1}{(1-d_{11})E_{11}} & \frac{-\nu_{12}}{E_{11}} & 0\\ \frac{-\nu_{21}}{E_{22}} & \frac{1}{(1-d_{22})E_{22}} & 0\\ 0 & 0 & \frac{1}{(1-d_{12})2G_{12}}\end{bmatrix}\begin{bmatrix}\sigma_{11}\\ \sigma_{22}\\ \sigma_{12}\end{bmatrix},\qquad d_{11},d_{22},d_{12}\in[0,\,1] \tag{32}$$

where d_{11} and d_{22} are damage variables responding to fiber fracture along the 11 and 22 directions, d_{12} is the damage variable associated with matrix deterioration in shear deformation as shown in Figure 78. To distinguish between tensile and compressive fiber failures, d_{11} and d_{22} are defined in the form:

$$d_{11}=d_{11}^{t}\frac{\langle\sigma_{11}\rangle}{|\sigma_{11}|}+d_{11}^{c}\frac{\langle-\sigma_{11}\rangle}{|\sigma_{11}|},\quad d_{22}=d_{22}^{t}\frac{\langle\sigma_{22}\rangle}{|\sigma_{22}|}+d_{22}^{c}\frac{\langle-\sigma_{22}\rangle}{|\sigma_{22}|} \tag{33}$$

$$\langle x\rangle=\begin{cases}0, & x<0\\ x, & x>0\end{cases}$$

where d_{11}^{t}, d_{11}^{c} are components of d_{11}, related to fiber fracture under tensile and compressive loading, respectively. Though the constitutive equations (Eq. 32) based on the stiffness decay model is straightforward to describe the material degradation, the concept of effective stress from the strain equivalence theory is generally applied to present the constitutive model as

$$\begin{bmatrix}\varepsilon_{11}\\ \varepsilon_{22}\\ \varepsilon_{12}^{e}\end{bmatrix}=\begin{bmatrix}\frac{1}{E_{11}} & \frac{-\nu_{12}}{E_{11}} & 0\\ \frac{-\nu_{21}}{E_{22}} & \frac{1}{E_{22}} & 0\\ 0 & 0 & \frac{1}{2G_{12}}\end{bmatrix}\begin{bmatrix}\bar{\sigma}_{11}\\ \bar{\sigma}_{22}\\ \bar{\sigma}_{12}\end{bmatrix},\quad\begin{bmatrix}\bar{\sigma}_{11}\\ \bar{\sigma}_{22}\\ \bar{\sigma}_{12}\end{bmatrix}=\begin{bmatrix}\frac{\sigma_{11}}{(1-d_{11})}\\ \frac{\sigma_{22}}{(1-d_{11})}\\ \frac{\sigma_{12}}{(1-d_{12})}\end{bmatrix} \tag{34}$$

The effective stress, $\bar{\boldsymbol{\sigma}}$, is defined as the stress on undamaged material responding to the same strain on damaged material caused by the nominal stress, $\boldsymbol{\sigma}$. The effective stress provides a direct approach to define the damage initiation criteria and damage evolution. The damage is initiated once the effective stress reaches the value of material strength (Eq. 35).

$$\frac{\bar{\sigma}_{ij}}{x_{ij}}=1,\qquad i,j=1,2 \tag{35}$$

X_{11} and X_{22} are the tensile or compressive strength for uniaxial loading along the fiber direction and X_{12} is the shear strength. After the initiation of damage, the evolution of d_{11} and d_{22} is described by the exponential equation (Eq. 36).

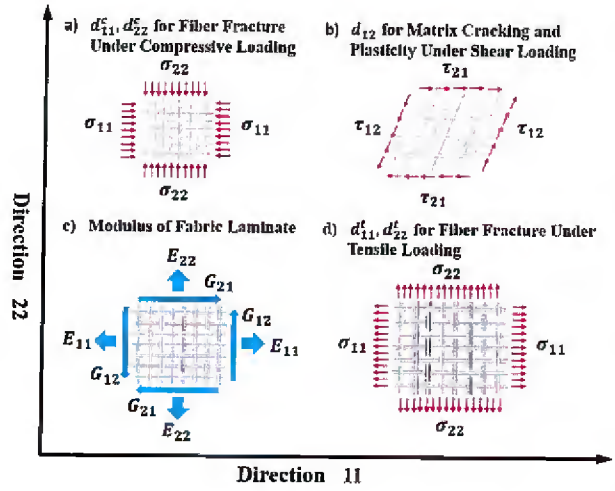

Figure 78. Damage variables used to model degradation of fabric reinforced laminae under different loading conditions.

$$d_{ii} = 1 - \frac{1}{k_{ii}} \exp\left\{-\frac{2U_0^{ii}L_c}{G_{ii}^f - U_0^{ii}L_c}(k_{ii} - 1)\right\} \qquad i = 1,2 \qquad (36)$$

$$k_{ii} = \frac{\bar{\sigma}_{ii}}{X_{ii}}, \quad U_0^{ii} = \frac{X_{ii}^2}{2E_{ii}}$$

where G_{ii}^f is the fracture energy of the laminae in the ii direction, U_0^{ii} is the elastic energy density when damage is initiated and L_c is the characteristic length of the element. To ensure the nondecreasing behavior of d_{11} and d_{22}, L_c needs to satisfy the following requirement (Eq. 37).

$$G_{ii}^f - U_0^{ii}L_c > 0 \qquad (37)$$

Therefore, the element size should be small enough to meet this requirement when implementing the damage evolution (Eq. 36) in finite element analysis.

Different from d_{11} and d_{22}, the evolution of d_{12} is described using the equation (Eq. 38) linear in $\ln(k_{12})$,

$$d_{12} = \alpha_{12}\ln(k_{12}), \quad k_{12} = \frac{\bar{\sigma}_{12}}{X_{12}} \qquad (38)$$

where α is a material constant which is measured by experimental testing and discussed later in the section of determination of material properties.

In addition to the elastic response above, plasticity behavior appears in fabric lamina under shear loading, which is described by the Ludwik-Hollomon [119] equation (Eq. 39),

$$\bar{\sigma}_{12} = \tilde{\sigma}_y + C(\varepsilon_{12}^p)^P, \qquad \varepsilon_{12}^p = \varepsilon_{12} - \varepsilon_{12}^e \tag{39}$$

where $\tilde{\sigma}_y$ is the effective stress corresponding to the normal stress at the yield point, ε_{12}^p is the plastic part of the total strain ε_{12}, C and P are material properties. The lamina fails when the plastic strain reaches a maximum value ε_{max}^{pl}.

The CDM presented above is for in-plane damage, which is aimed solely at predicting damage within individual lamina of the composite patch such as fiber fracture and matrix cracking. For out-of-plane damage, CZM is applied to model the delamination between plies and the disbond at the composite/metal interface.

The triangular traction-separation law (Figure 79) is selected because of its simple constitutive equations (Eq. 40) and widespread use [120]. Results have been demonstrated to be relatively invariant with respect to the shape of the traction-separation curve [47], and the triangular shape was able to accurately predict separation damage for this study.

$$\begin{cases} t = K\delta, & t \le t^0 \\ t = \frac{t^0(\delta - \delta^f)}{\delta^0 - \delta^f}, & t > t^0 \end{cases} \tag{40}$$

where t is the traction, δ is the separation, K is the interface stiffness relating the traction and corresponding separation before the initiation of the damage, t^0 is damage initiation stress, δ^0 is the separation where the damage initiates, and δ^f is the maximum separation where the element totally fails. The critical fracture energy G_c has the same value as the shaded area under the triangle in Figure 79. G_c is directly measured from experimental results while t^0, K and δ^f are obtained by empirically fitting to the experimental data.

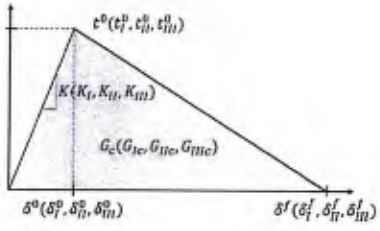

Figure 79. Triangular traction-separation law of the CZM.

To predict the delamination in the composite patch resulting from mixed mode fracture, the quadratic stress criterion (Eq. 41) is used to determine the damage initiation and evolution,

where t_I, t_{II}, t_{III} are tractions for Mode I, Moe II and Mode III fracture t_I^0, t_{II}^0, t_{III}^0 are the damage initiation stresses for the three modes of fracture.

$$\left\{\frac{\langle t_I \rangle}{t_I^0}\right\}^2 + \left\{\frac{t_{II}}{t_{II}^0}\right\}^2 + \left\{\frac{t_{III}}{t_{III}^0}\right\}^2 = 1 \tag{41}$$

Damage initiates when the left part of Eq. 41 is equal to unity.

The equation proposed by Benzeggagh and Kenane [121], one of the most widely used expressions for the critical energy release rate of a mixed-mode loading situation, is used as the mixed mode fracture criterion (Eq. 42).

$$G_c = G_{Ic} + (G_{IIc} - G_{Ic})\left(\frac{G_{II}+G_{III}}{G_I+G_{II}+G_{III}}\right)^{\eta} \tag{42}$$

where G_{Ic} and G_{IIc} are the critical energy release rates for Mode I and Mode II fracture, G_I, G_{II} and G_{III} are energy release rate for the three modes of fracture, η is a material property measured by experimental testing, and G_c is the critical energy release rate for mixed-mode fracture.

The elastic-plastic properties of the aluminum are determined from cylindrical tensile testing, as shown in Table 1. The Ludwik-Hollomon [119] equation (Eq. 43) is used to describe the strain hardening phenomenon,

$$\sigma = \sigma_y + K(\varepsilon_p)^n \tag{43}$$

where σ is the stress, σ_y is the yield stress, ε_p is the plastic strain, K and n are material properties.

The properties of each type of lamina (each reinforced with a different fabric type) are either obtained from experimental test results, provided by the manufacturer, or estimated from properties of similar materials in the literature. Due to the lack of shear property data, four lamina layers consisting of different fabric types are assigned the same shear properties. The assumption is made based on the fact that the four different laminae have the same matrix which dominates the laminae shear properties. The effects of this lack of data are discussed in section 5.2.

DCB and ENF tests on Hexcel 7500 reinforced epoxy laminates are used to determine the interlaminar properties (tests are performed by the NSWCCD in accordance with ASTM D5528, and ASTM D7905). The intralaminar fracture toughness of Hexcel laminae is estimated from the stress intensity factor of a similar E-glass/Epoxy weave fabric, which is measured by Mandell et al. [122] using a double edge notched specimen. The intralaminar fracture toughness of E-BX/E-LT is estimated from a double edge notched fracture test [123] of the $[90/0]_S$ E-glass/epoxy composite. Using the technique and procedure employed by Johnson [116], the shear properties are derived from the glass/Epoxy cyclic stress-strain curves from Johnson's [116] 45° tension test.

This model was validated and investigated under four point bending, three point bending, and low velocity impact. The four point bending results are provided and discussed as a representative example. The high fidelity FE model loaded under four point bending is shown in Figure 80. This model was loaded in varying configurations to engage different damage mechanisms.

Figure 80. Sideview of the high fidelity model loaded under four point bending.

The four different loading configurations discussed in section 3.4 presented multiple damage mechanisms contributing in varying degrees to the total energy absorbed by the hybrid structure. Figure 81 shows representative examples of damage progression for each of the four configurations, including the sequential strain fields of the intact specimens, damage initiation, damage evolution, and failure as well as the simulation results at failure. The load-displacement curves calculated from FE models are compared with the experimentally obtained results in Figure 82 for the four different specimen configurations. The simulation results quantitatively and qualitatively capture the experimental results reasonably well. As will be discussed in section 5.2, many of the input parameters represented by low quality data are shown to be highly influential on the damage tolerance and predictive capability of this model.

Damage in specimen A initiates at the site having the maximum shear force and moment in the form of interlaminar delamination. Due to the symmetry of the geometry, the damage should theoretically initiate simultaneously at both sites under the loading pins. However, microstructure variation due to inherent variability between specimens such as air voids, inclusions, and mechanical properties at the two sites causes initiation at one site to dominate failure. For the specimen shown in Figure 81a, the damage initiates on the left side and then propagates to a failure-inducing interlaminar delamination in the composite patch rather than a disbond at the interface between composite and aluminum. To initiate damage in the FE analysis, a small area at the initiation site on one side is assigned with lower strength cohesive elements to simulate the material asymmetry. Figure 82a shows that the simulation correctly predicts load drop due to the delamination and the maximum load compared with the experimental results.

Specimen B shows large areas of intralaminar damage and interlaminar delamination. The top layer of the composite patch fails first in the form of fiber fracture and delamination due to the presence of maximum tensile stress. Then the fracture and delamination of other layers in the composite patch followed one-by-one, as shown in Figure 81b. For the load-displacement curve of specimen-B in Figure 82b, the model captures the progressive damage behavior of the composite patch. The first load peak P_1 is related to the intralaminar fracture delamination of the first layer (Layer 1). As shown in the visualization of the simulation result, the shear failure of the two $\pm 45^{\circ}$ oriented E-BX 1200 laminae (Layer 4 and 5) causes the sudden drop of the load after the second load peak P_2, which indicates that the load carrying capacity between P_1 and P_2 mainly depends on the shear properties of the laminae which is governed by the resin.

Interlaminar delamination is again observed in specimen C at the same layer as in specimen A. When comparing the picture of specimen C in Figure 81, it is clear that specimen C exhibits minimal plastic deformation, because the composite patch, which presents a more brittle nature, becomes the main load-bearing component. The damage area in specimen C is much smaller than that in specimen A since the notch in aluminum reduces the flexural stiffness of the patched structure and subsequently the stress of the specimen.

Interface disbond dominates in specimen D while there is no disbond appearing specimen C, as shown in Figure 81. Specimen D is able to produce a higher disbond stress as the unnotched part in specimen D (aluminum) is much tougher than that in specimen C (composite).

The simulated load-CMOD curves of specimens A and B exhibit better quantitative comparison with the experimental results than that of specimens C and D. This might be caused by the fact the stress concentration area of specimens C and D is near the composite/aluminum interface and the interfacial properties used in the FE model are not of high quality. Moreover, the CNC machined initial notches in specimens C and D can potentially result in some damage in the composite and interface near the machining area and that damage is not considered in the FE models.

The energy absorbed by the patched structure is calculated from the FE results. The mechanisms capable of absorbing energy include the plastic deformation in aluminum, shear plasticity in laminae, the intralaminar fracture of the laminae, delamination within the patch and disbond at the interface. The contributions of the different damage mechanisms to the final energy absorption are calculated, as shown in Figure 83. As per the design of experiments, the different specimen configurations exhibit significant differences in the energy absorption distributions. The pie chart of specimen A shows more than two-thirds of the total absorbed energy is from the plasticity in the aluminum and the rest is from the delamination and plasticity in the laminae. Specimen B shows a similar distribution as specimen A except for presenting a small amount of energy from the fracture of the laminae. Since specimens A and B are essentially the same type of specimen, it can be concluded that different loading conditions can initiate different damage mechanisms.

For specimen C, the loading condition is the same as specimen A, but the energy is only absorbed by the composite patch compared against specimen A. The notch in the aluminum makes the composite patch the main bearing component. Likewise, the notch in the composite makes the aluminum the main bearing component in specimen D and most of the energy is absorbed by the aluminum. The difference between specimens A and C versus specimens B and D shows the preexisting damage in the patched structure significantly changes the energy absorption distribution. According to the pie charts of specimens A and B, although the composite patch is much more brittle than the aluminum, it contributes about one-third of the total energy absorbed. As depicted in Figure 83, the shear plasticity of the laminae and interlaminar delamination are the two main mechanisms in the patch that absorb the highest amount of energy. These mechanisms are governed by the matrix properties of the composite. Hence, the selection of the matrix material is an important criterion when designing patched structure to maximize energy absorption.

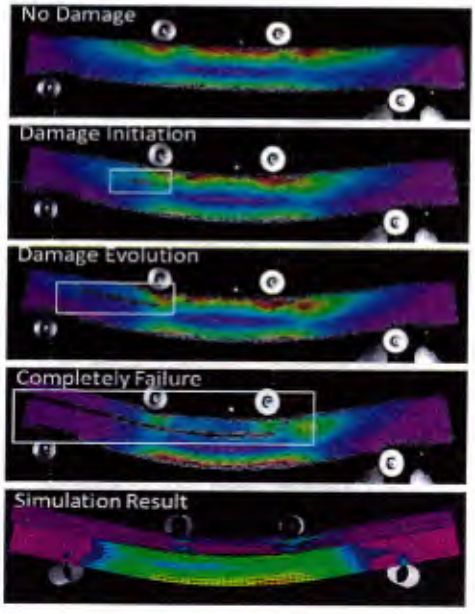

(a) Specimen A

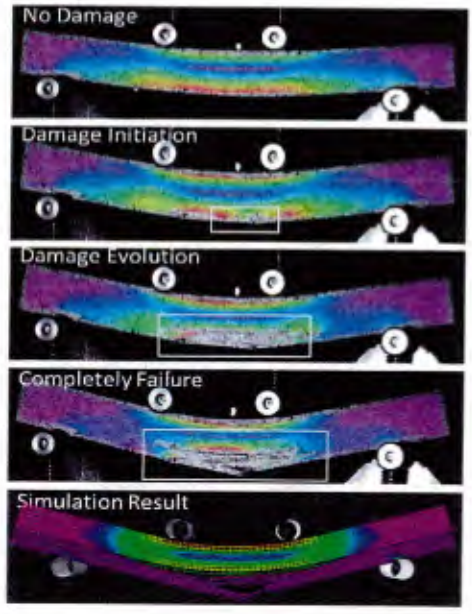

(b) Specimen B

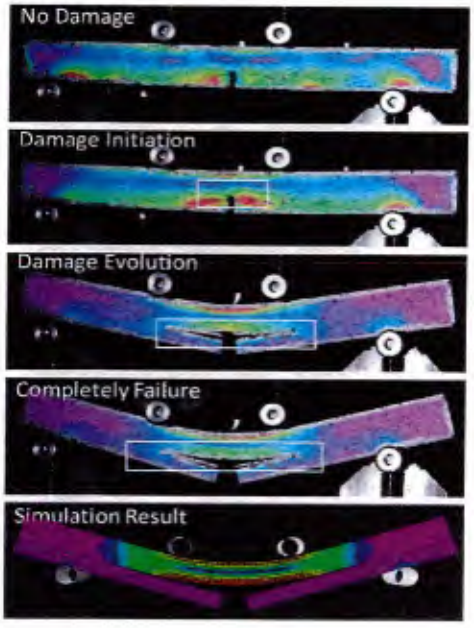

(c) Specimen C

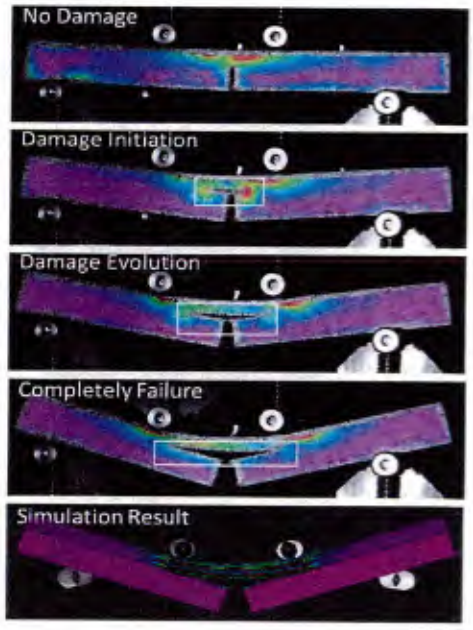

(d) Specimen D

Figure 81 Damage propagation of four-point bending specimens recorded with DIC, the white box indicates damage area and the corresponding simulation results at failure Tracking the many damage mechanisms in addition to the load displacement behavior is required for rigorous validation of the computational results.

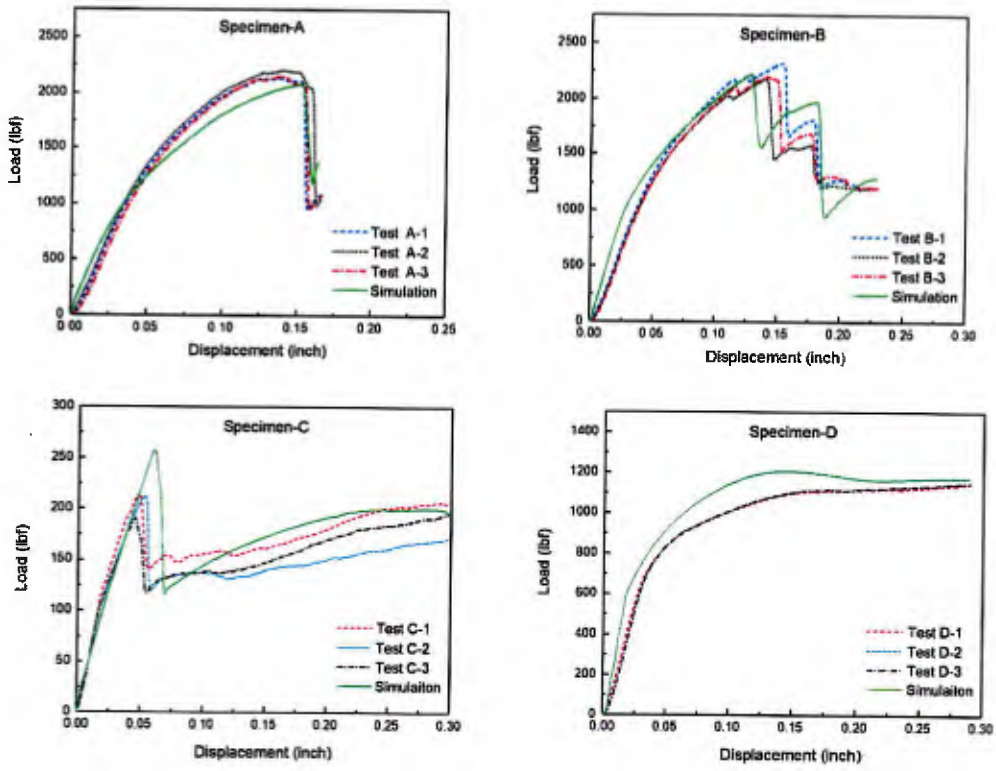

Figure 82. Comparison between the displacement-load curve from simulation and experimental test for different specimen configurations.

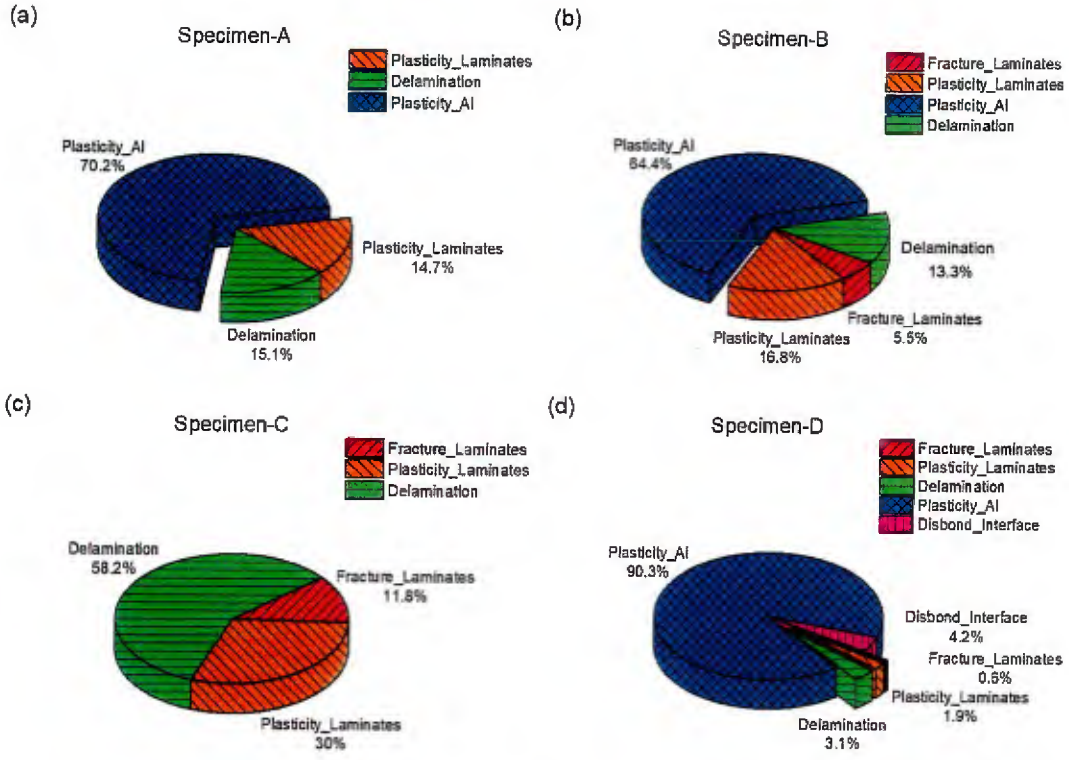

Figure 83. The final energy absorption distribution calculated from the models of different specimens for different mechanisms.

5 Demonstration Examples

The multi-scale models were developed to be readily interchanged and sequentially applied to investigate damage tolerance under in-service loading conditions. To demonstrate the plug and play capability of the models and to provide a few examples of scenarios that can be investigated using the models, three examples cases are discussed (Figure 84). In example 1, the analytical crack growth model and PD model are used to investigate crack growth in sensitized aluminum for varying amounts of hydrogen coverage at the crack front. Example 2 demonstrates the use of the high fidelity model and probabilistic toolkit to explore and quantify the effects of input parameters characterized by low quality data. The high fidelity model is loaded under three point bending to investigate the effects of DOS in the aluminum on damage propagation in example 3.

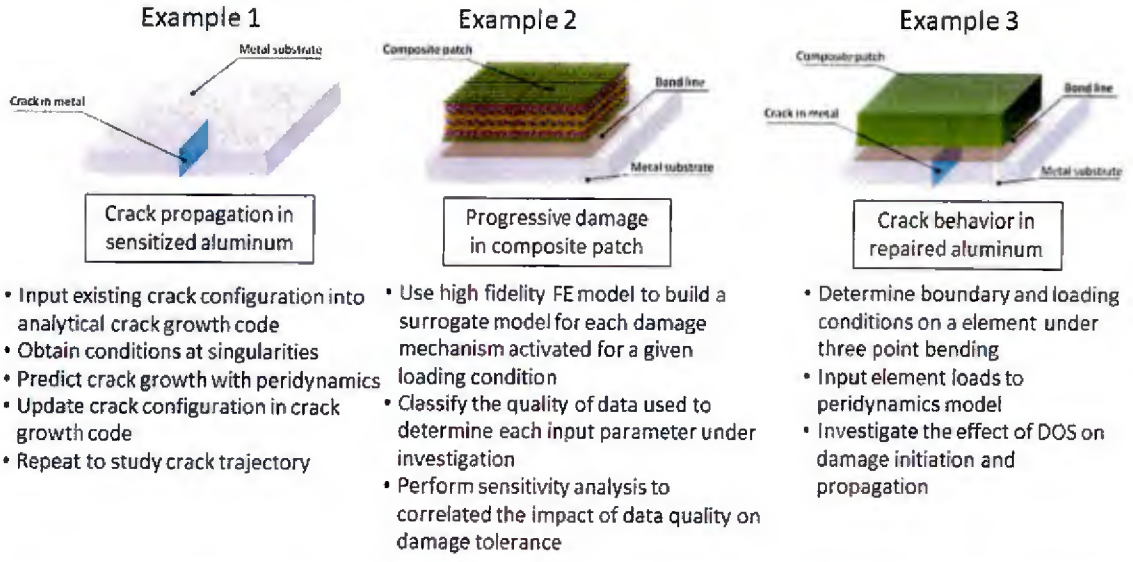

Figure 84. Example problems that demonstrate the plug and play capability of the multi-scale models to investigate damage tolerance for in-service loading conditions.

5.1 Hydrogen Effect on Crack Growth in Sensitized Al Alloy

As discussed in section 4.2, hydrogen coverage at crack tips was used to propagate IGSCC in sensitized Al-Mg alloy through embrittlement where the enhanced decohesion tends to reduce the bonding strength of grain boundaries. The increase of hydrogen coverage is described by the decrease of the maximum bond stretch in the PD model. With the developed relationship between critical energy release rate (G_c^H) of Al and hydrogen coverage from first principles calculations, the hydrogen coverage effect on crack damage sensitized Al-Mg alloy was explored by PD modeling. The analytical crack growth model was used to determine the loading for the PD analysis by calculating the displacement field at a crack tip in a branched crack. This process is depicted in Figure 85.

Results of this study show that although the effect of hydrogen adsorption and coverage is more significant at a high DOS level (DOS = 18.98 %) than that at a low DOS level (DOS = 4.16%), the hydrogen effect on crack damage is obvious only in the situation of high coverage (above 40% as shown in Figure 86). This predicted trend is well validated with the recent experimental study of hydrogen embrittlement effect on the IGSCC of sensitized 5083-H31 Al alloy, where a fast rate of IGSCC is only observed for the alloy with at least 60% of H concentration at the surface [124]. Figure 87 shows the difference in crack path for varying hydrogen coverage. This crack path is used to update the analytical model to then obtain the new strain conditions at the crack tip to repeat the process to predict the next increment of crack growth.

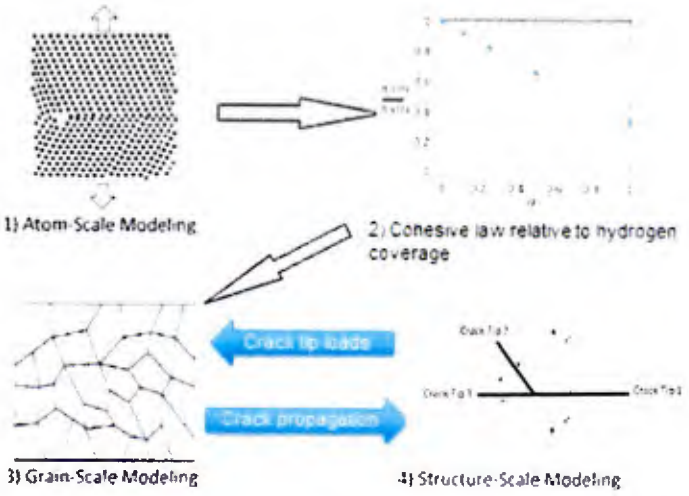

Figure 85. Flowchart of the multi-scale models selected to investigate crack growth due to hydrogen embrittlement at grain boundaries in sensitized aluminum.

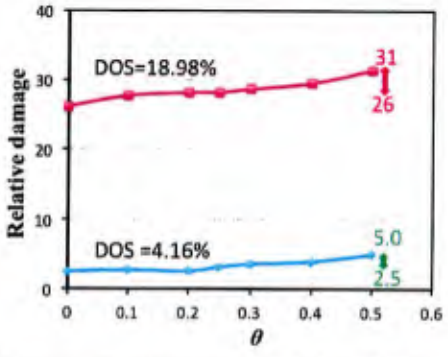

Figure 86. Crack damage as a function of hydrogen coverage in sensitized Al alloys with different DOS.

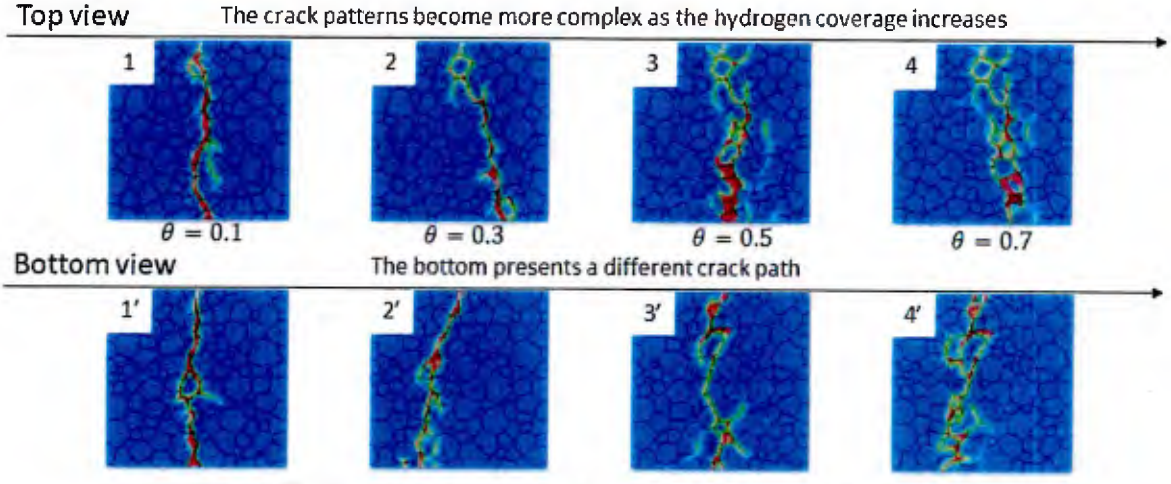

Figure 87. The change in crack path due to varying hydrogen coverage.

5.2 Identification of the Most Influential Parameters on Damage Tolerance

Although numerical modeling accelerates patch design by enabling exploration of varying material selections and configurations in a feasible amount of time, the large number of design parameters required for optimization of a composite patch structure remains challenging even when using high-performance computing (HPC). Sensitivity analysis provides a screening method to limit the design space by identifying and eliminating the non-influential parameters on patch performance. Design optimization is then performed using only the parameters that are determined to be influential on structural performance. Additionally, sensitivity analysis results inform the quality of data needed for each of the parameters. Highly influential parameters should be fully characterized and held to tight tolerances while parameters with little effect on performance can be defined with average values.

The high fidelity FE model captures multiple damage mechanisms: disbond at the metal/composite interface, delamination between lamina, matrix cracking, fiber breaks, and plasticity in the metal. This model was validated as demonstrated in section 4.4. As emphasized in this four bend testing discussion, comparing the force-displacement curve is not adequate to rigorously validate the model, and validation must include a comparison with the amounts of damage induced by each mechanism. Therefore, the importance of choosing the output variables for the sensitivity and uncertainty quantification cannot be understated. Initially, simple outputs to extract such as maximum and permanent deflection and total energy absorbed were investigated. It was clear that the behavior of this model fills a large and complex design space. In different subspaces of input parameters, different damage mechanisms govern and the sensitivity of the input parameters on the output changes dramatically throughout the space. To rigorously characterize the space, the energy associated with each damage mechanism was investigated and sensitivity analysis relative to the different type of energy absorption was studied.

This demonstration example begins with a classification of the quality of data that was used to define each independent input parameter. For this investigation, only material properties were used as the input parameters for the sensitivity analysis. To accurately represent the material behavior of the hybrid structure in the FE model, the material properties need to be acquired from experimental testing or valid sources to be considered high quality data. In the tables below that list the material properties, the values are highlighted green, yellow, or red corresponding good, neutral, or poor quality values. Neutral data was acquired from data sheets or experimental test data for similar materials. Poor data was obtained from empirical fitting or engineering judgement as a best estimate.

The properties for the aluminum 5456-H116 were provided by NSWCCD or were gathered from the Aluminum Association's Aluminum Standards and Data. These values are considered to be of good quality. The elastic-plastic properties are shown in Table 14. The Johnson-Cook equation was used to describe the strain hardening behavior of the aluminum alloy.

Table 14. Elastic and Plastic Properties for Aluminum 5456-H116

Young's Modulus, E	10.3 msi	*Strength Coefficient, B*	78.621 ksi
Poisson's Ratio, v	0.29	*Strain Hardening Exponent, n*	0.305
Hardening Parameter, A	75.045 ksi		

The baseline composite patch required eight separately detailed layers modeled to comprehensively simulate the progressive damage within the composite patch. Each of these layers have different material properties. The properties of the Hexcel 7500 lamina were provided by NSWCCD and are considered to be of high quality. These properties include the tension strength, elastic modulus, poisson's ratio, mode I interlaminar fracture toughness, and mode II interlaminar fracture toughness. These values are shown in Table 15. The mode I interlaminar fracture toughness and mode II interlaminar fracture toughness for Hexcel 7781, E-BX 1200, and E-LT 1800 were assumed to be the same as the Hexcel 7500. The other properties for the Hexcel 7781, E-BX 1200, and E-LT 1800 were obtained from manufacturer data. The shear properties of the laminae were estimated from similar fabric cyclic shear test using the technique and procedure demonstrated by Johnson [10]. The intralaminar fracture toughness of the Hexcel fabrics was estimated from similar E-glass/epoxy weave fabric stress intensity factors measured by Mandell et al. [11]. The intralaminar fracture toughness of the E-BX and E-LT laminates was derived from a double edge notched fracture test [29] of a [90/0] E-glass/epoxy composite. These values are considered poor quality and may require experimental characterization if identified as highly influential on damage tolerance results.

The resin properties were provided by NSWCCD and manufacturer data sheets. The properties for the cohesive layers between the lamina plies are shown in Table 16. The properties of the metal/composite interface are in Table 17.

Table 18 lists the sensitivity results on the total damage energy and the damage energy absorbed by the composite patch and metal separately. Table 19 provides the top 10 most influential parameters from the sensitivity analysis on each individual damage mechanism. Poor quality data has a major impact on model prediction in this example. The majority of the most influential parameters are those characterized by estimated parameters. It is therefore necessary to fullly characterize these parameters through a comprehensive test program to generate probability density functions for each parameter. This information is necessary for UQ to fully explore the variability in patch performance relative to these parameters.

Some additional observations from this study indicate that the top layer (Hexcel 7781) plays an important role in energy absorption of the composite patch. As expected, the most important inputs on the plastic behavior in the metal are the aluminum's properties (E and σ_y). The shear plasticity in the patch contributes significantly to reinforce the energy absorption capability of the aluminum (G_{12}, α_{12} and P).

Table 15. Mechanical Properties of Fabric Lamina

	Hexcel 7500	Hexcel 7781	E-BX 1200	E-LT 1800
Young's Modulus, $E_{11} = E_{22}$	2.83 msi	4.4 msi	2.031 msi	2.146 msi
Shear Modulus, G_{12}	0.8 msi	0.8 msi	0.8 msi	0.8 msi
Tensile Strength, $X_t = Y_t$	46.7 ksi	70 ksi	53 ksi	53 ksi
Poisson's Ratio, ν_{12}	0.15	0.15	0.13	0.13
Mode I interlaminar fracture toughness, G_I	7.6 in-lbs/in^2	7.6 in-lbs/in^2	7.6 in-lbs/in^2	7.6 in-lbs/in^2
Mode II interlaminar fracture toughness, G_{II}	15.6 in-lbs/in^2	15.6 in-lbs/in^2	15.6 in-lbs/in^2	15.6 in-lbs/in^2
Shear Strength of Laminate, X_{12}	5.16 ksi	5.16	5.16 ksi	5.16 ksi
Shear Damage Parameter, α_{12}	0.2767	0.2767	0.2767	0.2767
Maximum Shear Damage, d_{12}^{max}	0.714	0.714	0.714	0.714
Effective Shear Yield Stress, $\tilde{\sigma}_y$	5.16 ksi	5.16 ksi	5.16 ksi	5.16 ksi
Coefficient in Shear Hardening Equation, C	0.65 msi	0.65 msi	0.65 msi	0.65 msi
Power Term in Shear Hardening Equation, P	0.729	0.729	0.729	0.729
Maximum Shear Plastic Strain, ε_{max}^{pl}	0.02	0.02	0.02	0.02

Table 16. Mechanical Properties of Resin between Lamina

Nominal Stress Normal-Only Mode, σ_{nn}	8.1 ksi
Nominal Stress First Direction, σ_{ss}	5.88 ksi
Nominal Stress Second Direction, σ_{tt}	5.88 ksi
Normal Mode Fracture Energy, $G_{c,nn}$	7.6 lb-in/in^2
Shear Mode Fracture Eneregy First Direction, $G_{c,ss}$	16.588 lb-in/in^2
Shear Mode Fracture Energy Second Direction, $G_{c,tt}$	16.588 lb-in/in^2
Viscosity Coefficient	1e-05
Density, ρ	0.0425 lb/in^3
Elastic Modulus, E/E_{nn}	6.2 ksi
Shear Modulus First Direction, G_1/E_{ss}	1.571 ksi
Shear Modulus Second Direction, G_2/E_{tt}	1.571 ksi
Intralaminar fracture toughness, $G_I^f = G_{II}^f$	150 lbs/in

Table 17. Mechanical Properties of the Epoxy used in the cohesive zone law at the Metal/Composite Interface

Nominal Stress Normal-Only Mode; σ_{nn}	15.288 ksi
Nominal Stress First Direction, σ_{ss}	9.7572 ksi
Nominal Stress Second Direction, σ_{tt}	9.7572 ksi
Normal Mode Fracture Energy, $G_{c,nn}$	7.6 lb-in/in^2
Shear Mode Fracture Eneregy First Direction, $G_{c,ss}$	16.588 lb-in/in^2
Shear Mode Fracture Energy Second Direction, $G_{c,tt}$	16.588 lb-in/in^2
Viscosity Coefficient	1e-05
Density, ρ	0.0425 lb/in^3
Elastic Modulus, E/E_{nn}	6.2 ksi
Shear Modulus First Direction, G_1/E_{ss}	1.571 ksi
Shear Modulus Second Direction, G_2/E_{tt}	1.571 ksi
Intralaminar fracture toughness, $G_I^f = G_{II}^f$	150 lbs/in

Table 18. Most Influential Parameters on Damage Tolerance

Damage mechanisms	Ten most influential parameters
Damage in composite patch	$G^f_{7781}, E_{7500}, E_{1800}, E_{7781}, G^f_{IIint}, X_{Scoh}, G^f_{IIcoh}, \alpha_{12}, v_{7781}, X_{12}$
Plasticity in aluminum	$\sigma_y, E, P, n, \alpha_{12}, X_{Scoh}, G^f_{7781}, E_{7500}, G_{12}, E_{1800}$
All damage mechanisms	$G^f_{7781}, E_{7500}, E_{1800}, E_{7781}, X_{Scoh}, G^f_{IIint}, \sigma_y, G^f_{IIcoh}, E, \alpha_{12}$

Table 19. Most Influential Parameters on Individual Damage Mechanisms

Damage mechanisms	Ten most influential parameters
Plasticity in laminae	$E_{1800}, E_{7500}, P, \alpha_{12}, G^f_{1800}, E_{7781}, X_{Scoh}, G^f_{7781}, X_{12}, v_{7781}$
Intralaminar fracture	$E_{1800}, E_{7781}, E_{7500}, X_{12}, G^f_{7781}, v_{7781}, G^f_{1800}, BK_{coh}, v, E_{1200}$
Delamination	$P, G^f_{7781}, X_{12}, X_{Scoh}, C, G_{12}, G^f_{IIint}, \varepsilon^{pl}_{max}, v, v_{7781}$
Disbond at interface	$E, v, \sigma_y, K, n, E_{1200}, v_{1200}, X_{T1200}, G^f_{1200}, E_{1800}$
Plasticity in aluminum	$\sigma_y, E, P, n, \alpha_{12}, X_{Scoh}, G^f_{7781}, E_{7500}, G_{12}, E_{1800}$
All damage mechanisms	$G^f_{7781}, E_{7500}, E_{1800}, E_{7781}, X_{Scoh}, G^f_{IIint}, \sigma_y, G^f_{IIcoh}, E, \alpha_{12}$

5.3 DOS Effect on Damage in Sensitized Al Alloy Repaired with a Patch

This example investigates the effects of DOS on damage evolution in sensitized Al. The boundary conditions on an element loaded under bending are extracted from the FE model and applied to the PD model as shown in Figure 88. The PD model is then used to predict damage propagation for varying levels of DOS. The crack growth was defined as the accumulated PD damage over a time interval of 11.5 μs from the beginning of the simulation, a commonly used time period for calculating the crack velocity in PD simulation of fracture [125]. For the convenience of comparison, the predicted crack growth in each of the sensitized Al alloy model was normalized that of the pristine Al alloy model without sensitization, and a quantitative relationship was established by plotting the crack damage as a function of DOS in sensitized Al alloy (Figure 89).

Figure 88. Boundary and loading conditions are obtained on an element in the FE model. An SVE of the element is created for investigation using PD.

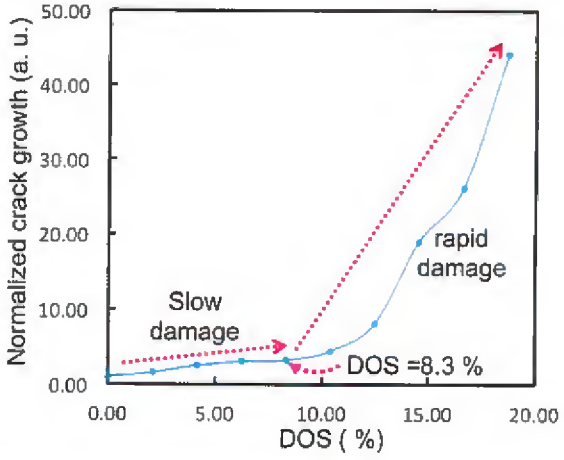

Figure 89. Predicted damage as a function of DOS in sensitized Al alloy. The red dashed lines show general experimental observations of damage growth as a function of DOS.

The results show that there are two distinct regimes of damage dependence on DOS: (1) a slow damage propagation region is observed where the damage increase is slow with increasing DOS, and (2) a rapid damage region where the damage increases quickly with the increase of DOS. The intersection of the slow crack damage trend line and the rapid crack damage trend line identifies a critical DOS value near 8.3%. The predicted trend of crack dependence on DOS agrees well with experimental observation of damage growth against the DOS in sensitized 5083-H131 Al alloy, where the damage growth jumps when DOS is above a critical value [124]. A satisfactory agreement is observed suggesting the accuracy of PD model in predicting the trend of DOS effect on crack growth in sensitized Al alloy.

In order to explain the presence of the two distinct regimes of the crack dependence on DOS, the potential energy and the crack propagation patterns corresponding to the crack growth in the sensitized Al alloys were plotted against DOS (Figure 90 and Figure 91). There is an overall trend where the potential energy decreases with increasing DOS, and a local inverse-volcano shape of the potential energy dependence on DOS was observed. The lowest point of the inverse-volcano

plot shows the same DOS value as Figure 89, again separating damage increase into two regions. For the pristine Al alloy, there is only one crack propagation band, which is centered to a narrow region in the middle of the model (Figure 91a) and is called center crack band. At the value of DOS lower than 8.3% in the sensitized Al alloys, this center crack band is observed to expand to the edge of the model with increasing DOS (Figure 91b-d). When the DOS is higher than 8.3%, two other side crack bands appear in the locations about one quarter of the model length to the edges (Figure 91 e-g), and both of the side crack bands tend to expand to the center and edge of the model with increasing DOS. With the DOS goes higher than 14.6%, the center crack band overlaps with the side crack bands, forming a wide crack propagation pattern across the entire sensitized element (Figure 91h-j). It is noted that the range of DOS values (8.3% to 16.6%) in the observed inverse-volcano shape dependence of the potential energy on DOS are consistent with those for the transition of one center crack band to the expanded crack These attributes suggest that the presence of the two distinct (slow and rapid) damage regions along with the increase of DOS (results from the difference of the crack propagation patterns, and the transition of the crack propagation patterns significantly affect the evolution of the potential energy with the variation of DOS.

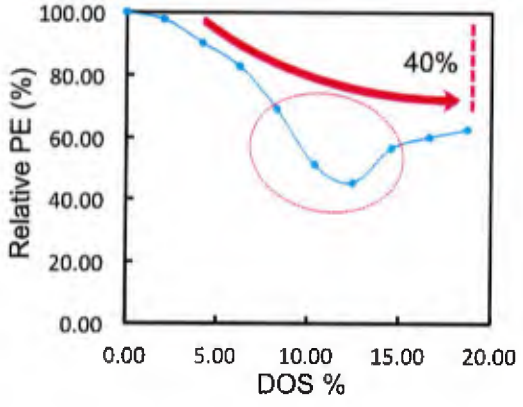

Figure 90. Predicted potential energy as a function of DOS in sensitized Al alloys. Each potential energy corresponds to the damage in one PD model at a given DOS value and is normalized to the potential energy of the pristine Al alloy.

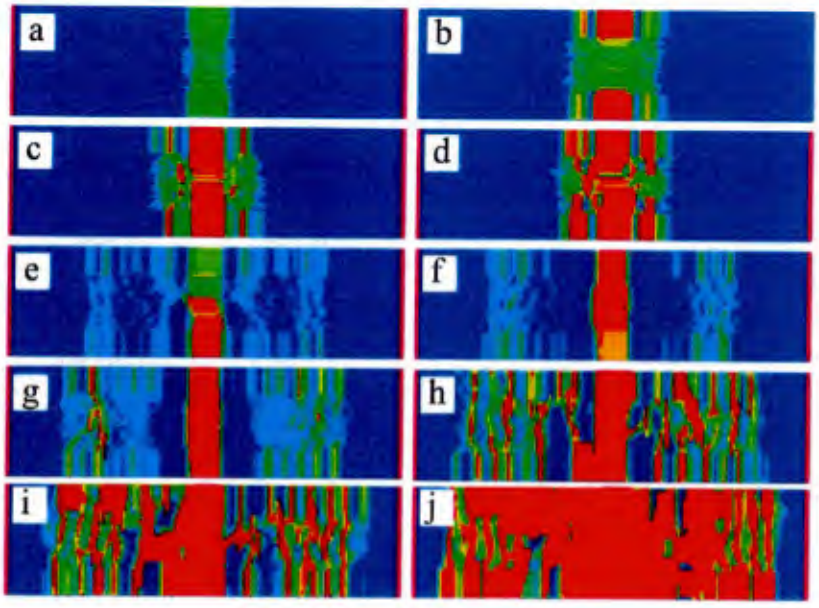

Figure 91. Crack propagation patterns in sensitized Al alloys with different DOS values. From a to j, the DOS values are 0% (i.e. pristine Al alloy without sensitization); 2.1%, 4.2%, 6.2%, 8.3%, 10.4%, 12.5%, 14.6%, 16.6%, and 18.7%

In summary, these results suggest that, along with the increase of DOS, the crack propagation pattern evolves from (1) a center crack band to (2) a combination of center and side crack bands and (3) a wide crack propagation pattern across the whole sensitized regions. In addition, the presence of the slow and rapid crack damage regimes along with the increase of DOS can be attributed to the difference of the crack propagation patterns.

6 Conclusions and Recommendations

An integrated approach encompassing computational simulation, experimental testing, and uncertainty quantification was developed and demonstrated to investigate the damage tolerance of hybrid structure. Damage mechanisms evaluated in this study include interlaminar and intralaminar composite overlay damage, plasticity, sensitization and crack growth in the metal, as well as disbond at the metal/polymer interface. Given the many types of damage mechanisms, the complexity of their interactions, and the disparate sources of uncertainty corresponding to damage type, models and methodology at varying scales and levels of fidelity were required to comprehensively investigate damage initiation and propagation. A probabilistic toolkit was developed and applied to identify the most influential input parameters across scales on global damage tolerance as well as the most influential parameters corresponding to specific damage mechanisms. Models and methodology were formulated to enable plug and play creation of varying geometric, material, loading, and boundary condition scenarios.

This holistic method of model development proved efficient in terms of the time, cost, and reduced amount of experimental testing required to develop validated multi-physics models capturing both

individual damage mechanisms and global interaction to investigate damage tolerance. The models can be readily chosen and assembled to explore a wide range of scenarios and hybrid structure designs providing Navy engineers an efficient capability for design and analysis of composite patches. Investigation of structural performance and prediction of damage tolerance through computational simulation is an effective approach to eliminate poor designs and optimize material selection and configuration prior to time-consuming and expensive experimental certification.

Recommendations:

(1) Damage should be quantified by the amount of energy absorbed by each individual damage mechanism. This information is readily extracted from the computational results, and damage energy can be correlated to the physical amount of damage in the structure. A maximum allowable amount of energy can then be set for each type of damage to ensure reliable patch performance. The total energy absorbed by the hybrid structure can be useful in comparing preliminary designs, but analysts must evaluate this value with caution as a patch with the lowest amount of total energy could fail first if all of the energy is absorbed by a single damage mechanism governed by rapid propagation.

(2) Evaluation and optimization on the full parameter space encompassing all potential damage mechanisms was demonstrated to be infeasible, even with supercomputing resources. Given the highly expansive, complex, and non-linear parameter space for damage tolerance, it is recommended to extract the energy absorbed by each damage mechanism and to identify the most dominant damage types. The problem of identifying the most influential parameters is then tractable by working in a limited subspace around this baseline design. The most sensitive parameters for each of the dominant mechanisms can be determined individually in a feasible amount of computational time. Design optimization can then be performed on this limited parameter space with allowable energy constraints as the objectives.

(3) Non-visible damage is a major concern when evaluating the reliability of hybrid structure. In-service loading, especially bending and low velocity impact, can cause internal damage that is difficult to detect during inspection. Even if this damage is minor, it can substantially degrade patch performance (for example, disbond at the bondline or matrix cracking in the composite will reduce load-carrying capacity) and provides sites for rapid damage propagation. Additionally, multiple damage sites were identified during this study under normal loading conditions, these sites were shown to have a propensity to interact and propagate into a failure-inducing damage mechanism.

(4) Failure at the bondline consists of three potential damage mechanisms: disbond between the metal and resin, cracking in the resin, and delamination at the bottom of the first fabric layer. All three types of damage were observed simultaneously during testing and at varying locations along the bondline. In the scenarios investigated in the study, the use of a smeared cohesive model along the bondline (validated with experimental test data) provided acceptable accuracy in simulation results.

(5) Given the large number of input parameters (hundreds), multiple objectives (each individual damage mechanism) and a highly non-linear space, it was challenging to build a surrogate model. While surrogate models were able to accurately fit the provided data, models were often found to be significantly inaccurate (by orders of magnitude) when randomly evaluated between data points. This problem was solved by evaluating individual damage mechanisms separately to identify the most influential parameters within this limited set and then including only the sensitive parameters for the damage mechanisms dominant in a subspace, thus

prohibiting a comprehensive investigation of parameter interactions and potentially missing parameters that defy engineering judgement. Even with supercomputing, it was impractical to sample enough parameter combinations to produce an adequate surrogate model for a full damage tolerance analysis. It is recommended that future work revisit surrogate modeling for this problem and that a comprehensive evaluation and mapping of the parameter space with respect to damage tolerance be performed. Potential methods to limit the parameter space a priori to surrogate modeling and uncertainty quantification should also be investigated.

(6) One significant limitation in this research that must be considered in design, analysis, and future work is that all variables were defined as independent in the sensitivity analysis. Parameter correlation and dependency is inherent in this problem and must be investigated for improved implementation of sensitivity analysis results into design, analysis, and optimization procedures.

(7) While sensitivity results from this research do serve as a preliminary indicator of the most influential parameters, more research is needed to determine how to perform a sensitivity analysis with confidence on a larger number of input parameters (50-200). As discussed, the amount of samples required to compute Sobol Indices for this many parameters in a non-linear space is prohibitive. Additionally, more research is required to correlate the Sobol Indices to the rate of damage propagation. There was typically not a clear cut-off point to determine how many parameters to include as highly influential in uncertainty quantification and optimization.

(8) This study evaluated Sobol Indices for first order and total effects and identified parameters with a significant difference between the two. Higher order effects calculations using chosen parameter combinations are then needed to identify the interacting parameters. An efficient method to systematically identify these interacting parameter combinations is needed.

7 References

1. Braun, D. and M. Pejcic, *Feasibility , conceptual design and optimization of a large composite hybrid hull.* Ship Structure Committee Report SSC-455, 2008.
2. Scott, R. and J. Sommella, *Feasibility study of glass reinforced plastic cargo ship.* Ship Structure Committee Report SSC-224, 1971.
3. Shields, M.D. and J. Zhang, *The generalization of Latin hypercube sampling.* Reliability Engineering & System Safety, 2016. **148**: p. 96-108.
4. Shields, M.D., et al., *Refined stratified sampling for efficient Monte Carlo based uncertainty quantification.* Reliability Engineering & System Safety, 2015. **142**: p. 310-325.
5. Saltelli, A. and P. Annoni, *How to avoid a perfunctory sensitivity analysis.* Environmental Modelling & Software, 2010. **25**(12): p. 1508-1517.
6. Iooss, B. and P. Lemaître, *A review on global sensitivity analysis methods*, in *Uncertainty Management in Simulation-Optimization of Complex Systems*. 2015, Springer. p. 101-122.
7. Saltelli, A., et al., *Variance based sensitivity analysis of model output. Design and estimator for the total sensitivity index.* Computer Physics Communications, 2010. **181**(2): p. 259-270.
8. Saltelli, A., et al., *Global sensitivity analysis: the primer*. 2008: John Wiley & Sons.
9. Nahshon, K. and N. Reynolds, *DICE: Distribution-based Input for Computational Evaluations, Version 0.3*. 2016, Naval Surface Warfare Center: West Bethesda, MD.
10. Lee, S.W., D.G. Lee, and K.S. Jeong, *Static and dynamic torque characteristics of composite cocured single lap joint.* Journal of Composite Materials, 1997. **31**(21): p. 2188-2201.
11. Cho, D.H. and D.G. Lee, *Optimum design of co-cured steel–composite tubular single lap joints under axial load.* Journal of adhesion science and technology, 2000. **14**(7): p. 939-963.
12. Fink, A., et al., *Hybrid CFRP/titanium bolted joints: Performance assessment and application to a spacecraft payload adaptor.* Composites Science and Technology, 2010. **70**(2): p. 305-317.
13. Kolesnikov, B., L. Herbeck, and A. Fink, *CFRP/titanium hybrid material for improving composite bolted joints.* Composite Structures, 2008. **83**(4): p. 368-380.
14. Lopes, J., et al., *Inter-laminar shear stress in hybrid CFRP/austenitic steel.* Frattura e Integrita Strutturale, 2015(31): p. 67-79.
15. Park, Y.-B., et al., *Strength of carbon/epoxy composite single-lap bonded joints in various environmental conditions.* Composite Structures, 2010. **92**(9): p. 2173-2180.
16. Ucsnik, S.A. and G. Kirov, *New possibility for the connection of metal sheets and fibre reinforced plastics.* Materials Science Forum, 2011. **690**: p. 465-8.
17. Xiong, W., et al., *The effect of composite orientation on the mechanical properties of hybrid joints strengthened by surfi-sculpt.* Composite Structures, 2015. **134**: p. 587-592.
18. Liang, C. and J. Hutchinson, *Mechanics of the fiber pushout test.* Mechanics of materials, 1993. **14**(3): p. 207-221.
19. William D. Callister, J., *Materials Science and Engineering: An Introduction*. 6th ed. 2003: John Wiley & Sons Inc.

20. da Silva, L.F.M., V.H.C. Esteves, and F.J.P. Chaves, *Fracture toughness of a structural adhesive under mixed mode loadings.* Materialwissenschaft und Werkstofftechnik, 2011. **42**(5): p. 460-470.
21. Chaves, F.J.P., et al., *Fracture Mechanics Tests in Adhesively Bonded Joints: A Literature Review.* The Journal of Adhesion, 2014. **90**(12): p. 955-992.
22. *ASTM D5528-13 Standard Test Method for Mode I Interlaminar Fracture Toughness of Unidirectional Fiber-Reinforced Polymer Matrix Composites.* 2013, ASTM International.
23. de Moura, M.F.S.F. and A.B. de Morais, *Equivalent crack based analyses of ENF and ELS tests.* Engineering Fracture Mechanics, 2008. **75**(9): p. 2584-2596.
24. S. H. YOON, C.S.H., *MODIFIED END NOTCHED FLEXURE SPECIMEN FOR MIXED MODE INTERLAMINAR FRACTURE IN LAMINATED COMPOSITES.* International Journal of Fracture, 1990. **43**: p. R3-R9.
25. Demoura, M., R. Campilho, and J. Goncalves, *Crack equivalent concept applied to the fracture characterization of bonded joints under pure mode I loading.* Composites Science and Technology, 2008. **68**(10-11): p. 2224-2230.
26. Oliveira JMQ, d.M.M., Morais JJL.. Holzforschung, *Application of the end loaded split and single-leg bending tests to the mixed-mode fracture characterization of wood.* 2009. **63**: p. 597-602.
27. W.S Kim, D.S.H., C.J. Jang, J.J. Lee, *ENHANCEMENT OF COMPOSITE-METAL ADHESION STRENGTH BY MICRO-PATTERNING OF METAL SURFACES*, in *18TH INTERNATIONAL CONFERENCE ON COMPOSITE MATERIALS.* 2011.
28. Alfano, G., *On the influence of the shape of the interface law on the application of cohesive-zone models.* Composites Science and Technology, 2006. **66**(6): p. 723-730.
29. Paulino, G.H. *2D ABAQUS UEL for the PPR potential-based cohesive model.* Available from: http://paulino.ce.gatech.edu/PPR_tutorial.html.
30. Allan, R., J. Bird, and J. Clarke, *Use of adhesives in repair of cracks in ship structures.* Materials Science and Technology, 1988. **4**(10): p. 853-859.
31. Grabovac, I., R. Bartholomeusz, and A. Baker, *Composite reinforcement of a ship superstructure—project overview.* Composites, 1993. **24**(6): p. 501-509.
32. Grabovac, I., *Bonded composite solution to ship reinforcement.* Composites Part A: Applied Science and Manufacturing, 2003. **34**(9): p. 847-854.
33. Grabovac, I., *Composite Reinforcement for Naval Ships: Concept Design, Analysis and Demonstration.* 2005.
34. Turton, T., J. Dalzel-Job, and F. Livingstone, *Oil platforms, destroyers and frigates—case studies of QinetiQ's marine composite patch repairs.* Composites Part A: Applied Science and Manufacturing, 2005. **36**(8): p. 1066-1072.
35. Grabovac, I. and D. Whittaker, *Application of bonded composites in the repair of ships structures–A 15-year service experience.* Composites Part A: Applied Science and Manufacturing, 2009. **40**(9): p. 1381-1398.
36. McGeorge, D., et al., *Repair of floating offshore units using bonded fibre composite materials.* Composites Part A: Applied science and manufacturing, 2009. **40**(9): p. 1364-1380.
37. Weitzenboeck, J.R. and D. McGeorge. *A cold repair method for FPSOs.* in *Offshore Technology Conference.* 2012. Offshore Technology Conference.
38. Avgoulas, E., et al., *Numerical analysis of cracked marine structures repaired with composite patches.* Tree Biotechnology, 2014: p. 367.

39. Golumbfskie, W.J., *Aluminum Sensitization and the Navy*. 2014, TMS Annual Meeting and Exhibition.
40. Karatzas, V.A., E.A. Kotsidis, and N.G. Tsouvalis, *Experimental Fatigue Study of Composite Patch Repaired Steel Plates with Cracks.* Applied Composite Materials, 2015. **22**(5): p. 507-523.
41. Kwon, Y. and B. Hall, *Analyses of cracks in thick stiffened plates repaired with single-sided composite patch.* Composite Structures, 2015. **119**: p. 727-737.
42. Meggiolaro, M.A., et al., *Stress intensity factor equations for branched crack growth.* Engineering Fracture Mechanics, 2005. **72**(17): p. 2647-2671.
43. Zhang, W. and L. Cai. *In-situ SEM and optical microscopy testing for investigation of fatigue crack growth mechanism under overload.* in *MATEC Web of Conferences*. 2018. EDP Sciences.
44. Wang, C.H., L.R.F. Rose, and R. Callinan, *Analysis of out-of-plane bending in one-sided bonded repair.* International Journal of Solids and Structures, 1998. **35**(14): p. 1653-1675.
45. Lee, J., M. Cho, and H.S. Kim, *Bending analysis of a laminated composite patch considering the free-edge effect using a stress-based equivalent single-layer composite model.* International Journal of Mechanical Sciences, 2011. **53**(8): p. 606-616.
46. Clark, R.J. and D.P. Romilly, *Bending of bonded composite repairs for aluminum aircraft structures: A design study.* Journal of Aircraft, 2007. **44**(6): p. 2012-2025.
47. Goodmiller, G.R. and S.C. TerMaath. *Investigation of composite patch performance under low-velocity impact loading.* in *55th AIAA/ASMe/ASCE/AHS/SC Structures, Structural Dynamics, and Materials Conference*. 2014.
48. Ramji, M., R. Srilakshmi, and M. Bhanu Prakash, *Towards optimization of patch shape on the performance of bonded composite repair using FEM.* Composites Part B: Engineering, 2013. **45**(1): p. 710-720.
49. Bachir Bouiadjra, B., et al., *Comparison between rectangular and trapezoidal bonded composite repairs in aircraft structures: A numerical analysis.* Materials & Design, 2011. **32**(6): p. 3161-3166.
50. Mall, S. and D. Conley, *Modeling and validation of composite patch repair to cracked thick and thin metallic panels.* Composites Part A: Applied Science and Manufacturing, 2009. **40**(9): p. 1331-1339.
51. Ouinas, D., et al., *Progressive edge cracked aluminium plate repaired with adhesively bonded composite patch under full width disbond.* Composites Part B: Engineering, 2012. **43**(2): p. 805-811.
52. Hosseini-Toudeshky, H., et al., *Numerical and experimental fatigue crack growth analysis in mode-I for repaired aluminum panels using composite material.* Composites Part A: applied science and manufacturing, 2007. **38**(4): p. 1141-1148.
53. Benyahia, F., et al., *Experimental and numerical analysis of bonded composite patch repair in aluminum alloy 7075 T6.* Materials & Design, 2015. **73**: p. 67-73.
54. Ouinas, D., B.B. Bouiadjra, and B. Serier, *The effects of disbonds on the stress intensity factor of aluminium panels repaired using composite materials.* Composite Structures, 2007. **78**(2): p. 278-284.
55. Denney, J.J. and S. Mall, *Characterization of disbond effects on fatigue crack growth behavior in aluminum plate with bonded composite patch.* Engineering Fracture Mechanics, 1997. **57**(5): p. 507-525.

56. Chang, F.-K. and K.-Y. Chang, *A progressive damage model for laminated composites containing stress concentrations.* Journal of composite materials, 1987. **21**(9): p. 834-855.
57. Perugini, P., A. Riccio, and F. Scaramuzzino. *Three-dimensional progressive damage analysis of composite joints.* in *Proceedings of the eighth international conference on The application of artificial intelligence to civil and structural engineering computing.* 2001. Civil-Comp Press.
58. Donadon, M.V., et al., *A progressive failure model for composite laminates subjected to low velocity impact damage.* Computers & Structures, 2008. **86**(11): p. 1232-1252.
59. Bednarcyk, B.A., J. Aboudi, and S.M. Arnold, *Micromechanics modeling of composites subjected to multiaxial progressive damage in the constituents.* AIAA journal, 2010. **48**(7): p. 1367-1378.
60. Kashfuddoja, M. and M. Ramji, *An experimental and numerical investigation of progressive damage analysis in bonded patch repaired CFRP laminates.* Journal of Composite Materials, 2015. **49**(4): p. 439-456.
61. Akterskaia, M., E. Jansen, and R. Rolfes. *Progressive Failure Analysis of Stiffened Composite Panels Using a Two-Way Loose Coupling Approach Including Intralaminar Failure and Debonding.* in *2018 AIAA/ASCE/AHS/ASC Structures, Structural Dynamics, and Materials Conference.* 2018.
62. Sápi, Z., R. Butler, and A.T. Rhead. *Numerical Prediction of Failure in Composite T-Joints Using Progressive Damage Modelling.* in *2018 AIAA/ASCE/AHS/ASC Structures, Structural Dynamics, and Materials Conference.* 2018.
63. Jones, R., W.K. Chiu, and R. Smith, *Airworthiness of composite repairs: Failure mechanisms.* Engineering Failure Analysis, 1995. **2**(2): p. 117-128.
64. Papanikos, P., et al., *Progressive damage modelling of bonded composite repairs.* Theoretical and Applied Fracture Mechanics, 2005. **43**(2): p. 189-198.
65. Holroyd, N.J.H. and G.M. Scamans, *Environmental Degradation of Marine Aluminum Alloys—Past, Present, and Future.* CORROSION, 2016. **72**(2): p. 136-143.
66. Jones, R.H., J.S. Vetrano, and C.F.W. Jr., *Stress Corrosion Cracking of Al-Mg and Mg-Al Alloys.* CORROSION, 2004. **60**(12): p. 1144-1154.
67. Lim, M.L.C., R.G. Kelly, and J.R. Scully, *Overview of Intergranular Corrosion Mechanisms, Phenomenological Observations, and Modeling of AA5083.* CORROSION, 2016. **72**(2): p. 198-220.
68. Goswami, R. and R.L. Holtz, *Transmission Electron Microscopic Investigations of Grain Boundary Beta Phase Precipitation in Al 5083 Aged at 373 K (100 degrees C).* Metallurgical and Materials Transactions a-Physical Metallurgy and Materials Science, 2013. **44A**(3): p. 1279-1289.
69. Gupta, R.K., et al., *Influence of Mg Content on the Sensitization and Corrosion of Al-xMg(-Mn) Alloys.* Corrosion, 2013. **69**(11): p. 1081-1087.
70. Jones, R.H., et al., *Role of Mg in the stress corrosion cracking of an Al-Mg alloy.* Metallurgical and Materials Transactions A, 2001. **32**(7): p. 1699-1711.
71. Zhao, Y., et al., *The role of grain boundary plane orientation in the β phase precipitation of an Al–Mg alloy.* Scripta Materialia, 2014. **89**: p. 49-52.
72. Goswami, R., et al., *Microstructural Evolution and Stress Corrosion Cracking Behavior of Al-5083.* Metallurgical and Materials Transactions a-Physical Metallurgy and Materials Science, 2011. **42A**(2): p. 348-355.

73. Holtz, R.L., et al., *Corrosion-Fatigue Behavior of Aluminum Alloy 5083-H131 Sensitized at 448 K (175 °C).* Metallurgical and Materials Transactions A, 2012. **43**(8): p. 2839-2849.
74. David A Shifler; T Tsuru; P M Natishan; Electrochemical Society. Meeting; Electrochemical society (Etats-Unis). Corrosion division, e.a., *Corrosion in marine and saltwater environments II : proceedings of the international symposium.* Pennington, NJ : Electrochemical Society, cop., 2005.
75. Seong, J., G.S. Frankel, and N. Sridhar, *Corrosion Inhibition of Sensitized and Solutionized AA5083.* Journal of the Electrochemical Society, 2015. **162**(9): p. C449-C456.
76. Lyndon, J.A., et al., *Electrochemical behaviour of the β-phase intermetallic (Mg2Al3) as a function of pH as relevant to corrosion of aluminium–magnesium alloys.* Corrosion Science, 2013. **70**: p. 290-293.
77. Ai, J.-H., M.L.C. Lim, and J.R. Scully, *Effective Hydrogen Diffusion in Aluminum Alloy 5083-H131 as a Function of Orientation and Degree of Sensitization.* CORROSION, 2013. **69**(12): p. 1225-1239.
78. Holroyd, N.J.H., et al., *Improved understanding of environment-induced cracking (EIC) of sensitized 5XXX series aluminium alloys.* Materials Science and Engineering: A, 2017. **682**: p. 613-621.
79. Eric F. Herzberg, P.N.C., Mitch L. Daniels, and Norman T. O'Meara, *Estimate of the Annual Cost of Corrosion for Navy Ships FY2008–10.* CorrDefense, 2012.
80. Hart, D.C. *5xxx Aluminum Sensitization and Application of Laminated Composite Patch Repairs*. 2017. Cham: Springer International Publishing.
81. Jones, A.A.B.L.R.F.R.R., *Advances in the Bonded Composite Repair of Metallic Aircraft Structure* Elsevier Science, 2003. **1st edition**: p. 1122.
82. Silling, S.A. and R.B. Lehoucq, *Peridynamic Theory of Solid Mechanics*, in *Advances in Applied Mechanics*, H. Aref and E.v.d. Giessen, Editors. 2010, Elsevier. p. 73-168.
83. Erdogan Madenci, E.O., *Peridynamic Theory and Its Applications.* Springer, 2014: p. 289.
84. Lusk, M.T. and A.E. Mattsson, *High-performance computing for materials design to advance energy science.* MRS Bulletin, 2011. **36**(3): p. 169-174.
85. Giannozzi, P., et al., *QUANTUM ESPRESSO: a modular and open-source software project for quantum simulations of materials.* Journal of Physics-Condensed Matter, 2009. **21**(39).
86. Perdew, J.P., K. Burke, and M. Ernzerhof, *Generalized Gradient Approximation Made Simple.* Physical Review Letters, 1996. **77**(18): p. 3865-3868.
87. Vanderbilt, D., *Soft self-consistent pseudopotentials in a generalized eigenvalue formalism.* Physical Review B, 1990. **41**(11): p. 7892-7895.
88. Monkhorst, H.J. and J.D. Pack, *Special points for Brillouin-zone integrations.* Physical Review B, 1976. **13**(12): p. 5188-5192.
89. Alchagirov, A.B., et al., *Energy and pressure versus volume: Equations of state motivated by the stabilized jellium model.* Physical Review B, 2001. **63**(22): p. 224115.
90. Davey, W.P., *Precision Measurements of the Lattice Constants of Twelve Common Metals.* Physical Review, 1925. **25**(6): p. 753-761.
91. Gerlich, D. and E.S. Fisher, *The high temperature elastic moduli of aluminum.* Journal of Physics and Chemistry of Solids, 1969. **30**(5): p. 1197-1205.

92. Kappes, M., M. Iannuzzi, and R.M. Carranza, *Hydrogen Embrittlement of Magnesium and Magnesium Alloys: A Review.* Journal of the Electrochemical Society, 2013. **160**(4): p. C168-C178.
93. Ai, J.H., M.L.C. Lim, and J.R. Scully, *Effective Hydrogen Diffusion in Aluminum Alloy 5083-H131 as a Function of Orientation and Degree of Sensitization.* Corrosion, 2013. **69**(12): p. 1225-1239.
94. Scully, J.R., G.A. Young, and S.W. Smith, *19 - Hydrogen embrittlement of aluminum and aluminum-based alloys*, in *Gaseous Hydrogen Embrittlement of Materials in Energy Technologies*, R.P. Gangloff and B.P. Somerday, Editors. 2012, Woodhead Publishing. p. 707-768.
95. Möller, J.J., et al., *Fracture ab initio: A force-based scaling law for atomistically informed continuum models.* Journal of Materials Research, 2018. **33**(22): p. 3750-3761.
96. Bitzek, E., J.R. Kermode, and P. Gumbsch, *Atomistic aspects of fracture.* International Journal of Fracture, 2015. **191**(1): p. 13-30.
97. Rice, J.R. and J.-S. Wang, *Embrittlement of interfaces by solute segregation.* Materials Science and Engineering: A, 1989. **107**: p. 23-40.
98. Jiang, D.E. and E.A. Carter, *First principles assessment of ideal fracture energies of materials with mobile impurities: implications for hydrogen embrittlement of metals.* Acta Materialia, 2004. **52**(16): p. 4801-4807.
99. Serebrinsky, S., E.A. Carter, and M. Ortiz, *A quantum-mechanically informed continuum model of hydrogen embrittlement.* Journal of the Mechanics and Physics of Solids, 2004. **52**(10): p. 2403-2430.
100. Silling, S. and R. Lehoucq, *Peridynamic theory of solid mechanics.* Advances in applied mechanics, 2010. **44**: p. 73-168.
101. Kilic, B. and E. Madenci, *Coupling of peridynamic theory and the finite element method.* Journal of mechanics of materials and structures, 2010. **5**(5): p. 707-733.
102. Oterkus, E., et al., *Combined finite element and peridynamic analyses for predicting failure in a stiffened composite curved panel with a central slot.* Composite Structures, 2012. **94**(3): p. 839-850.
103. De Meo, D., et al., *Modelling of stress-corrosion cracking by using peridynamics.* International Journal of Hydrogen Energy, 2016. **41**(15): p. 6593-6609.
104. Silling, S.A. and E. Askari, *A meshfree method based on the peridynamic model of solid mechanics.* Computers & Structures, 2005. **83**(17): p. 1526-1535.
105. Parks, M.L., et al., *Implementing peridynamics within a molecular dynamics code.* Computer Physics Communications, 2008. **179**(11): p. 777-783.
106. Groeber, M.A. and M.A. Jackson, *DREAM. 3D: a digital representation environment for the analysis of microstructure in 3D.* Integrating Materials and Manufacturing Innovation, 2014. **3**(1): p. 5.
107. Zhang, R., et al., *Experiment-based modelling of grain boundary beta-phase (Mg2Al3) evolution during sensitisation of aluminium alloy AA5083.* Scientific Reports, 2017. **7**.
108. Heng, B. and S.C. TerMaath, *Prediction of Damage Tolerance in Metallic Structure Repaired with a Co-Cured Composite Patch*, in *2018 AIAA/ASCE/AHS/ASC Structures, Structural Dynamics, and Materials Conference*. 2018, American Institute of Aeronautics and Astronautics.
109. Monteiro, J.P.R., et al., *Experimental estimation of the mechanical and fracture properties of a new epoxy adhesive.* Applied Adhesion Science, 2015. **3**(1): p. 25.

110. TerMaath, S.C., *A two-dimensional analytical technique for studying fracture in brittle materials containing interacting kinked and branched cracks.* 2001.
111. TerMaath, S., S. Phoenix, and C.-Y. Hui, *A technique for studying interacting cracks of complex geometry in 2D.* Engineering fracture mechanics, 2006. **73**(8): p. 1086-1114.
112. TerMaath, S.C. and S.L. Phoenix, *Investigation of a new analytical method for treating kinked cracks in a plate*, in *Fatigue and Fracture Mechanics: 31st Volume*. 2000, ASTM International.
113. Yavuz, A.K., S.L. Phoenix, and S. TerMaath, *An accurate and fast analysis for strongly interacting multiple crack configurations including kinked (V) and branched (Y) cracks.* International Journal of Solids and Structures, 2006. **43**(22-23): p. 6727-6750.
114. Yavuz, A.K., S.L. Phoenix, and S.C. TerMaath, *Multiple crack analysis in finite plates.* AIAA journal, 2006. **44**(11): p. 2535-2541.
115. Abaqus, V., *6.14 Documentation.* Dassault Systemes Simulia Corporation, 2014. **651.**
116. Johnson, A.F., *Modelling fabric reinforced composites under impact loads.* Composites Part A: Applied Science and Manufacturing, 2001. **32**(9): p. 1197-1206.
117. Johnson, A.F., A.K. Pickett, and P. Rozycki, *Computational methods for predicting impact damage in composite structures.* Composites Science and Technology, 2001. **61**(15): p. 2183-2192.
118. Turon, A., et al., *An engineering solution for mesh size effects in the simulation of delamination using cohesive zone models.* Engineering Fracture Mechanics, 2007. **74**(10): p. 1665-1682.
119. Kleemola, H.J. and M.A. Nieminen, *On the strain-hardening parameters of metals.* Metallurgical Transactions, 1974. **5**(8): p. 1863-1866.
120. Turon, A., et al., *A damage model for the simulation of delamination in advanced composites under variable-mode loading.* Mechanics of Materials, 2006. **38**(11): p. 1072-1089.
121. Benzeggagh, M. and M. Kenane, *Measurement of mixed-mode delamination fracture toughness of unidirectional glass/epoxy composites with mixed-mode bending apparatus.* Composites science and technology, 1996. **56**(4): p. 439-449.
122. Mandell, J.F., S.-S. Wang, and F.J. Mcgarry, *The extension of crack tip damage zones in fiber reinforced plastic laminates.* Journal of Composite Materials, 1975. **9**(3): p. 266-287.
123. Hallett, S.R. and M.R. Wisnom, *Experimental investigation of progressive damage and the effect of layup in notched tensile tests.* Journal of Composite Materials, 2006. **40**(2): p. 119-141.
124. Crane, C., *Validation of the Coupled Dissolution-Hydrogen Embrittlement Mechanism of IGSCC in Low Temperature Sensitized AA5083-H131.* PhD Dissertation, University of Virginia, 2013.
125. Florin Bobaru, J.T.F., Philippe H Geubelle, Stewart A. Silling, *Handbook of Peridynamic Modeling.* Chapman and Hall/CRC, 2016.